



## Design Solutions for 10MW Floating Offshore Wind Turbines

Agreement n.:	308974
Duration	November 2012 – October 2017
Co-ordinator:	DTU Wind



The research leading to these results has received funding from the European Community's Seventh Framework Programme FP7-ENERGY-2012-1-2STAGE under grant agreement No. 308974 (INNWIND.EU).nn

---

### PROPRIETARY RIGHTS STATEMENT

This document contains information, which is proprietary to the "INNWIND.EU" Consortium. Neither this document nor the information contained herein shall be used, duplicated or communicated by any means to any third party, in whole or in parts, except with prior written consent of the "INNWIND.EU" consortium.

---

## Document information

Document Name:	<b>Design Solutions for 10MW Floating Offshore Wind Turbines</b>
Document Number:	<b>Deliverable D 4.3.7</b>
Author:	<b>José Azcona, Felipe Vittori (CENER) Uwe Schmidt (DTU) Feike Savenije (ECN) Giannis Kapogiannis, Xaris Karvelas, Dimitris Manolas, Spyros Voutsinas (NTUA) Florian Amann, Ricardo Faerron-Guzmán, Frank Lemmer (USTUTT)</b>
Document Type	Report
Dissemination level	PU
Review:	<b>José Azcona Armendáriz (CENER)</b>
Date:	<b>04/10/2017</b>
WP:	<b>4 Offshore Foundations and Support Structures</b>
Task:	<b>4.3 Structural Implementation</b>
Approval:	Approved by WP Leader

## Table of contents

1	INTRODUCTION.....	5
2	SITE CONDITIONS.....	7
3	WIND TURBINE DESCRIPTION .....	8
4	CONCEPTUAL DESIGN ANALYSIS .....	10
4.1	Parametric design of the steel tripod.....	10
4.1.1	Parametric spreadsheet calculations .....	12
4.1.2	Parametric hydrodynamic panel code simulations .....	12
5	MOORING LINES.....	19
5.1	Design description .....	19
5.2	Mooring line design dynamic verification .....	21
6	CONTROLLER.....	25
6.1	Controller design .....	26
6.1.1	Controller input processing.....	26
6.1.2	Baseline power and rotor speed regulation.....	27
6.1.3	Drive train damping.....	31
6.1.4	Tower damping.....	32
6.2	Controller evaluation.....	32
6.2.1	Initial evaluation and tuning in ACT.....	32
6.2.2	Controller assessment and tuning with FAST .....	33
6.2.3	Complete DLC evaluation with hGAST.....	34
7	DETAILED DESIGN ANALYSIS.....	35
7.1	Introduction .....	35
7.2	Coupled hydro-servo-aero-elastic analysis .....	35
7.2.1	Time domain simulations.....	35
7.2.2	Eigen-value analysis.....	38
7.3	ULS analysis of the tri-spar Floater .....	39
7.3.1	Description of modelling.....	39
7.3.2	Determination of the external (hydrodynamic) loading.....	40

7.3.3	Detailed structural design and verification .....	43
7.3.4	Capacity ratios of the main parts of the tri-spar floater .....	44
7.3.5	Steel Tripod.....	45
7.3.6	Steel-concrete connection .....	49
7.3.7	Reinforcement of the Concrete cylindrical columns .....	51
7.3.8	Heave Plates.....	51
7.3.9	Platform data .....	52
7.3.10	Equivalent beam properties.....	53
7.4	FLS analysis of the tri-spar floater .....	54
7.4.1	Theory.....	54
7.4.2	Results: Critical sections and Damage ratios .....	56
8	THE FLOATING VERTICAL AXIS WIND TURBINE CASE.....	59
8.1	Introduction .....	59
8.2	Design description and upscaling.....	59
8.3	Mooring system.....	64
8.3.1	Decay testing: .....	68
8.4	Controller.....	69
8.5	Energy production and cost estimations .....	72
	Cost estimation.....	76
8.6	Discussion .....	76
9	OUTLOOK FOR THE DESIGN SOLUTIONS OF FLOATING WIND TURBINES .....	77
9.1	Introduction .....	77
9.2	Pressure mapping for finite element analysis.....	77
9.2.1	Boundary element method solver .....	78
9.2.2	Aero-hydro-elastic simulations.....	78
9.2.3	Pre-processing for time domain pressures .....	79
9.2.4	Finite element model of floating platform .....	81
9.2.5	Example time domain simulation of excitation pressures .....	82
9.3	Summary and considerations .....	83
10	CONCLUSIONS.....	85
11	REFERENCES.....	87

## 1 INTRODUCTION

The work package 4 of the INNWIND.EU project has developed design methodologies, testing procedures and simulation tools for offshore wind turbines both fixed and floating. These developments have been applied to design a reference floating substructure for the 10MW INNWIND reference wind turbine in the Task 4.3. The design of this reference floater for the horizontal axis wind turbine (HAWT) is described in this report. In addition, a reference floating platform for a 10MW vertical axis wind turbine (VAWT) is also described.

The work described in this document is based on a first exercise of design of floating substructure for the INNWIND reference 10MW wind turbine that was reported in the project deliverable 4.33 (Sandner, et al., 2014). In this deliverable, four different innovative concepts shown in Figure 1 were proposed.

One of these concepts was designed by DTU and consisted of a semi-floater concept that combines the strengths of floating structures with those of bottom fixed. This technology has been proven in the oil and gas industry and it is well suited in intermediate water depths. In addition, it outperforms bottom-fixed structures in terms of fatigue lifetime and lesser motions than floating structures.

Two different torus-shape structures in concrete were proposed by USTUTT and NTUA. The torus has the advantage of a reduced draft for an increased flexibility to the water depth and it significantly reduces the wave excitation due to the “moonpool” feature and the steel construction around water level, where wave forces are high. One of the designs has two dynamically linked floating bodies to reduce excitation from waves. The use of concrete as material can drastically reduce the cost of these designs.

Finally, an asymmetric semi-submersible floater was designed by CENER. The substructure is composed of three cylinders, connected by pontoons to form a geometrically simple shape. The function of the pontoons is not only structural, but also hydrodynamic: the pontoons work as heave plates to damp the motion of the offshore wind turbine. In addition, the wind turbine is mounted on one of the cylinders, instead of building a central structure to hold it in the platform centre. This allows for the simplification of the structure and reduction in manufacturing costs.

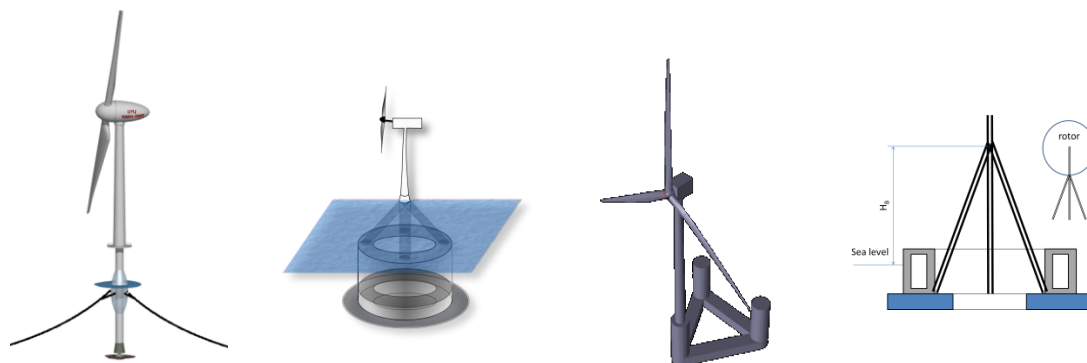


**Figure 1 - Conceptual designs analyzed. From left to right: semi-floater, concrete torus, semisubmersible and concrete torus linked with floating bodies**

After the comparative analysis of these concepts it was concluded that the semisubmersible design has a good dynamic behaviour, together with manufacturing and installation advantages

due to a reduced draft and good stability. On the other hand, the use of concrete can potentially reduce the cost of the platforms. The semi-floater concept is suitable for moderate depths.

These “lessons learned” were taken as starting point for the design of the INNWIND reference floating platform that is described in this report. The platform is a hybrid semisubmersible design composed by three concrete cylinders with low draft for flexible deployment and a simple assembly and installation. Heave plates, also in concrete, are added at the cylinder’s base to increase the damping in heave. A low-cost steel transition piece connects the platform with the wind turbine. The concrete material was selected for the platform to decrease the cost. The concept is called TripleSpar. An artistic representation is presented in Figure 2 giving an impression of its dimensions.



Figure 2 – TripleSpar.

This document reports the development of the TripleSpar platform from the first conceptual design based on simplified tools to the structural dimensioning with more complex tools. The design of the platform includes the development of a specific mooring line system for the particular selected location and a control strategy to optimise production and reduce loads. The design has been verified using integrated simulations tools to evaluate the dynamics and the performance of the system and the loads at the different components.

Finally, the design of a 10MW VAWT is also included in the present report. In this connection, the 5MW DeepWind VAWT has been upscaled to 10MW and its performance in terms of power production and cost have been estimated. The procedures and findings are regarded preliminary especially if comparison of the two types of WT is intended. On the one hand the floater is different in several aspects one of which being the targeted depth while on the other hand the level of detail in the analysis is largely higher in the HAWT case.

## 2 SITE CONDITIONS

The site conditions selected for the design of the TripleSpar platform were defined in the project LIFES50+ (Gómez, Sánchez, Llana, & Gonzalez, 2015). This document presents complete information about wind, wave and current for various water depths that comes from measurements of offshore sites intended for real wind farm developments, offering enough data for a simplified load analysis.

This document reports the environmental conditions of three different locations. The conditions at the Gulf of Maine in United States of America, were selected for the verification of the TripleSpar, because they were considered representative of the target design locations of the TripleSpar concept. Table 1 presents the main environmental parameters.

**Table 1 Design environmental conditions**

50-year wind at hub height	50-year significant wave height	50-year sea-state peak period	50-year current	Extreme water level range	Water depth
44 m/s	10.9 m	9 - 16 s	1.13 m/s	4.3 m	180 m

### 3 WIND TURBINE DESCRIPTION

The TripleSpar floating platform is designed to support the INNWIND reference 10MW wind turbine (Bak C. , et al., 2013). This turbine was designed for offshore applications and is intended for a class 1A location. The rated wind speed is 11.4m/s. Table 2 presents general data about the wind turbine.

**Table 2 General parameter of DTU10MW RWT**

Rotor orientation	Upwind
Control	Variable speed / collective pitch
Rotor diameter	178.3 m
Hub Height	119 m
Minimum Rotor speed	6 rpm
Maximum Rotor speed	9.6 rpm
Gear box ratio	50
Hub Overhang	7.1 m
Shaft tilt angle	5 deg
Blade Pre-cone	2.5 deg
Nacelle Mass	446036 kg

The tower of the INNWIND 10MW reference wind turbine has been shortened in 25m (that correspond to the foreboard of the platform) to keep the original hub height of 119m. The values for the tower base diameter and the mass per length at the height of 25 m were interpolated as it is shown in Table 3. The properties of the new tower are listed in Table 4.

**Table 3 - Diameter and mass distribution of the tower.**

Height [m]	Outer diameter [m]	Mass per length [kg/m]
0.000	8.3000	8383.74
11.500	8.0215	8101.16
11.501	8.0215	7676.68
23.000	7.7430	7409.00
23.001	7.7430	6999.18
<b>25.000</b>	<b>7.6946</b>	<b>6955.21</b>
34.500	7.4646	6746.37
34.501	7.4646	6351.21
46.000	7.1861	6113.27

46.001	7.1861	5732.78
57.500	6.9076	5509.71
57.501	6.9076	5143.87
69.000	6.6292	4935.68
69.001	6.6292	4584.50
80.500	6.3507	4391.17
80.501	6.3507	4054.66
92.000	6.0722	3876.20
92.001	6.0722	3554.35
103.500	5.7937	3390.76
103.501	5.7937	3083.57
115.630	5.5000	2926.71

Table 4 New tower properties.

Tower Property	Original tower	Shortened tower
Tower base diameter	8.3 m	7.7 m
Length	115.63 m	90.63 m
Weight	628 442 kg	432 955 kg
Center of mass above SWL	47,57 m	63,56 m

## 4 CONCEPTUAL DESIGN ANALYSIS

The platform is a semisubmersible platform with three concrete cylinders. The columns are connected by a steel tripod, which supports the tower of the DTU 10MW reference wind turbine, (Bak C. Z., 2013). The tower of the turbine had to be shortened by 25 m because of the height of the tripod and the column elevation above SWL. The hollow columns are filled with solid ballast. Figure 3 shows a sketch of the concept: It is a deep-drafted semi-submersible with the prospect of combining the advantages of a spar with those of a semi-submersible. Thus, with a maximum draft of 60m, smaller than the one of typical spar platforms, and simple cylindrical shapes made of concrete, the material cost is reduced. A low draft has the prospect of flexibility to sites with a low water depth – a clear advantage of semi-submersibles. On the other hand, a spar is usually easier to manufacture due to the simple cylindrical shape and has smaller material costs. The columns are only connected through a three-legged steel structure in order to enable an assembly with the wind turbine at site, as for the Hywind Scotland wind farm (Skaare, 2017). The use of concrete for the columns was already investigated in the EU KIC-InnoEnergy project AFOSP for a concrete spar, see (Molins, Campos, Sandner, & Matha, 2014). Recently, reinforced concrete has been proposed by various platform designers. A study on design calculations for FOWTs can be found in (Dwyer, Viselli, Dagher, & Goupee, 2017). The properties of the TripleSpar concept are summarized in (Lemmer, Amann, Raach, & Schlipf, 2016). The concept has already been published in a version prior to the publication of the present document to be used by the scientific community and can be downloaded from (Lemmer, Amann, Raach, & Schlipf, 2016). It was used, for example, for the first studies in the EU Horizon2020 project LIFES50+, see (Lemmer, Müller, Pegalajar-Jurado, Borg, & Bredmose, 2016).

As part of the design process extensive parametric studies were performed to investigate the sensitivities of the hull shape geometry (column diameter, column radius column spacing) with respect to the overall dynamic behaviour. This is based on panel-code calculations, before starting the detailed structural design phase, presented in Chapter 7. In the following section the geometry with the “tripod” steel structure connecting the columns with the tower will be analysed, followed by the hydrostatic and hydrodynamic conceptual calculations.

### 4.1 Parametric design of the steel tripod

Figure 3 shows the platform geometry and the possible range of its dimensions. The concrete spar elevation above SWL is 10 m to avoid green water loads on the steel structure. The column radii were considered in the range of 5 to 15 m and the column distance to the vertical centerline between 10 to 35 m, see Figure 3. The wall thickness of the concrete columns was set to 0.4 m, aligned with (Molins, Campos, Sandner, & Matha, 2014).



**Figure 3 - Platform geometry.**

For the first conceptual parametric studies, a number of assumptions has been made to come up with reasonable dimensions for the detailed design, presented in Chapter 7. The tripod design is based on the transition piece of the Bard “Tripile”, a steel structure for the bottom fixed Bard 5MW wind turbine, see Figure 4 . It consists of three cylinders that are connected by square-shaped bars. While the bard transition piece is permanently bonded to three piles by a grouted connection, the Triple-Spar tripod will be connected to the three concrete spars.



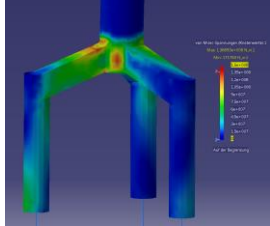
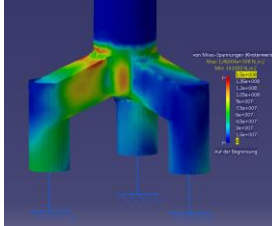
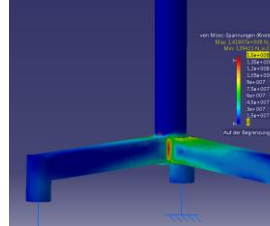
**Figure 4 - Transition piece of the Bard tripile support structure.**

The mass of the Bard transition piece is 490t, see (Bard Offshore, 2009), which leads to a wall thickness of about 5cm. Based on this geometry, CATIA FEM analysis were performed to upscale the tripod for the 10MW turbine.

The maximum horizontal force at the tower top of the DTU 10MW turbine is 4,605kN (Bak C. , et al.). Because the Bard structure was designed for a 5MW turbine, the maximum force at the bard tower was assumed to be 2,303kN according to (Jonkman, Butterfield, Musial, & Scott, 2009). This leads to a maximum stress of 139 N/mm. In the next step two tripods at distances of 10m and 35m were designed to match this maximum stress. For the other considered distances, the bar height and wall thickness were linearly interpolated. Table 5 shows the geometry data for the Bard transition piece and the smallest and the largest tripod.

The Tripod geometry has a large influence on the platform cost, because the steel for the structure is much more expensive than the concrete for the cylinders. It has also an effect on the platform center of mass and its mass moments of inertia.

Table 5 - Tripod geometry data.

	Bard transition piece	Smallest Tripod	Largest Tripod
			
Column distance to center	10 m	10 m	35 m
Tripile bar section height	3 m	5 m	7 m
Wall thickness	0.05 m	0.05 m	0.06 m
Max hor. force	2 303 kN	4 605 kN	4 605 kN
Max stress	139 N/mm	146 N/mm	142 N/mm
Mass	490 t	447 t	1 716 t

#### 4.1.1 Parametric spreadsheet calculations

The platform pitch angle at rated wind speed is constrained to 3.5°, independent of the parametric variations of the hull shape. Consequently, for every set of column radius and distance the draft was calculated as to match the constant stiffness of 2.922e9 Nm/rad. This is the same value as the one assumed in the previous deliverable, (Sandner, et al., 2014).

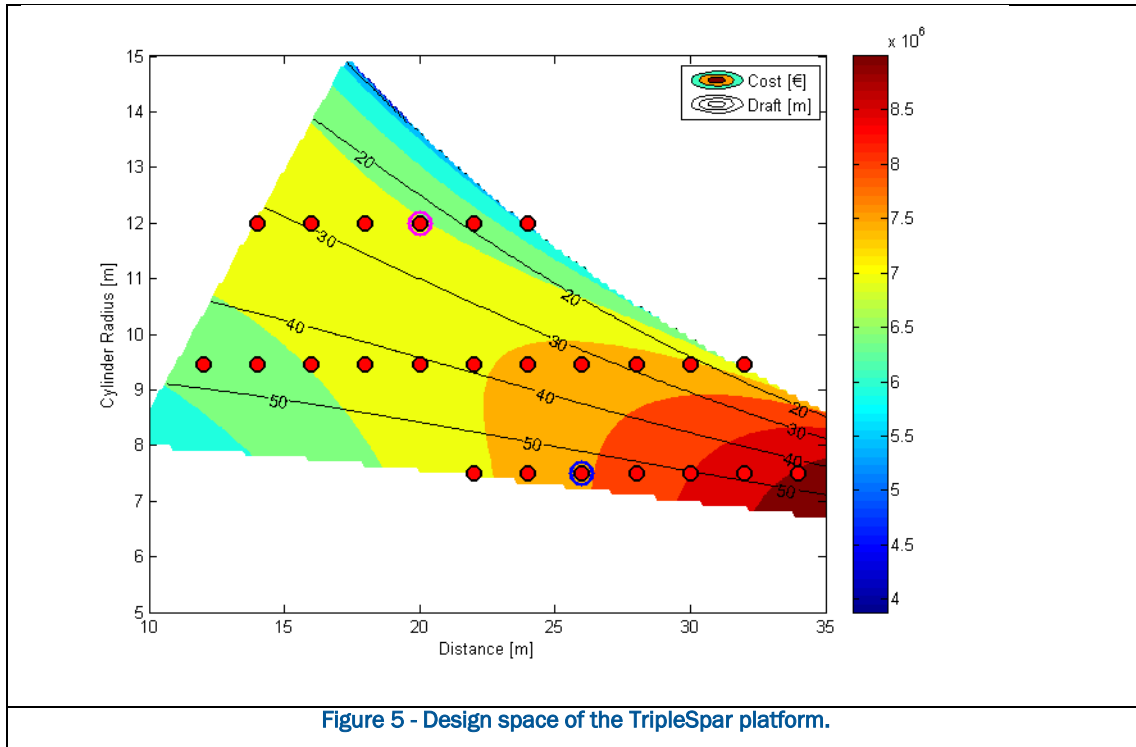
Figure 5 shows the platform draft and material cost over radius and distance. The left limit of the design space is defined by the minimum distance between two columns. In the upper right the draft becomes too small for a stable platform, whereas the lower limit is defined by the draft limit of 60 m.

The material cost for processed steel is assumed to be 4 k€/t and for processed concrete 236 €/t. With these values the platform cost depends more on the distance than on the radius, due to the expensive steel tripod. A higher distance means a larger tripod with higher wall thickness. So the platform cost limits the design space to the right, see Figure 5.

#### 4.1.2 Parametric hydrodynamic panel code simulations

The potential flow hydrodynamics were calculated with Ansys Aqwa for three different column radii. The red markers in Figure 5 show the reduced design space for the hydrodynamic calculations. Each marker represents a combination of a column radius and a column distance (to the vertical platform centerline). Furthermore, the figure shows the cost contour in color and the numbered contours representing the draft of the platform. The marker with the blue circle denotes the selected dimensions of the TripleSpar. This selection is due to the panel code calculations which show limitations due to the natural periods of the platform. Specifically, when increasing column radii, the platform pitch natural period becomes smaller than the limit of 25s, see Figure

6. This limit is necessary to avoid resonances from the wave excitations, see e.g. (Chakrabarti, 2005). The design with the red circle (with low draft and large radius) was initially selected for further calculations and comparisons for benchmarking studies of the TripleSpar.



Additionally, thin heave plates at the bottom of the columns have also been analysed for the concept with large draft and smaller column diameter. Figure 6 shows draft, platform cost and the period of the maximum RAO for the reduced design space in the three plots. For the two larger radii, the maximum RAO is within the wave spectrum of 10 s to 25 s, see red line in the lower plot.

By adding heave-plates to the three columns with a diameter of 1.5 times the column diameter, the period of the maximum RAO could be slightly increased for all configurations (dashed lines in Figure 6). While the heave-plates have no effect on the calculated draft, the platform cost increases due to the higher amount of steel. In the detailed design, concrete heave plates are proposed instead, see Section 7.3.8.

Figure 7 shows the mesh in Ansys Aqwa (Ansys, 2009) for the calculation of 1<sup>st</sup> order radiation and diffraction forces. This is the input for FAST calculations, see (NWTC, NWTC Information Portal (FAST v8), 2016). For the coupled FAST simulator the hydrodynamic coefficients need to be calculated with the SWL as reference point. The coefficient of added mass is shown in Figure 8, the coefficients of radiation damping in Figure 9 and the one for the first order wave excitation in Figure 10. These results have been converted from the format of Ansys Aqwa to the one of Wamit (Lee, 1998).

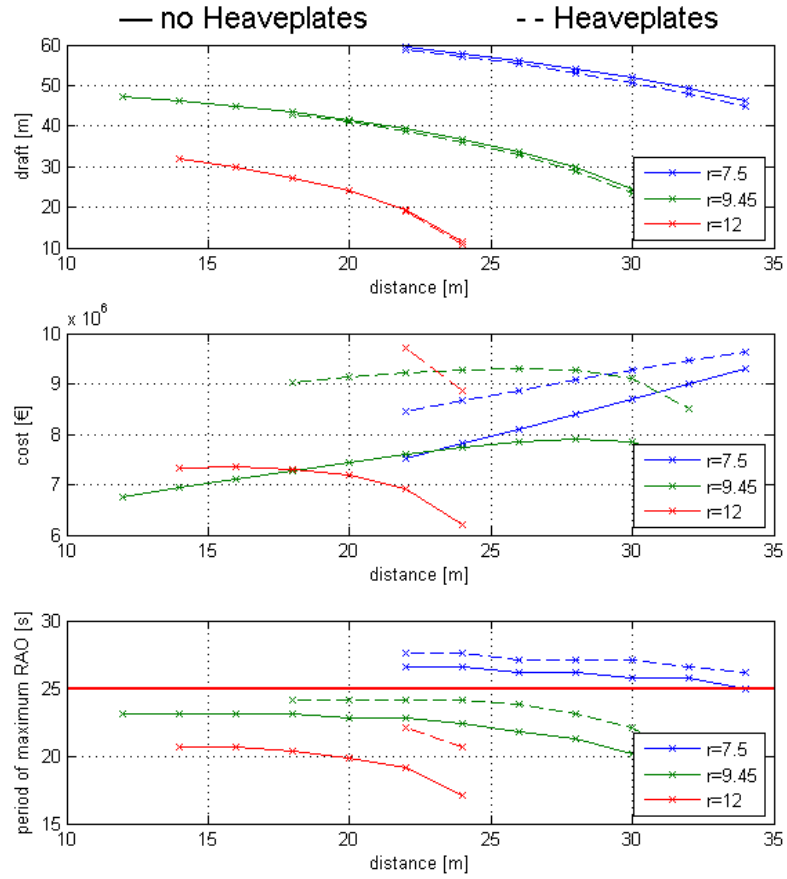


Figure 6 - Draft, cost and maximum RAO period for the reduced design space.

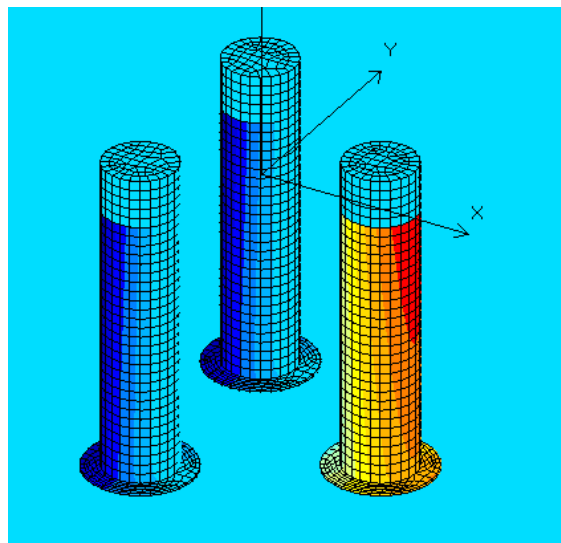


Figure 7 - Mesh in Ansys Aqwa for 1<sup>st</sup> order radiation and diffraction calculation.

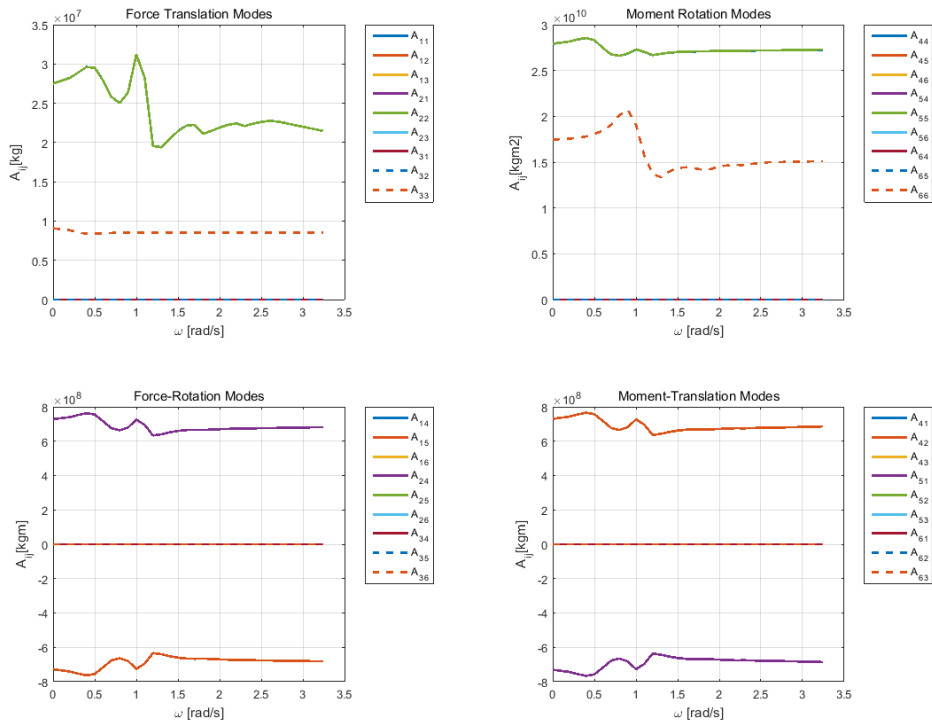


Figure 8 – Ansys Aqwa: Added mass.

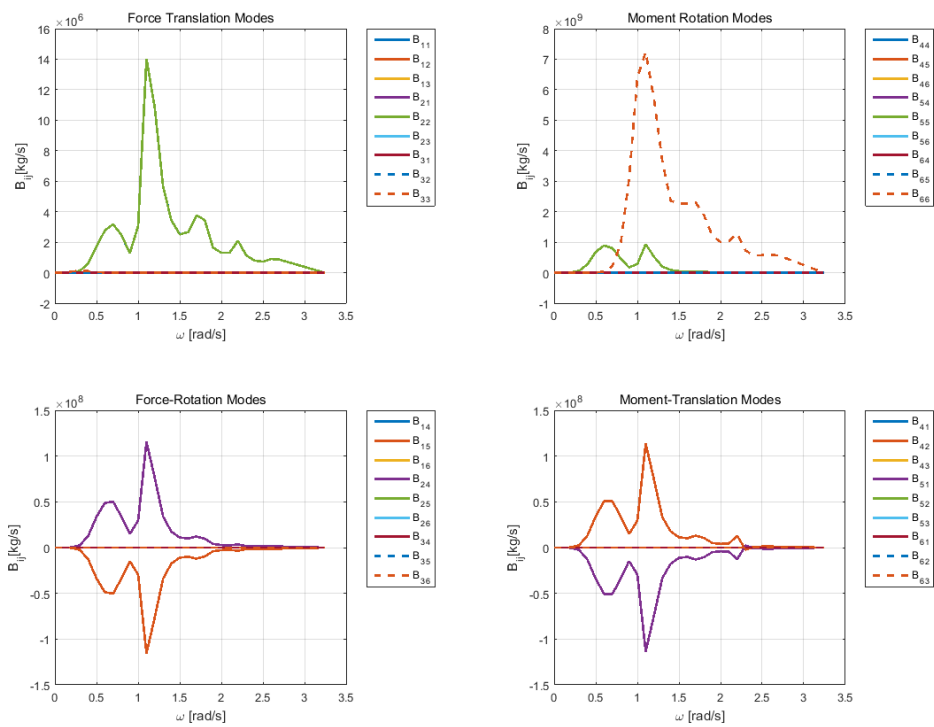


Figure 9 – Ansys Aqwa: Radiation damping.

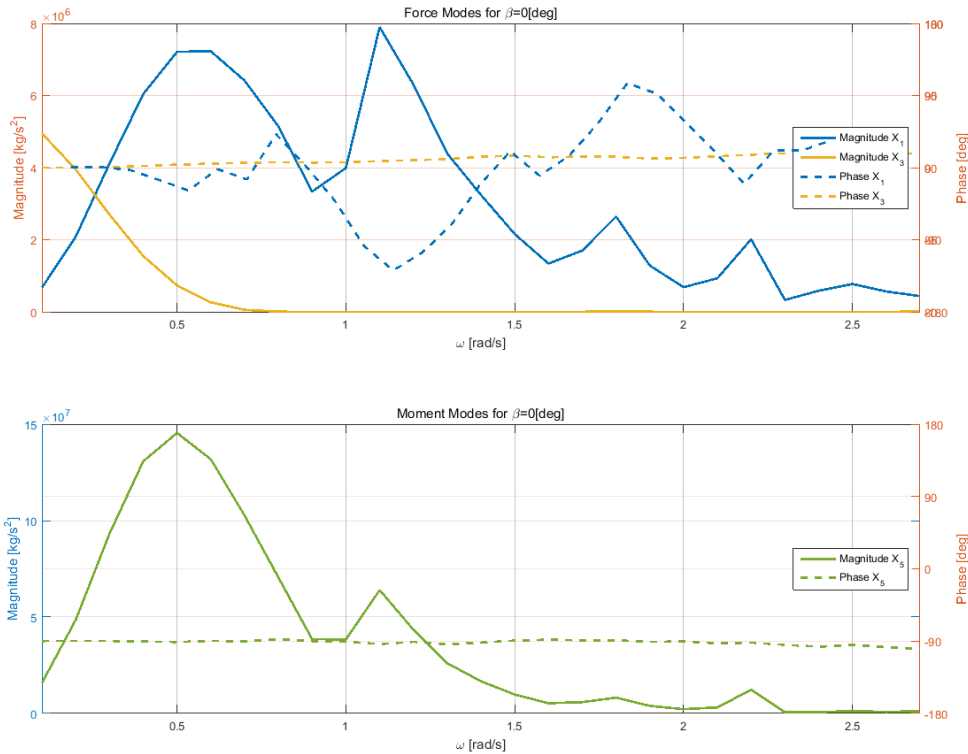


Figure 10 – Ansys Aqwa: Incident wave and diffraction forces.

Table 6 - INNWIND.EU TripleSpar concept properties.

Platform	Draft	54.464 m
	Elevation of tower base above SWL	25 m
	Water displacement	29 205.09 m <sup>3</sup>
	Center of mass below SWL	36.0176 m
	Center of buoyancy below SWL	27.5381 m
	Platform mass	2.822863e7 kg
	Ballast mass	17 264 t
columns	Length	65 m
	Distance to the center	26 m
	Diameter	15 m
	Elevation above SWL	10.5 m
Heave plates	Thickness	0.5 m
	Diameter	22.5m
	Mass	678.7t
Tripod	Total height	15 m

	Height outer cylinder	11 m
	Diameter outer cylinder	5.64 m
	Bar cross-section width	5.64 m
	Wall thickness	0.0564 m
	Mass	971.3 t
DTU 10MW RWT	Tower height above SWL	119 m
	Reduced tower length to hub height	94 m
	Rotor diameter	178.3 m
	Rotor mass	228 t
	Nacelle mass	446 t
	Reduced tower mass	433 t
	$I_{11}$ about turbine CM	1.613e9 kgm <sup>2</sup>
	$I_{22}$ about turbine CM	1.613e9 kgm <sup>2</sup>
	$I_{33}$ about turbine CM	0.491e9 kgm <sup>2</sup>
Densities	Concrete density	2 750 kg/m <sup>3</sup>
	Steel density	7 750 kg/m <sup>3</sup>
	Ballast density	2 500 kg/m <sup>3</sup>
	Water density	1 025 kg/m <sup>3</sup>
	Total platform mass	28268.22 t
Moments of Inertia about center of mass	Platform $I_{11}$ without turbine	1.8674e10 kgm <sup>2</sup>
	Platform $I_{22}$ without turbine	1.8674e10 kgm <sup>2</sup>
	Platform $I_{33}$ without turbine	2.0235e10 kgm <sup>2</sup>
	FOWT System $I_{11}$	3.907e10 kgm <sup>2</sup>
	FOWT System $I_{22}$	3.907e10 kgm <sup>2</sup>
	FOWT System $I_{33}$	3.1129e10 kgm <sup>2</sup>
Hydrostatics/Hydrodynamics	Heave stiffness $C_{33}$	5.321e6 N/m
	Pitch stiffness $C_{55}$	2.922e9 Nm/rad
	Pitch stiffness $C_{55}$ w/o gravitation (FAST)	-6.199e9 Nm/rad
Cost	Steel price	4 000 €/t
	Concrete price	236 €/t
	Ballast price	70 €/t
	Tripod cost	3.885e6 €
	Total platform cost	1.0296e7 €



Figure 11 – INNWIND.EU TripleSpar platform with DTU10MW reference turbine.

## 5 MOORING LINES

### 5.1 Design description

The mooring system keeps the platform at the desired location and avoids the drift caused by the wind, the currents and the nonlinear hydrodynamics. If possible, the resulting natural frequencies of the moored system have to be located outside of the dominant frequencies range of the wave spectrum to avoid dynamic excitations. In addition, the anchor should not experience vertical loads in any case.

A semi-taut design was selected to moor the Triple Spar platform to the 180m depth location. In the semi-taut configuration, the mooring cost can be reduced combining different materials in the same line. In this design, polyester, a common material in the oil & gas industry, is used in the upper part of the line and a steel chain is selected for the lower part, that comes in contact with the seabed. A 647kg/m chain was selected to provide enough stiffness to the mooring system.

On a first approach, the mooring system was dimensioned using the static catenary equations. A plane seabed was assumed. The stretching of the line is also assumed to follow Hooke's law. The elastic catenary equation was applied for the chain section coupled with an elastic taut equations for the polyester line; details on these equations can be found in (Barltrop, 1998) and (Journée & Massie, 2001). Figure 12 shows the semi-taut shape of one mooring line at zero platform excursion.

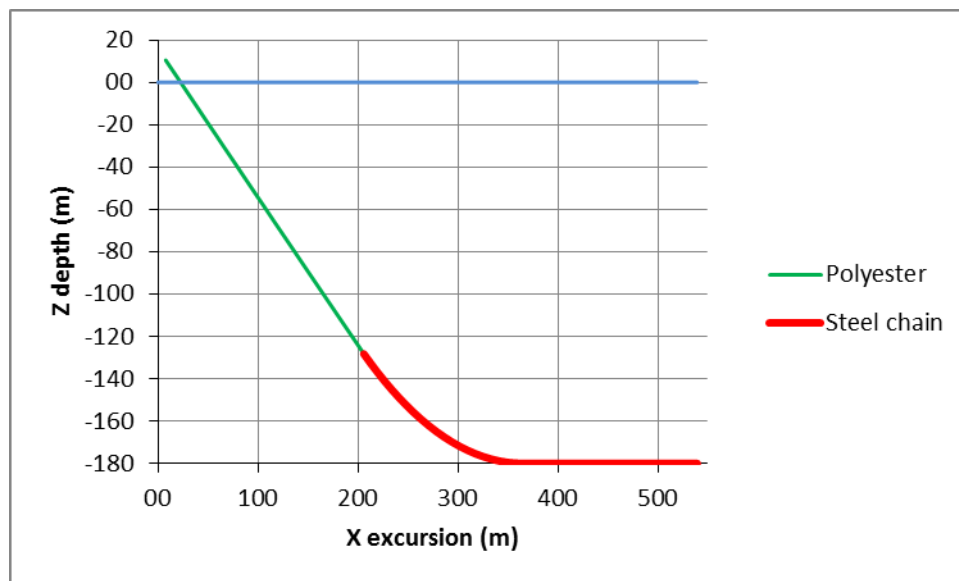


Figure 12 Semi-taut configuration for zero surge

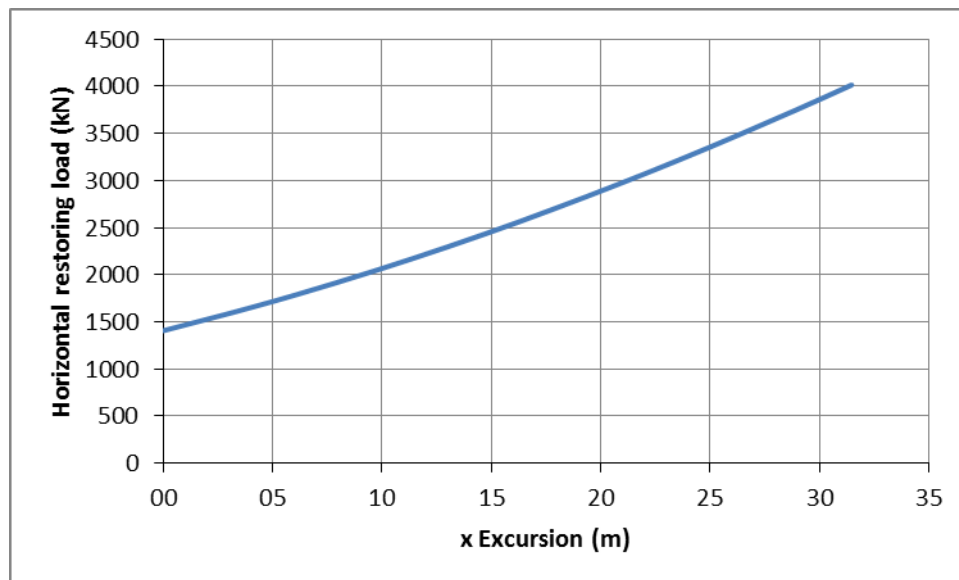
Figure 12 shows that the chain section lays on the seabed connected to the anchor meanwhile the polyester section at the upper part connects the platform fairlead to the chain. This configuration has been designed to avoid the contact of the polyester with the seabed that could damage the line due to friction.

Table 7 presents the main data of the designed mooring system.

**Table 7 Mooring line characteristics**

Fairleads above MSL	10.5 m
Number of lines	3
Pretension at fairlead	1700 kN
Fairlead radius position	33.5 m
Anchor radius position	572.9 m
Chain nominal diameter	0.180 m
Chain equivalent diameter	0.324 m
Chain weight/length in water	5526.9 N/m
Chain weight /length in air	6350.0 N/m
Chain length	344 m
Chain axial stiffness	2.8 E6 kN
Polyester nominal diameter	0.200 m
Polyester equivalent diameter	0.151 m
Polyester weight /length in water	60.0 N/m
Polyester weight /length in air	240.0 N/m
Polyester length	239 m
Polyester axial stiffness	4.32 E4 kN

Figure 13 shows the resulting horizontal force of the mooring system as function of the surge excursion of the platform. The mooring system has been designed to obtain a linear smooth curve that avoids snaps loads. The curve shows that the semi-taut system is able to counteract the rotor design thrust force of 1500kN at rated wind speed and also the design extreme wind load of 2050 kN (Bak C. , et al., 2013). The maximum allowable excursion is 31.5m. Beyond this excursion the line at the seabed aligned with the direction of the excursion would lift up and the anchor would experience vertical force.



**Figure 13 Horizontal mooring force as function of the excursion**

The angle between the water plane and the mooring line is 55.8deg, based on this steady calculation. This angle should not reach 86.7deg to avoid the contact between the line and the heave plate at the base of the platform columns. The maximum value of this angle will be verified afterwards, based on dynamic simulations.

The stiffness of the mooring system was designed to obtain natural period of the platform out of the dominant frequencies of the wave spectrum (4s-25s). This was not possible for the heave motion, because the contribution of the mooring system to the heave stiffness is low. The heave plates at the bottom of the columns damp this motion. Table 8 shows the resulting natural periods of the platform that were obtained by free decay's tests using FASTv8 (National Renewable Energy Laboratory, 2016)..

**Table 8 Damped natural periods of the moored platform**

DoF	Td [s]	fd [Hz]
Surge	166	0.006
Sway	166	0.006
Heave	16.8	0.059
Roll	25.5	0.039
Pitch	25.5	0.039
Yaw	99.65	0.010

## 5.2 Mooring line design dynamic verification

The dynamic performance of the mooring system under the loads of wind, wave and currents is verified in this Section. A set of 16 load cases, considered the most critical, were selected based on the recommendations by (Chaviaropoulos, Karga, Harkness, & Hendriks, 2014). These cases are defined based on the standard IEC 61400-3 (I.E.C, Wind Turbines-Part 3: Design Requirements for Offshore Wind Turbines, IEC 61400-3., 2008). Table 9 shows the load cases selected to verify the mooring lines design.

Table 9 Reduced design load cases

Cases	DLC	Description	Wind speed [m/s]	Waves		Sea current [m/s]	Wind - Wave misalignment $\beta$ (deg)	Simulation length [s]
				Hs [m]	Tp [s]			
1	1.6	Power production	9.4	10.9	14.80	0.154	0	3600
2			11.4					
3			13.4					
4			20					
5			25					
6	2.2	Power production plus fault occurrence	11.4	4.45	7.47	0.154	0	500
7		20	10.3	11.37				
8	6.1a	Parked or idling	44m/s x 0.95 [k1]	10.9 x 1.09 [k2]	14.80	1.13	-30	3600
9							0	
10							30	
11	7.1	Parked and fault condition (1 blade fails to pitch)	36.7m/s x 0.95 [k1]	7.7 x 1.09 [k2]	12.4	1.13	-30	1000
12							0	
13							30	
14							-30	
15							0	
16							30	

As this is a reduced set of load cases, the variation of mean sea level and rotor misalignment were not considered. Figure 14 represents the numbering of the three lines that compose the mooring system. Line 2 is aligned with the wind.

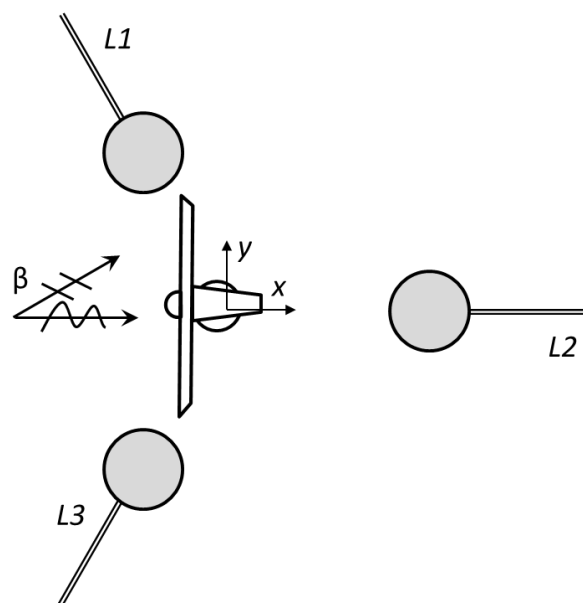


Figure 14 Floating turbine configuration for load analysis

The simulations were done using FASTv8. The mean drift effect was calculated based on the Newman approximation (Faltinsen, 1990). The sea current was modelled with a logarithmic velocity profile that reaches zero speed at 60m of water depth. Viscous forces were added on the platform columns using a Morison approach with a drag coefficient  $C_d=0.61$ . Mooring lines were simulated with a dynamic model based on lumped mass method that take into account tangential and also along the line drag and inertial forces. The drag coefficients used in the numerical model were obtained from DNVGL-OS-E301 (DNV-GL, 2015).

**Table 10 Normal and tangential drag equivalent coefficients.**

Section	$C_{dn}$	$C_{dt}$
(-)	(-)	(-)
Steel chain	1.333	0.633
Polyester	2.12	0

The results of these simulations were processed to obtain the largest platform motions and the extreme mooring line tensions and to confirm that the connection point is not reaching the seafloor and the anchor is not experimenting vertical loads in any case.

Table 11 present the largest (max) and the smallest (min) tension obtained from the simulations. These maximum and minimum values can be found on the diagonal of the table. The other values, out of the diagonal, correspond to the tension on the other lines when the extreme value is produced. The maximum tension of 4139 kN appears on line 1 caused by the case 6.1 that combines the extreme wind model with the severe sea state. This maximum tension is below the minimum breaking load (MBL) of the polyester line (13172 kN) and the steel chain (30689 kN).

**Table 11 Extreme fairlead tensions**

<i>DLC Case</i>			<i>L1</i>	<i>L2 (downwind)</i>	<i>L3</i>
			<i>kN</i>	<i>kN</i>	<i>kN</i>
Max	6.1	9	4139	1038	2649
Min	6.1	11	564	1048	2062
Max	1.6	5	1953	1808	1938
Min	7.1	13	3484	61.22	3181
Max	6.1	11	2757	1078	4033
Min	6.1	9	1885	1050	446.4

Table 12 shows the extreme displacements of the platform and the corresponding values of the others degrees of freedom. The maximum surge, pitch and yaw displacements are produced by DLC 7.1 (case 13), which is an idling case with misalignment between waves and wind with one blade that has failed to pitch to feather and is on a 0 deg position. The maximum pitch inclination (8.898 deg) and the maximum roll inclination (11.23 deg) are admissible values.

**Table 12 Extreme platform displacements**

	<b>DLC</b>	<b>Case</b>	<b>Surge</b> <i>m</i>	<b>Sway</b> <i>m</i>	<b>Heave</b> <i>m</i>	<b>Roll</b> <i>deg</i>	<b>Pitch</b> <i>deg</i>	<b>Yaw</b> <i>deg</i>
Max	7.1	13	34.45	0.1549	-0.8093	0.9146	6.366	-22.3
Min	1.6	5	0.95	-0.7278	-2.957	0.2824	-0.5783	-0.8101
Max	6.1	11	12.8	13.28	0.5088	-3.822	-2.208	-6.673
Min	6.1	9	13.52	-13.52	-1.237	4.235	-2.571	6.158
Max	6.1	9	20.58	-10.88	10.07	0.5411	1.885	8.49
Min	6.1	9	10.95	-11.49	-9.525	2.313	-6.129	8.179
Max	7.1	16	25.14	-2.596	0.02554	8.615	0.9995	-2.614
Min	7.1	16	24.77	6.757	1.319	-11.23	-1.381	-1.289
Max	7.1	13	30.47	4.454	-0.3299	-5.654	7.164	-14.05
Min	7.1	13	21.94	0.5785	0.6559	-3.052	-8.898	-4.904
Max	7.1	13	30.9	2.887	-0.3302	-1.499	-0.003231	18.81
Min	7.1	13	25.54	0.1854	0.5794	0.5208	-3.707	-25.31

The depth of the links between the polyester and the steel chain for the three mooring lines has been checked to ensure that there is no contact between polyester and the seabed. This contact would damage the polyester line due to friction. The lowest value, as can be seen in Table 13, was 165.6m below still water level for line 2, confirming that there is no contact between polyester and the seabed.

**Table 13 Connection node depth position**

	<b>DLC</b>	<b>Case</b>	<b>L1</b> <i>m</i>	<b>L2 (downwind)</b> <i>m</i>	<b>L3</b> <i>m</i>
Max	6.1	9	-101.7	-139.5	-118.9
Min	6.1	11	-142.2	-141.3	-118.2
Max	1.6	5	-127	-127.7	-125.7
Min	7.1	13	-110.2	-165.6	-112.3
Max	7.1	13	-123	-156.2	-101.2
Min	6.1	9	-117	-135.7	-142.9

Finally, it has been checked that none of the anchors experience vertical forces in any of the load cases computed.

In conclusion, this simplified load cases analysis showed that semi-taut mooring system has been successfully designed for seakeeping the 10MW turbine on the TripleSpar floating platform: maximum tensions are always below the MBL of the materials, the motions of the platform are moderate, the line is not hitting the heave plates, the polyester is not contacting the seabed and the anchors does not present vertical loads.

## 6 CONTROLLER

Due to the floating foundation the DTU10MW baseline controller cannot be used here because of the “negative damping” problem, which has been reported in the literature, see e.g. (Larsen & Hanson), (Fischer, 2012), (Veen, Couchman, & Bowyer, 2012).

When a lightly damped eigenmode of the floating support (surge, pitch) sits inside the wind turbine controller bandwidth, the apparent wind velocity due to floater motion combined with the negative wind speed to thrust relation, causes controller limit cycling and resulting poor performance. Several methods to deal with this issue have been investigated previously, such as reduction of controller bandwidth (Larsen & Hanson), individual pitch control (IPC) to provide damping of the floating support (Namik & Stol, 2010), state estimation and feedback/feedforward (Savenije & Peeringa, 2014), LiDAR to measure the apparent wind (Schlipf, Simley, Lemmer, Pao, & Cheng, 2015). In most of these studies, the focus has been on power and rotor speed regulation. The approach in this task is focused on load reduction, with a strategy that aims to minimize the variation of the thrust load.

Studies on the linear system characteristics and responses with different controllers analyzing the TripleSpar concept can be found in (Lemmer, Schlipf, & Cheng, Control design methods for floating wind turbines for optimal disturbance rejection, 2016).

The controller in this task has been developed with a dedicated wind turbine control design environment (Engels, Kanev, Savenije, & Wouters, 2013) that has been extended to allow design of floating wind turbine controllers. To obtain good controller behavior for all situations a (floating) wind turbine can encounter, several different loops work together, such as:

- baseline power and rotor speed regulation
- drivetrain and tower damping
- individual pitch control (IPC)
- extreme event control (EEC)
- reduced power operation

An overview of the controller structure is shown in Figure 15. In addition to these main control loops, the controller contains rotor speed dependent filters, observers for state estimation and actuator limitation. The sections below describe the design and initial evaluation of the main control loops.

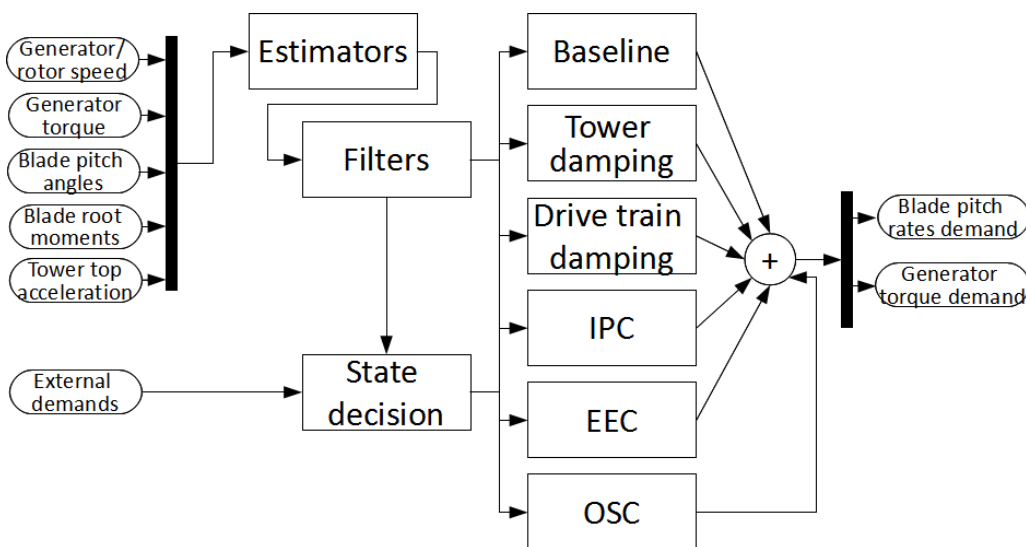


Figure 15 Structure of Advanced Control Tool

## 6.1 Controller design

The first section describes the required input processing in the controller (filtering, observers and wind speed estimation). The second section discusses the baseline controller algorithm and design. The following sections contain the load reduction add-ons.

### 6.1.1 Controller input processing

The controller applies filtering of the input depending on its usage. Figure 16 shows the different low pass filters used for gain scheduling, peak shaving, pitch angle synchronization etc.

To reduce the time delay, but have sufficient reduction of harmonic (nP) components, rotor speed dependent notch filters are used in combination with a low pass filter for the main rotor speed feedback loop (Figure 17).

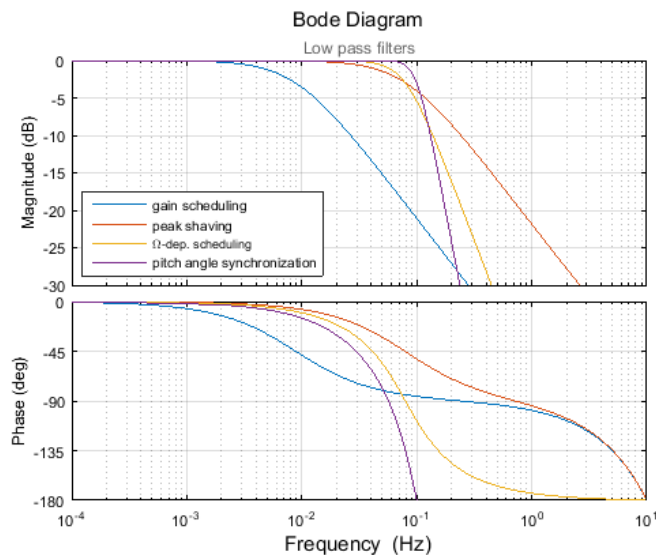


Figure 16 Input filtering

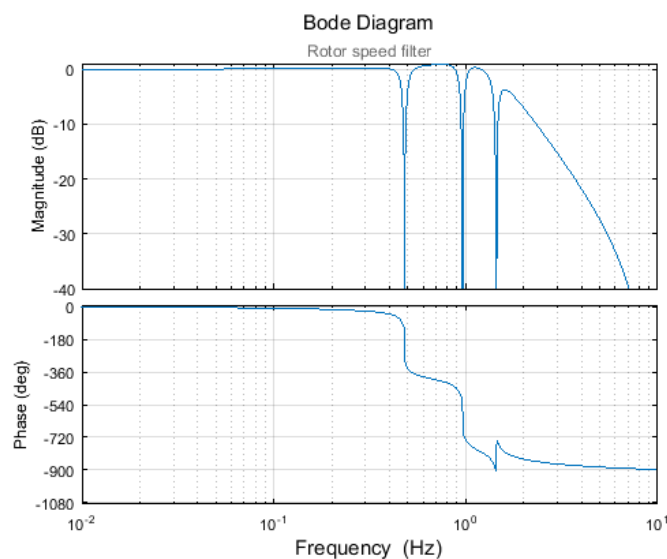


Figure 17 Rotor speed dependent filter

The controller uses (extended) kalman filters on the drive train and tower components, to estimate the states required for the damping loops.

A special type of observer has been developed to estimate the wind speed felt by the rotor, based on the principle described in (Van der Hooft & Van Engelen, 2004). The estimated wind speed is amongst others used for gain scheduling and peak shaving.

### 6.1.2 Baseline power and rotor speed regulation

As most modern wind turbine controllers, the baseline controller works in two regions (below and above rated wind speed) connected with a transition region. Below rated, the focus is on maximum power capture using variable speed generator torque control. Above rated, the baseline control loop takes care of power and rotor speed regulation with collective blade pitch control.

The operating curve governs the setpoints of the controller, and is derived using the rotor power (Figure 18) and thrust (Figure 19) coefficients provided by aero-elastic simulations. Figure 20, Figure 21 and Figure 22 show the quasi-static power, thrust and pitch angle curves. Moderate peak shaving is applied to reduce the thrust peak around rated.

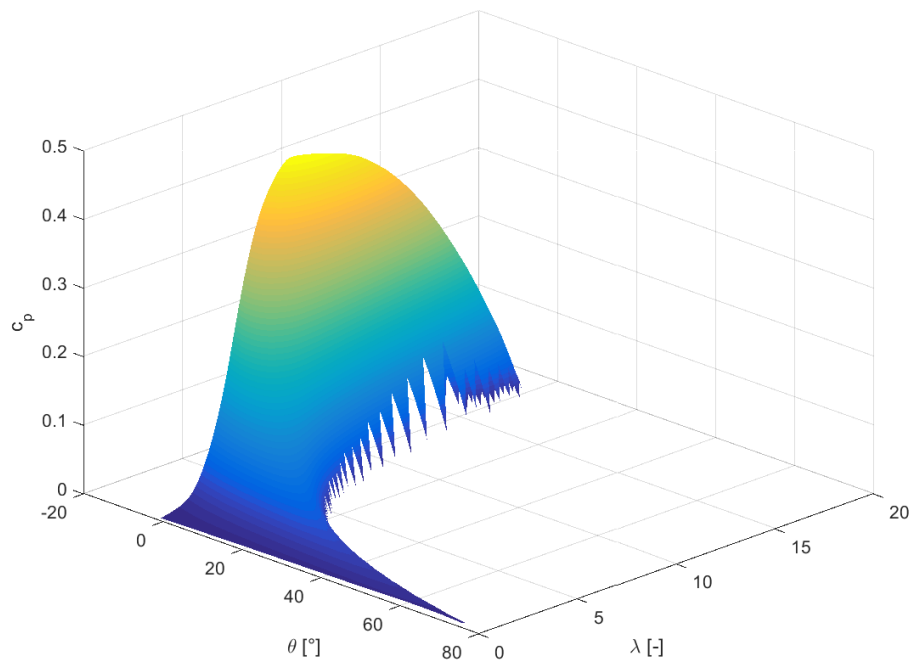


Figure 18 Rotor power coefficient

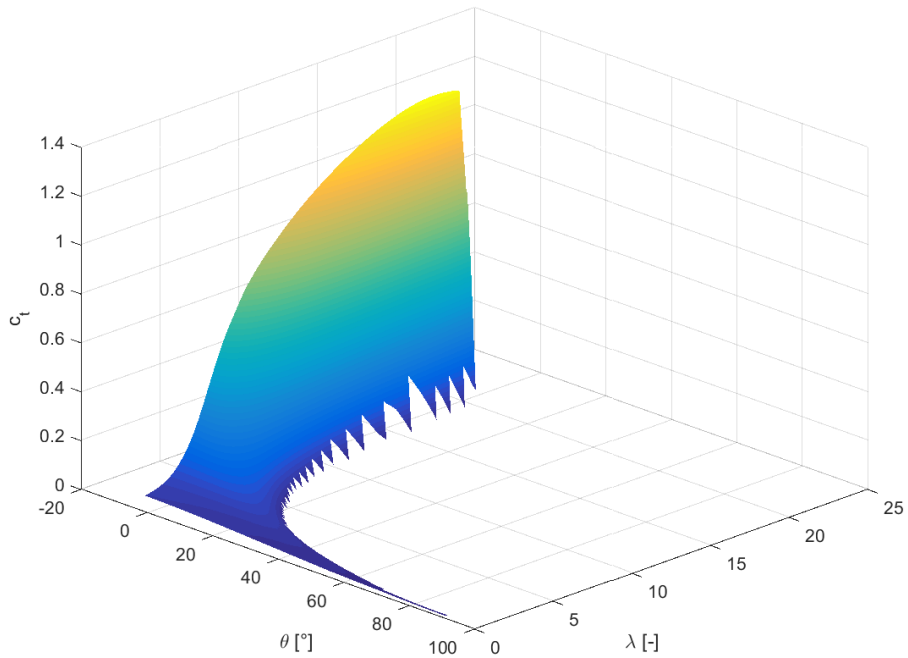


Figure 19 Rotor thrust coefficient

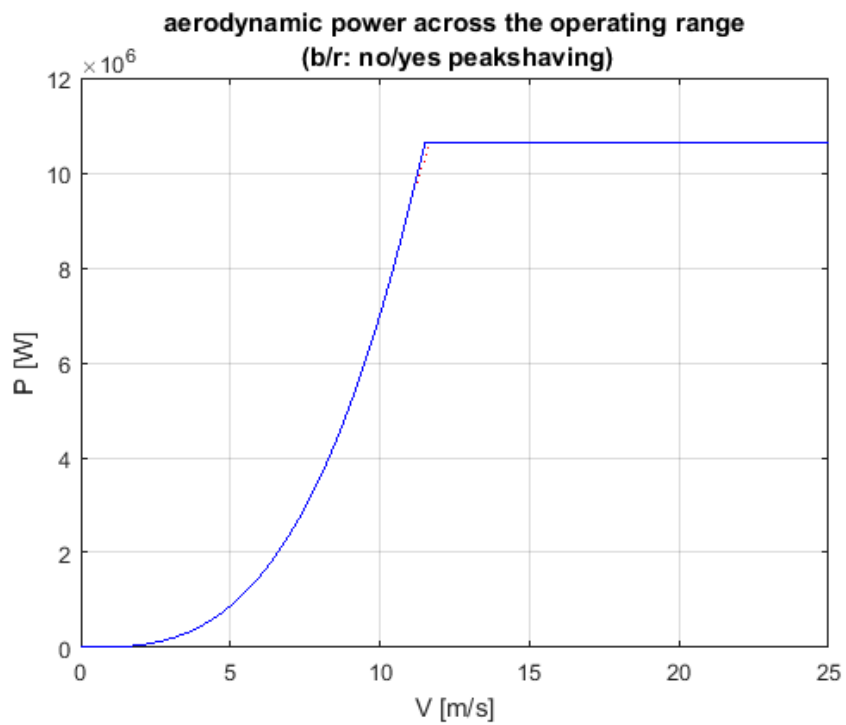


Figure 20 Power curve

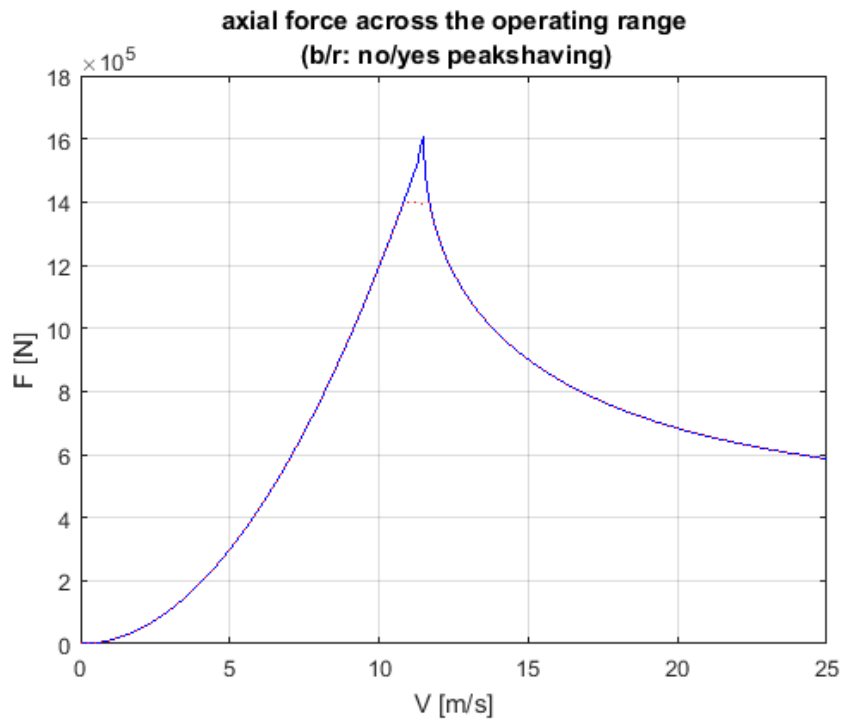


Figure 21 Thrust curve

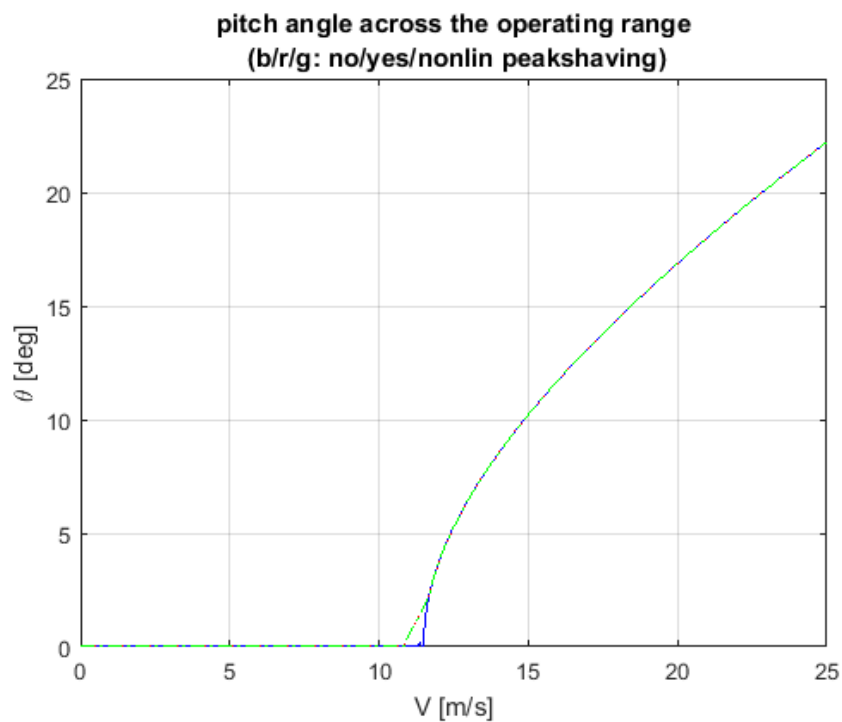


Figure 22 Collective blade pitch angle curve

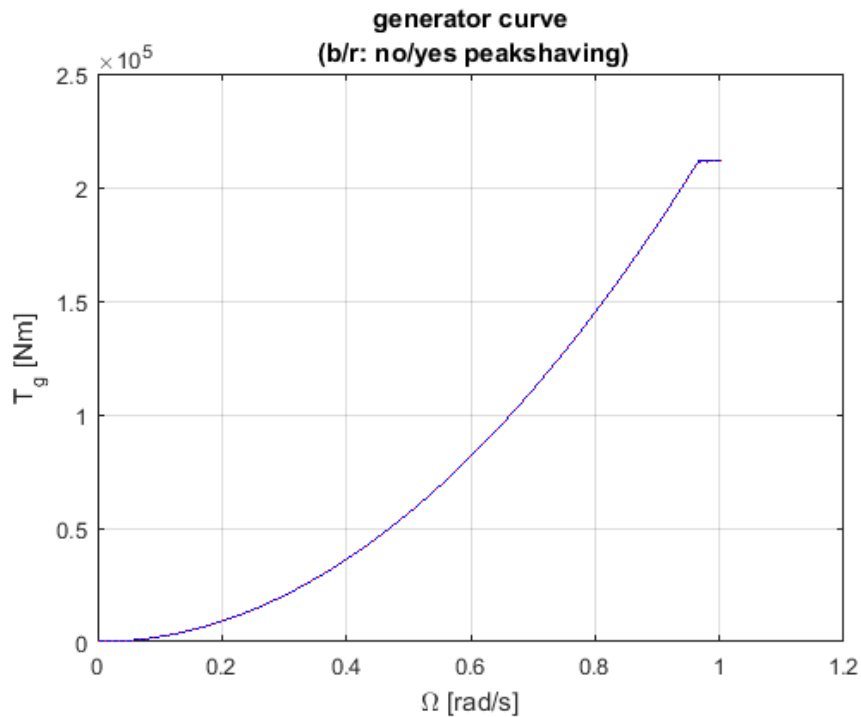


Figure 23 Generator torque curve

Below rated, a torque-speed relation (Figure 23) is derived from the operating curve that results in optimal tip speed ratio and maximum power coefficient. This relation directly provides the torque setpoint to be applied. Both at minimum and at rated rotor speed, the rotor speed is controlled using a PI feedback loop from generator speed to generator torque.

Above rated wind speed, a (PI) structured linear-quadratic regulator (LQR) controller is used from generator speed to collective blade pitch angle. The LQR design approach takes care of the gain selection that balances tracking performance and actuator effort. For floating wind turbines, the model input for the LQR design also contains a simple linear model of floater and mooring dynamics. The resulting gains are scheduled based on estimated wind speed as shown in Figure 24. Due to the low frequent eigenmodes of the floating support, the gains are lower than for a conventional bottom fixed wind turbine controller. Step response of the system shows good stability, but the low gains result in reduced tracking performance. To counter this, and reduce thrust fluctuations at the same time, a loop that smoothens the thrust fluctuations has been added.

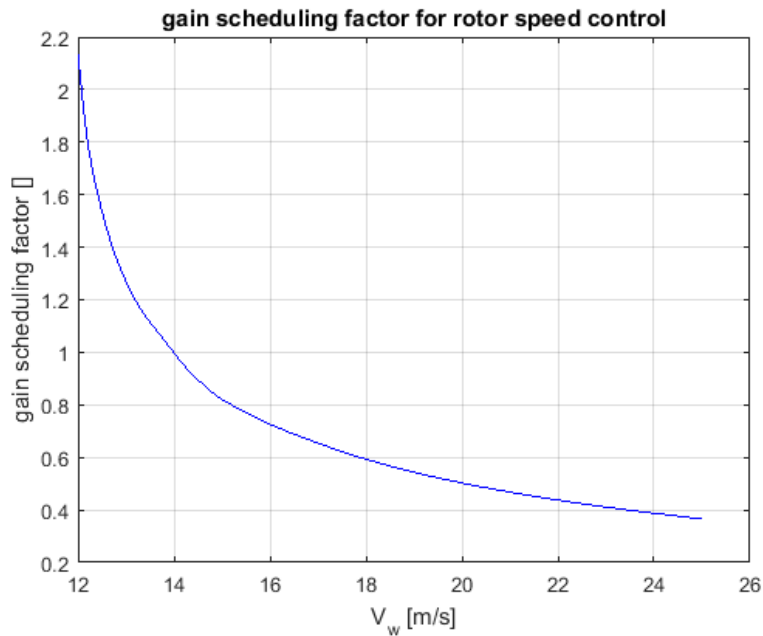


Figure 24 Gain scheduling

### 6.1.3 Drive train damping

Torsional vibrations in the drive train are due to the different flexibilities that exist between point of application of the aerodynamic torque (from the wind) and the generator torque. For the InnWind 10MW RWT with a main shaft and gearbox setup, both a collective blade mode and a shaft torsional mode are present. These can be suppressed using state feedback from the drive train observer to generator torque. Figure 25 shows the response when damping of the collective rotor mode is applied.

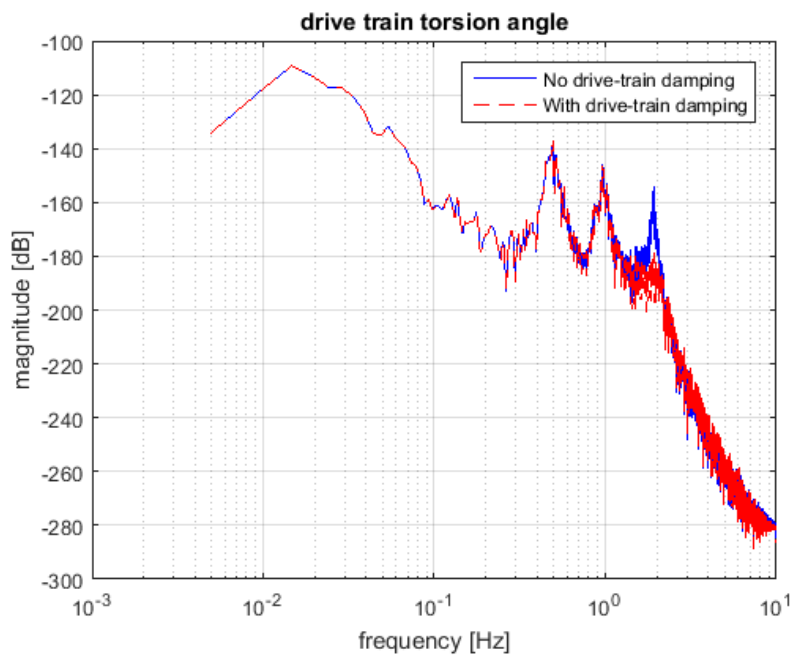


Figure 25 Drive train damping (collective rotor mode)

### 6.1.4 Tower damping

The wind turbine controller can be used to reduce the tower vibrations:

- fore-aft tower damping using collective pitch angle
- sideways tower damping using generator torque

Both use observers based on kalman filter and state (tower top position and velocity) feedback. Care must be taken in case of a floating support to design for the correct frequency of the coupled tower mode. Figure 26 shows the effect of sideways tower damping.

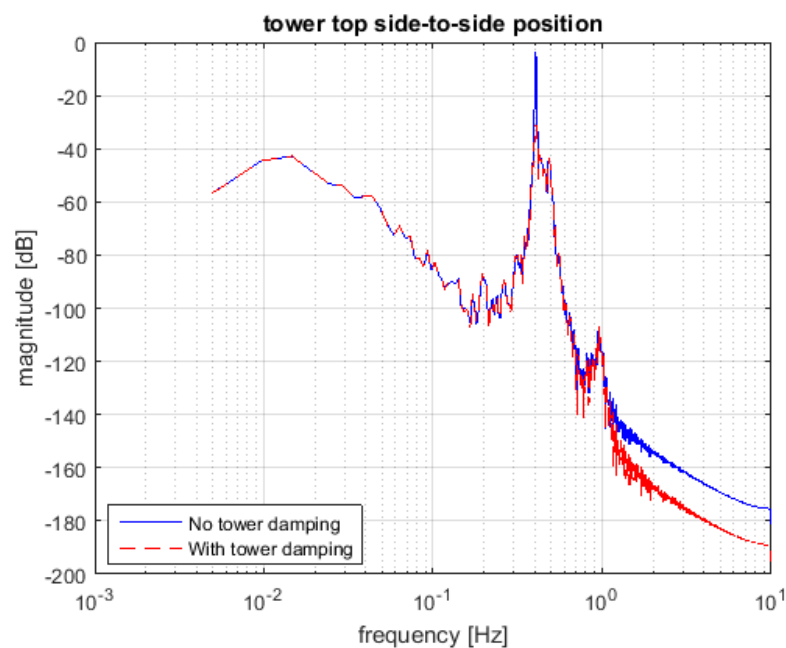


Figure 26 Sideways tower damping

## 6.2 Controller evaluation

Controller evaluation is typically done at several levels:

1. Initial evaluation in control design environment with simplified model
2. Fine tuning of the controller with aero(-hydro)-elastic code on limited set of relevant design load cases
3. Final numerical evaluation of the controller with aero(-hydro)-elastic code on a complete set of relevant design load cases

After this, implementation, testing and certification can follow.

Each step involves design iteration for the controller, and if required, for the wind turbine and the floating support structure.

As mentioned, focus for controller development and design in this task is on the loads reduction. Main loads of interest are the out of plane blade root bending moments, the rotor axial force (thrust) and the fore-aft tower base bending moment. Below the three stages are briefly described.

### 6.2.1 Initial evaluation and tuning in ACT

To verify the response of control algorithms to different environmental conditions or model parameters and to perform first tuning, a simple simulation setup covering the relevant dynamics

and external loading is most practical. The simulation environment in ACT has been extended with a basic model of the floating support. It allows 6DOF rigid body motions of the floater with a hydrostatic stiffness matrix and linear damping matrix. The mooring can be modelled using a linear stiffness matrix or with a quasi-static catenary mooring model. The latter is useful to check interaction between controller and mooring in different operating points (offset of the floater with respect to the origin). The wave loads are provided using a JONSWAP spectrum and the force RAOs from a potential flow panel code.

With this fast simulation setup, quick iteration can be performed to assess the effect of algorithm changes and tuning.

Main findings/adjustments from this evaluation step are the following:

- Tuning of the baseline control filters
- Improve filtering of the estimated axial force for thrust smoothing (minimize time delay)
- Including measured loads benefits the thrust smoothing

### 6.2.2 Controller assessment and tuning with FAST

After the initial evaluation of the controller behaviour in the control design environment, a detailed assessment has been performed with the aero-hydro-elastic time domain code FAST. To enable such coupled time domain simulations, the controller has been compiled into shared library for Windows (\*.DLL) and Unix (\*.SO). The model used in FAST is described in (Lemmer, Amann, Raach, & Schlipf, 2016), but with updated properties for the mooring lines and the floater.

The dynamic behaviour of the controller floating wind turbine in FAST has shown to be comparable with the response found from the simple model simulations.

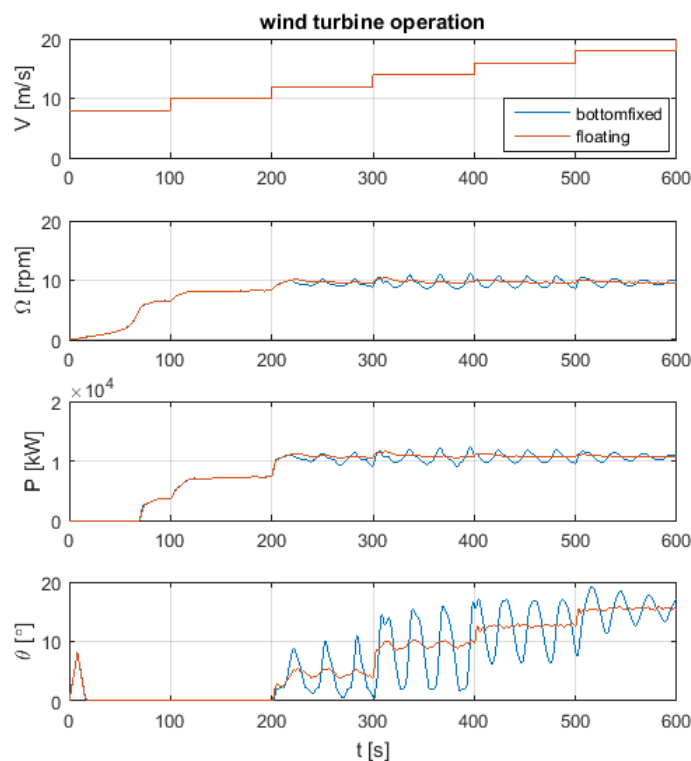


Figure 27 Wind turbine operation for a wind staircase

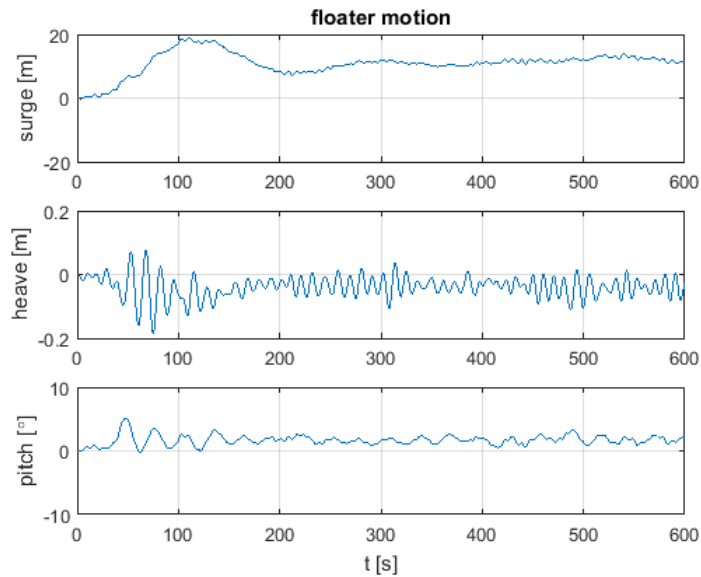


Figure 28 Floater response in 14m/s turbulent wind and irregular waves

Improvements and checks done during this step:

- Tuning drive train and tower frequencies for damping loops
- Preliminary fatigue load analysis

### 6.2.3 Complete DLC evaluation with hGAST

Detailed design analysis of the coupled floating wind turbine including the controller can be found in Section 7.2. Results from this analysis indicate possibilities to improve the response during normal power production in extreme sea state (DLC1.6: NPP with NTM&ESS). This would be recommended as future work.

## 7 DETAILED DESIGN ANALYSIS

### 7.1 Introduction

In the present section, the structural design and verification of the TripleSpar concrete floater defined in (Florian Amann, Frank Lemmer) is performed with the structural analysis program SAP2000 v18.2. The design procedure accounts for the ultimate and the fatigue loading conditions (ULS and FLS) as presented in DLCs 1.3, 6.1 and 6.2 in IEC standard (I.E.C, Wind Turbines-Part 1: Design Requirements, IEC 61400-1 Ed. 3., 2005) (I.E.C, Wind Turbines-Part 3: Design Requirements for Offshore Wind Turbines, IEC 61400-3., 2008) for the ULS and in DLC1.2 for the FLS respectively. The structural design and verification refers to the following parts of the structure: a) the connection between the steel tripod and the concrete cylinders, b) the required reinforcement percentage in the concrete, c) the steel tripod and d) the heave plates. Moreover, the beam equivalent cross sectional characteristics are derived and the updated floater properties are provided, together with the first 8 natural frequencies of the coupled floating wind turbine. Time domain hydro-servo-aero-elastic simulations have been also performed using NTUA's tool hGAST in order to provide the necessary input to the FEM solver SAP2000. Lastly, NTUA's frequency domain hydrodynamic solver freFLOW is used in order to provide the hydrodynamic pressure on the wet floater surface.

### 7.2 Coupled hydro-servo-aero-elastic analysis

#### 7.2.1 Time domain simulations

Time domain hydro-servo-aero-elastic simulations have been performed using NTUA's tool hGAST (Riziotis & Voustinas, 1997) (Manolas D.I., 2014) in order to estimate the ultimate and the fatigue loads of the coupled floating structure. For the coupled analysis, the site conditions have been defined in Section 2, the wind turbine in Section 3, the concrete tri-spar floater in section 4, the mooring lines in section 5 and the controller in section 6. In Table 14 the list of the performed DLCs is given. Each case corresponds to 1hour simulation. For the fatigue case (DLC1.2) one seed has been simulated for each wind speed, while for the ultimate cases (DLC1.3, 1.6, 6.1, 6.2) three. For the parked DLC6.1 two wave directions have been considered (0°, 30°), while for DLC6.2 three yaw angles (-30°, 0°, 30°) respectively. In the latter DLC the wind and the wave are co-directional.

DLC	Wind	Wave	Seeds	Bins [m/s]	Yaw	Wave	SF
1.2	NTM	NSS	1	5, 7, 9, 11, 13, 15, 17, 21, 23, 25	0	0	
1.3	ETM	NSS	3	11, 25	0	0	1.35
1.6	NTM	ESS	3	11, 13, 17, 21, 25	0	0	1.35
6.1	EWM	SSS	3	41.8	0	0, 30	1.35
6.2	EWM	SSS	3	41.8	0,+/-30	=Yaw	1.10

Table 14: DLCs definition for time domain simulations.

Wind turbine class	C
50-year significant wave height (m)	10.9
50-year sea-state peak period (s)	9.-16 -> 14.8
Design Depth (m)	180

Table 15: Characteristic met-ocean conditions for Site B.

DELS													
		5m/s	7m/s	9m/s	11m/s	13m/s	15m/s	17m/s	19m/s	21m/s	23m/s	25m/s	Overall
BLADE ROOT [kNm]	edge	21915	22666	23818	24404	24593	24580	24723	24870	25159	25352	25619	23595
	flap	5391	9079	12988	15246	22527	24309	26333	27845	29408	31322	32775	23492
	torsion	289	285	280	299	381	392	398	401	404	414	425	351
TOWER BASE [kNm]	side	4998	7952	25205	52386	37596	47203	57148	66146	73323	83698	98065	45494
	fore	107349	115225	136032	165190	194429	200614	212691	226805	250090	271595	291930	169422
	yaw	4305	6144	9188	12434	16230	18442	20205	22143	23860	25479	27031	14941
FAIRLEADS [kN]	axial1	77	125	177	171	235	156	148	150	162	179	194	165
	axial2	132	190	225	150	253	173	156	163	182	201	220	190
	axial3	76	127	177	176	241	166	157	159	169	179	190	169
ACHORS [kN]	axial1	73	117	167	163	220	148	141	143	156	174	189	156
	axial2	126	176	202	137	223	160	147	156	176	198	220	172
	axial3	73	120	167	166	227	156	148	151	162	173	184	160

Table 16: Lifetime DELs calculated for 20 years with Weibull parameters  $C=11$  m/s and  $k=2$ , Wöhler coefficient  $m=4$  for the tower and the mooring lines and  $m=10$  for the blades and  $n_{ref}=10^8$  cycles.

			DLC 1-2	DLC 1-3	DLC 1-6	DLC 6-1	DLC 6-2	Overall
BLADE ROOT	edge [kNm]	max	20564	26257	<b>27796</b>	13351	24458	27796
		min	-20573	-23443	<b>-24184</b>	-13725	-17121	-24184
	flap [kNm]	max	50897	57379	<b>90477</b>	36989	51903	90477
		min	-22561	-35035	-35410	-31034	<b>-43647</b>	-43647
	torsion [kNm]	max	373	460	862	380	<b>1030</b>	1030
		min	-520	<b>-633</b>	-627	-557	-612	-633
combine [kNm]	max	52571	60157	<b>91922</b>	37412	54124	91922	
TOWER BASE	side [kNm]	max	123278	172052	169597	390556	<b>415436</b>	415436
		min	-72747	-103379	-94964	-423189	<b>-439007</b>	-439007
	fore [kNm]	max	404347	472255	<b>838299</b>	685837	468121	838299
		min	-217003	-269563	-621861	<b>-741340</b>	-604501	-741340
	yaw [kNm]	max	30458	<b>43502</b>	34053	17261	26444	43502
		min	-37184	<b>-46804</b>	-44606	-18864	-28157	-46804
combine [kNm]	max	415494	474363	<b>838328</b>	747449	699522	838328	
FAIRLEADS	axial1 [kN]	max	3094	3476	4935	<b>5607</b>	4643	5607
		min	2146	2332	902	1161	<b>80</b>	80
	axial2 [kN]	max	2019	2077	<b>2945</b>	2112	1755	2945
		min	767	781	209	<b>96</b>	135	96
	axial3 [kN]	max	3274	3486	4883	<b>6890</b>	4587	6890
		min	2073	2157	767	288	<b>42</b>	42
ANCHORS	axial1 [kN]	max	2658	2997	4599	5259	<b>5932</b>	5932
		min	1776	1926	<b>0</b>	3	1	0
	axial2 [kN]	max	1670	1724	3155	<b>4542</b>	2519	4542
		min	561	569	<b>0</b>	0	0	0
	axial3 [kN]	max	2830	3005	4521	<b>6634</b>	6064	6634
		min	1704	1762	<b>0</b>	1	1	0

Table 17: Ultimate loads of the coupled tri-spar floating wind turbine (safety factors applied).

The tri-spar floater is designed for a medium site (Site B, The Gulf of Maine, USA (Lopez) . The site conditions are summarized in Table 15.

In Table 16 the lifetime Damage Equivalent Loads (DELs) are given for the blade root, the tower base and the mooring lines at the anchor and the fairleads positions. The first columns present the DELs per wind speed, while the last column the overall lifetime DEL as defined by the Weibull distribution with  $C=11\text{m/s}$  and  $k=2$  respectively. Moreover by processing the DLC1.2 results using the same Weibull parameters, the overall lifetime power spectral density (PSD) of the 6 tower base loading (3 forces and 3 moments) is estimated. This will be the stochastic input at the upper part of the tri-spar floater in SAP2000 for the FLS analysis.

In Table 17 the ultimate loads at the same positions are given for all the simulated DLCs. The maximum tower fore-aft moment is depicted in DLC1.6 at 13m/s. The maximum fore-aft moment together with the other simultaneous loads are given in Table 18. The 1x6 vector is introduced in SAP2000 for the ULS analysis on the tri-spar floater.

Fx [kN]	7.472E+03
Fy [kN]	1.682E+02
Fz [kN]	-9.736E+03
Mx [kNm]	-5.186E+03
My [kNm]	<b>6.210E+05</b>
Mz [kNm]	3.679E+03

**Table 18: DLC1.6 at 13m/s, Hs=10.9m, Tp=14.8s. Maximum tower base fore-aft moment and simultaneous loads, applied on the tri-spar floater (SF=1.3).**

## 7.2.2 Eigen-value analysis

In Table 19 the first natural frequencies of the coupled system are presented (the 6 rigid body modes and the 2 tower modes) as computed by hGAST, considering the floater as rigid body and taking into account the gravity.

mode	Frequency [Hz]
floater surge	0.0063
floater sway	0.0063
floater yaw	0.0138
floater roll	0.0429
floater pitch	0.0429
floater heave	0.0604
tower side-side	0.3840
tower fore-aft	0.4016

**Table 19: Natural Frequencies of the coupled system.**

### 7.3 ULS analysis of the tri-spar Floater

#### 7.3.1 Description of modelling

The design and verification analysis of the tri-spar floater is performed using the FE Program CSI SAP2000 v18.2 (CSI, 2016). The structure is composed by the following parts:

- Concrete Cylinders
- Concrete Heave Plates
- Steel horizontal legs (steel tripod)
- Steel vertical columns (steel tripod)
- Steel Central Cylinder (central connection of the 3 horizontal legs of the steel tripod)
- Steel inclined tubes (concrete-steel connection)
- Steel horizontal ties (concrete-steel connection)

The materials used for the floater and the corresponding mechanical properties are presented in Table 20. For the concrete parts concrete C50/60 is selected and rebar B500C for the reinforcement, while for the tripod steel S450 is used.

Material	Unit Mass	Young's Modulus E	Shear Modulus G	Poisson's Ratio
	tn/m <sup>3</sup>	[kN/m <sup>2</sup> ]	[kN/m <sup>2</sup> ]	[-]
<b>C50/60</b>	2.750939358	37000000.0	15416666.67	0.2
<b>Rebar</b>	7.752647280	199947978.8	80769230.77	0.3
<b>S450</b>	7.752647280	210000000.0	80769230.77	0.3

**Table 20: Material Properties - Basic Mechanical Properties.**

The whole structure (concrete cylinders, heave plates and steel tripod) is modeled using thick-shell elements, while the inclined tubes and the horizontal ties (that form the concrete-steel connection) are modeled as linear beam-column elements. In total 64412 finite elements are used. The model in SAP2000 is shown in Figure 29.

In order to come up with a realistic model, the 6 rigid body modes of the floater should be included in the SAP2000 model. To this end the floater is not considered clamped, but in its reference point a generalized stiffness matrix is introduced, taking into account the linearized contribution from the mooring lines, the hydrostatics and the restoring due to gravity. In this respect, the base nodes of the structure are connected to a central joint, at which the following spring parameters are defined:

$$K_{tot} = \begin{bmatrix} 83.28 & 83.28 & 0 & 0.1794 & -2841.52 & 2.3808 \\ 83.28 & 0 & 0 & 2834.33 & -7.717 & -156.51 \\ 0 & 0 & 5381.41 & 0.7101 & 143.8 & 7.4522 \\ 0.1794 & 2834.33 & 0.7107 & 2927178 & 28.939 & 19703 \\ -2841.52 & -7.717 & 143.88 & 28.939 & 2926708 & -832.1 \\ 2.3808 & -156.51 & 7.4522 & 19703 & -832.1 & 269575 \end{bmatrix} \text{ (kN, m, rad)}$$

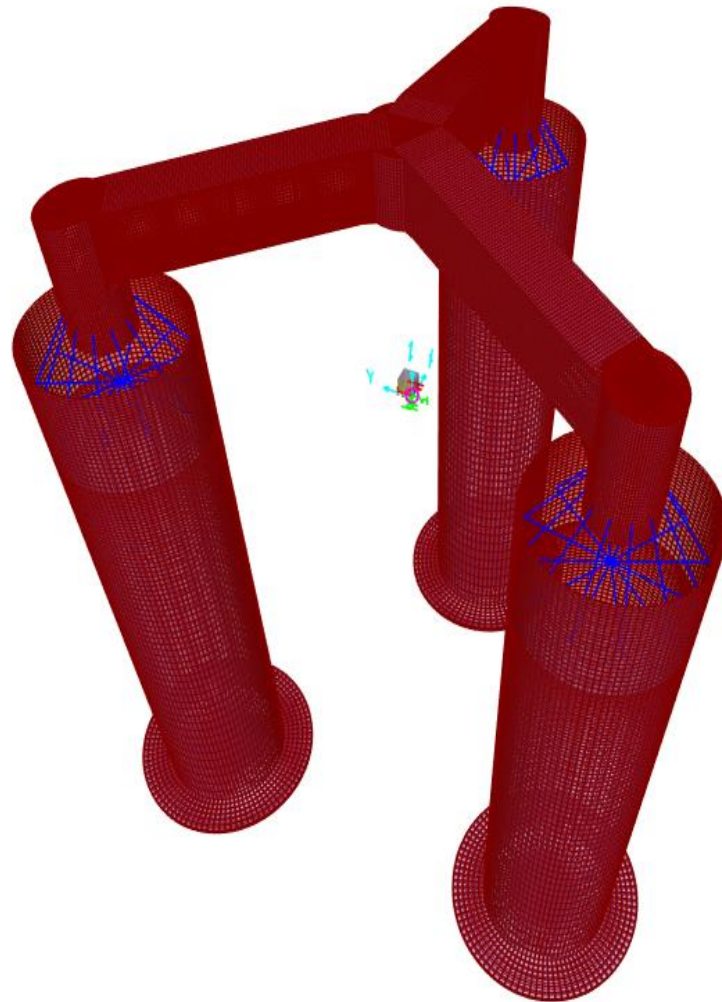


Figure 29: Floater FE model

### 7.3.2 Determination of the external (hydrodynamic) loading

Concerning the ultimate limit state, the external applied loading conditions introduced in the 3D FEM model, include the gravity force, the hydrostatic pressure, the maximum hydrodynamic pressure due to wave and current and the maximum loading from the wind turbine communicated through the tower base. The last one includes the contribution of the aerodynamic, the inertial and the gravitational loads applied at the WT tower base. The estimation of the gravity force and the hydrostatic pressure is trivial, while the maximum WT loading has been defined in Table 18 so the maximum hydrodynamic loading is detailed next. It is noted that a static solution is performed in SAP2000.

The hydrodynamic loading on the floater is taken into account by estimating the maximum normal pressure  $p_{\max}$  along the wet surface of the floater. The maximum normal pressure at every point  $\mathbf{x}$  on the surface floater is defined as:

$$p_{\max}(\mathbf{x}) = 1.86 \cdot p_{\text{sign}}(\mathbf{x}) = 1.86 \cdot 2 \sqrt{\int_0^{\infty} p(\omega; \mathbf{x})^2 S(\omega; T_p, H_s) d\omega}$$

where  $p_{\text{sign}}$  is the significant normal pressure,  $p$  the normal pressure at a point  $\mathbf{x}$  and frequency  $\omega$  and  $S(\omega; T_p, H_s)$  the wave spectrum. In the present analysis the Jonswap spectrum is used with parameters the peak period  $T_p$  and the significant wave height  $H_s$ , defined in Table 15.

For the estimation of the normal pressure  $p(\omega; \mathbf{x})$  the hydrodynamic problem is solved in the frequency domain using the in-house hybrid integral equation method freFLOW (Manolas, 2015). freFLOW solves the Laplace equation in 3D using the Boundary Element Method by adopting the indirect formulation with constant source distributions and by satisfying Garrett's analytic solution at the matching boundary. Verification of the method has been carried out by comparing against WAMIT (Lee, 1998) the hydrodynamic solution for the OC3 spar-buoy and the OC4 semi-submersible floater (Manolas, 2015). Due to the symmetry of the floater's geometry in the xz plane the computational domain is reduced to half, in order to reduce the computational cost. In total 18573 panels have been used, while the simulation is performed on 12 OMP threads.

The solution procedure provides the exciting loads, the added mass & damping coefficients, the RAOs of the floater, the surface elevation and the pressure along the floater surface. The latter is the input in the abovementioned equation. It is noted that for the RAOs estimation apart from the floater external geometry, the mass matrix of the floater, the stiffness matrix due to the moorings and the hydrostatics, as well as external mass, stiffness and damping matrices should be specified. The external matrices project the WT contribution on the floater's dofs and include the linearized contribution from the aerodynamic, the inertial and the gravitational loading on the WT parts. In the present analysis the aforementioned matrices have been defined using a simplified reduced order model of hGAST based on modal analysis and steady linearized blade element equations (Manjock, A., D. Manolas, F. Sandner and S. Voutsinas. (2014). INNWIND.EU D4.2.3: Integrated Design Methods and Controls for Floating Wind Turbines. Tech rep.). Thus the total 1<sup>st</sup> order hydrodynamic pressure applied on the floater can be estimated, taking into account the contribution from both the diffraction and the 6 radiation hydrodynamic problems and can be calculated only if the RAOs of the coupled floating structure are already known. So finally the estimated maximum (ultimate) hydrodynamic pressure is the external loading in the SAP2000 model.

In Figure 30 the RAOs of the tri-spar floater are presented for zero wave angle as a function of the wave frequency. Since the wave angle is zero the RAOs in sway, roll and yaw directions are excited due to couplings with the other directions mainly through the WT contribution (external matrices).

In Figure 31 the diffraction hydrodynamic loads are compared against the total hydrodynamic loads (including the diffraction and the 6 radiation hydrodynamic problems). The total surge force and the pitch moment are almost half of the diffraction ones, while the heave force remains almost unchanged.

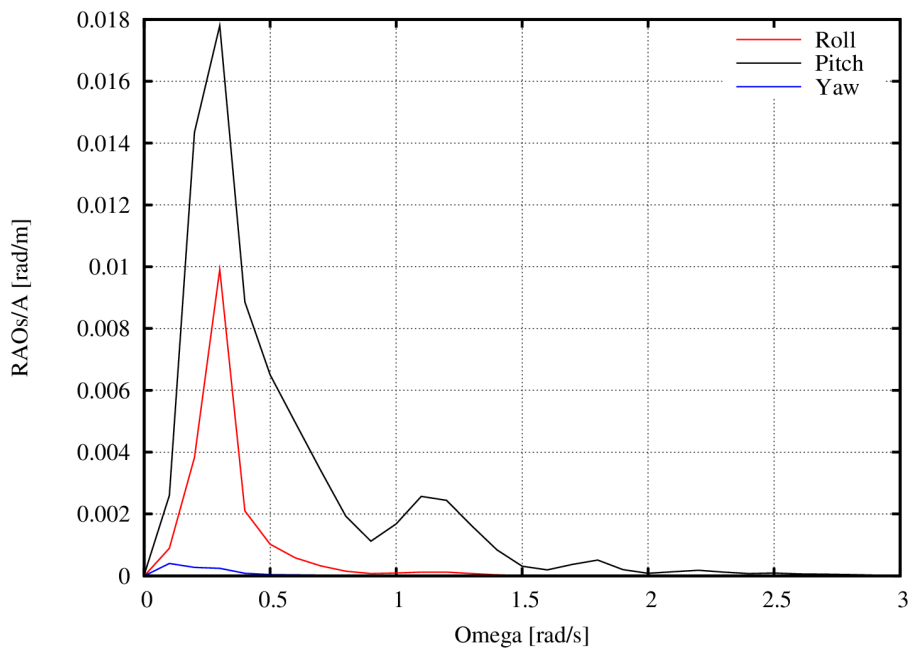
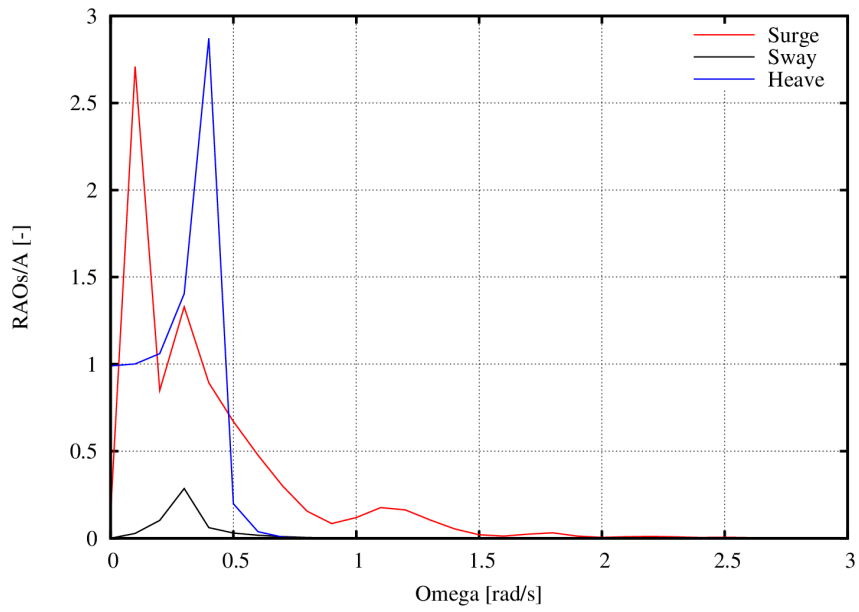


Figure 30: RAOs of the tri-spar floater for 0° wave angle

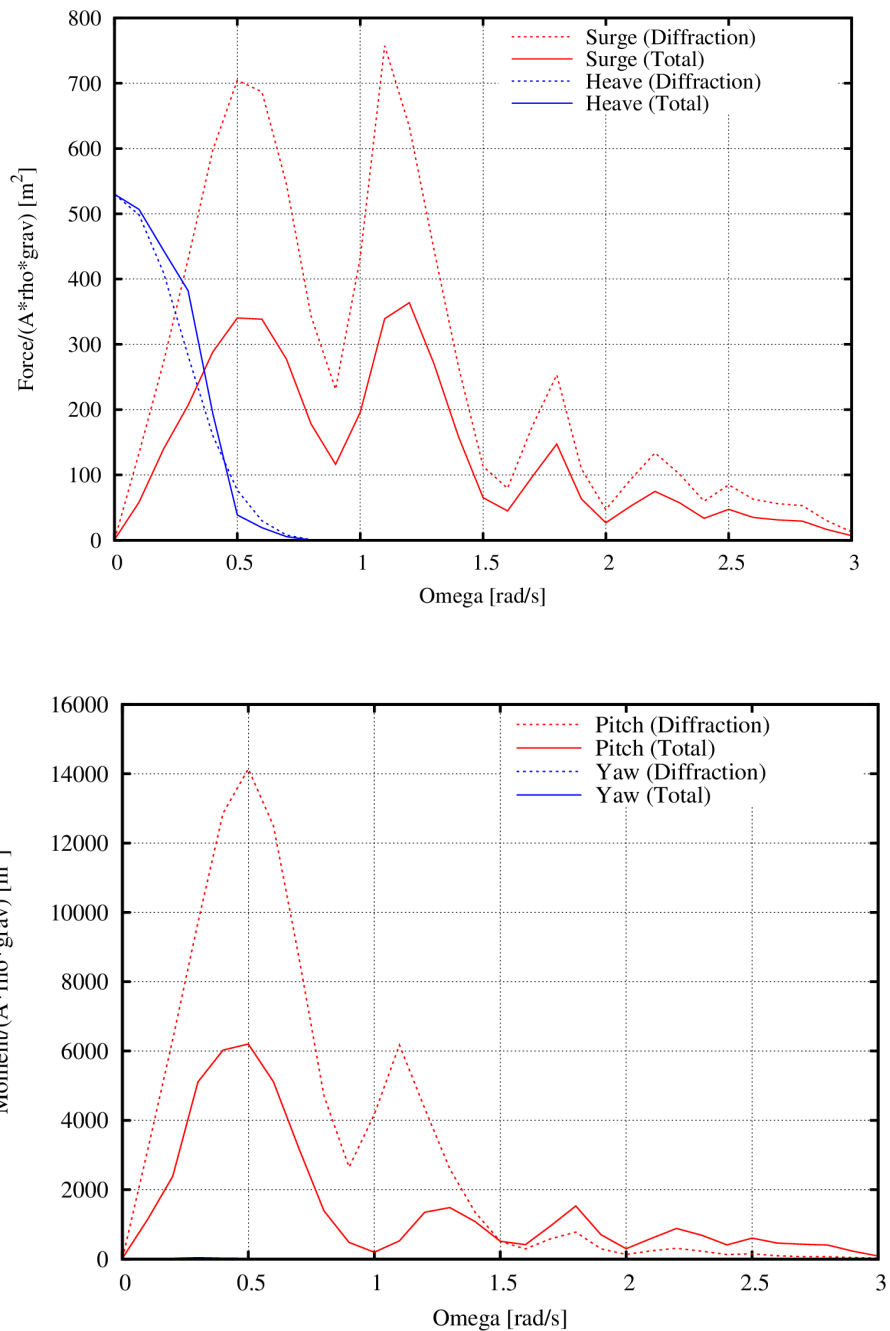


Figure 31: Diffraction and Total hydrodynamic loads of the tri-spar floater with respect to the center of the floater at the mean water level for 0° wave angle

### 7.3.3 Detailed structural design and verification

The floater characteristics defined in (Florian Amann, Frank Lemmer) have been initially introduced in the 3D FEM model. The modifications that took place, during the design procedure are:

1. A slight reduction of the width of the tripod horizontal legs in order to ease the horizontal-vertical leg connection
2. The steel heave plates are replaced by concrete ones
3. The local thickness increase at the central connecting point between the 3 horizontal legs

In the present section, the capacity ratio at selected critical points is presented and the description of each individual part is given. At the end of the section, the updated properties of the floater (comparing to those given initially in section 4) and the equivalent beam properties are given.

### 7.3.4 Capacity ratios of the main parts of the tri-spar floater

In Table 21 the capacity ratios at the most critical positions are given as computed in SAP2000 for the DLC1.6 at 13m/s with  $H_s=10,9\text{m}$  and  $T_p=14.8\text{s}$ . In Figure 33 and Figure 34 stress contours are presented at the connecting point between the vertical and the horizontal legs of the tripod and between the 3 horizontal legs at the center respectively, demonstrating the local stress concentration at these positions.

Critical Position	$\sigma_{vm}/\sigma_y$	$N_{sd}/N_{b,rd}$
Central Cylinder -Horizontal Leg Connection	0.72	-
Horizontal Leg-Vertical Leg Connection	0.284	-
Vertical Leg -Inclined Rods Connection	0.76	-
Inclined Rods	-	0.46
Ties	-	0.08

**Table 21: Capacity Ratios at the critical positions, DLC1.6 at 13m/s,  $H_s=10.9\text{m}$ ,  $T_p=14.8\text{s}$ .**

Where:

- $\sigma_{vm}$  : maximum calculated Von Mises stress of shell elements
- $\sigma_y$  : yield stress of steel
- $N_{sd}$  : Axial force estimated for the inclined rods and ties
- $N_{b,rd}$  : Member's strength against buckling

The inclined rods and the ties are checked against buckling according to EC-3 (EN 1993-1-1: Design of Steel Structures: General rules and rules for buildings, 2004). The highest estimated capacity ratio for the steel ties is  $\sim 0.1$  which is rather low. However, the selection of this thickness is chosen in order to increase the axial stiffness of the structure and in turn reduce the amount of the horizontal force on the concrete wall.

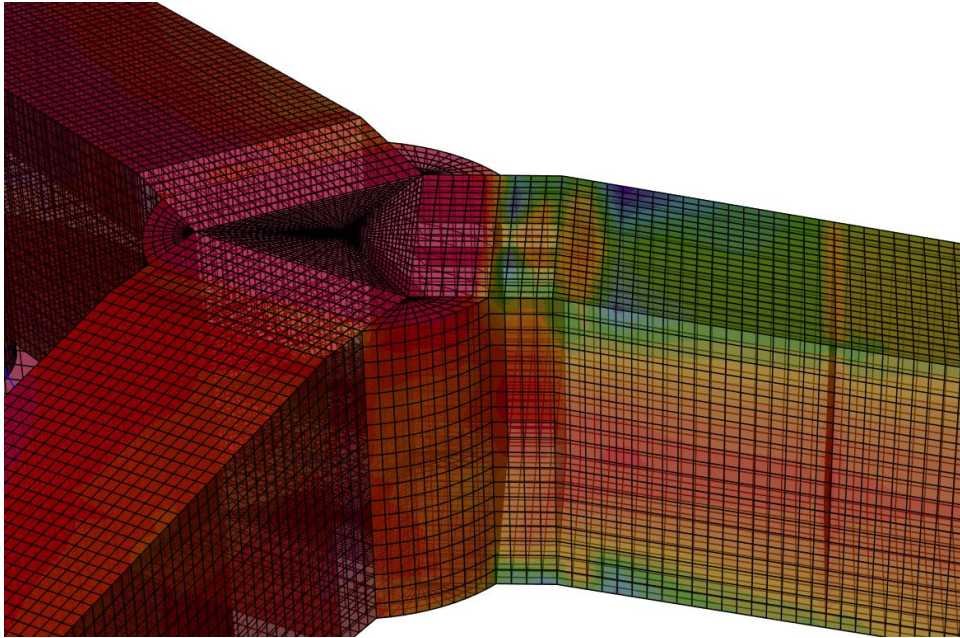


Figure 32: Stress concentration and reinforced areas.

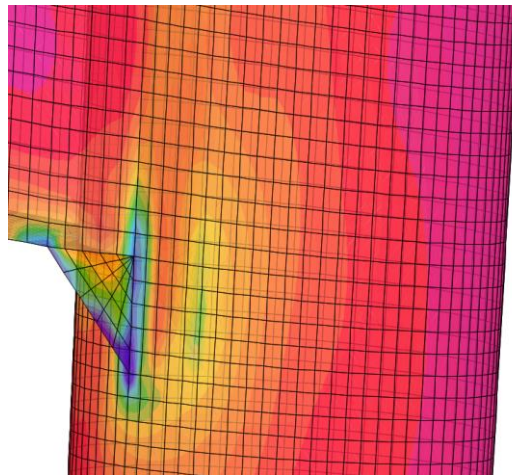


Figure 33: Stress concentration on Horizontal leg - Vertical leg connection.

### 7.3.5 Steel Tripod

The steel tripod is modeled exclusively with shell elements. In total, 48498 thick-shell elements are used. The whole steel tripod is presented in Figure 34, while the connecting points between the horizontal and the vertical steel leg and between the 3 horizontal legs at the center of the floater are presented in Figure 35.

The diameter of the vertical cylindrical legs is equal to 5.64m and their height is 11m, while the wall thickness is for 5.64 cm. In order to avoid local failure at the gamma - connection, steel

brackets of the same thickness have been introduced as shown in Figure 33. Steel plates acting as diaphragms are also introduced inside the peripheral cylinders, in order to reduce the buckling length and in turn to improve the strength against buckling, as shown in Figure 36. For the connection between the abovementioned structural elements and the inclined rods [Figure 37], a pinned connection is used. At the connection points, the local thickness of the material is increased in order to avoid local failures.

The tower base of the wind turbine is attached to the steel central cylinder shown in Figure 35 (right). Initially at this point, local failures predicted for the upper and the rear parts (Figure 32 demonstrates the stress concentration) and thus a reinforced steel zone, composed by steel plates of varying thickness (5.64-17.5 cm) is used, as shown in Figure 38.

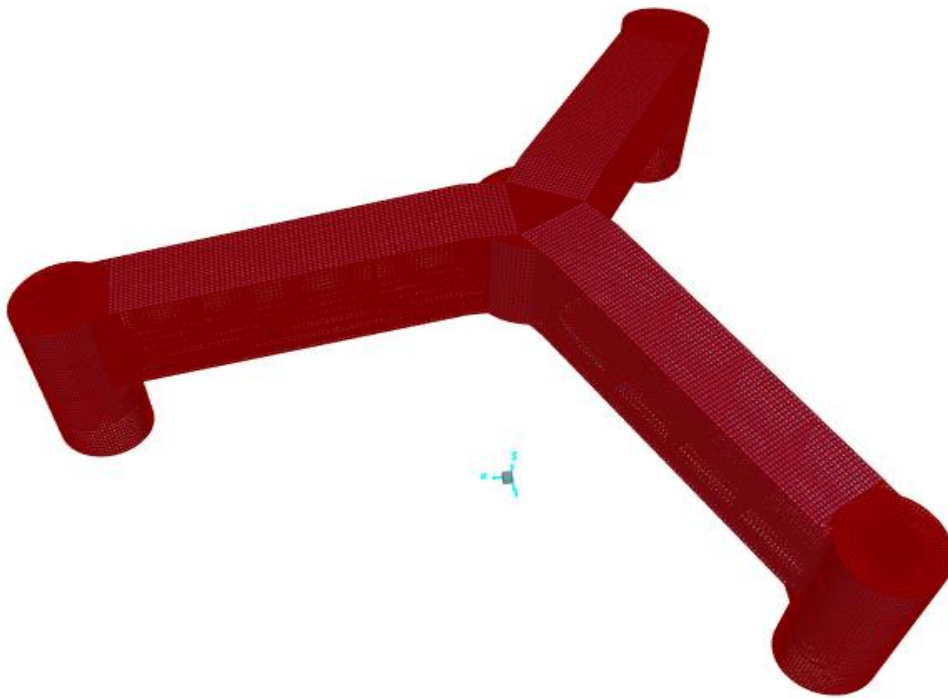


Figure 34: Overview of the FEM mesh of the steel tripod.

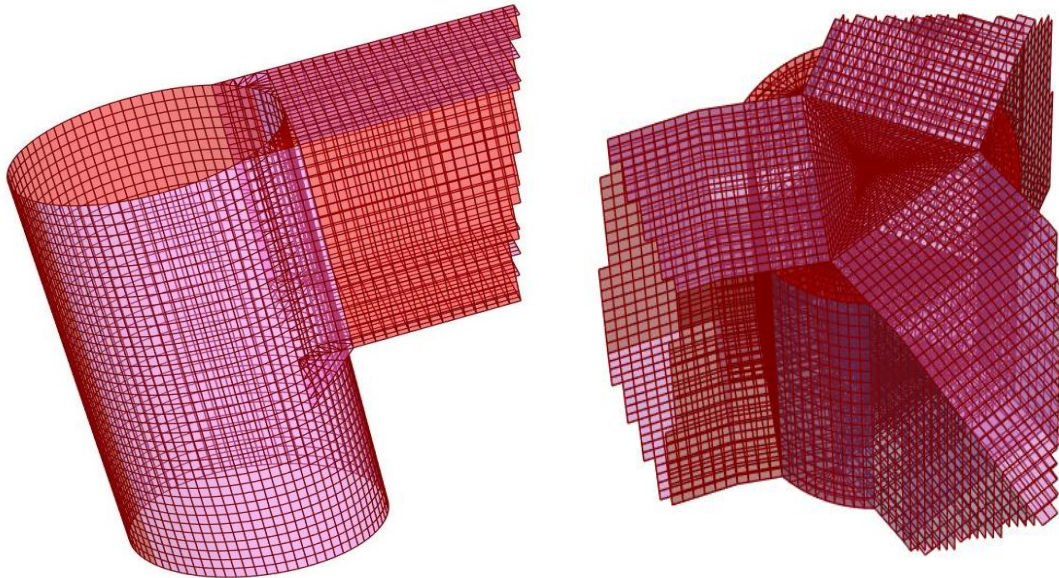


Figure 35: Mesh of the connecting point between the horizontal and the vertical steel leg (left) and of the central connecting point between the 3 horizontal legs (right).

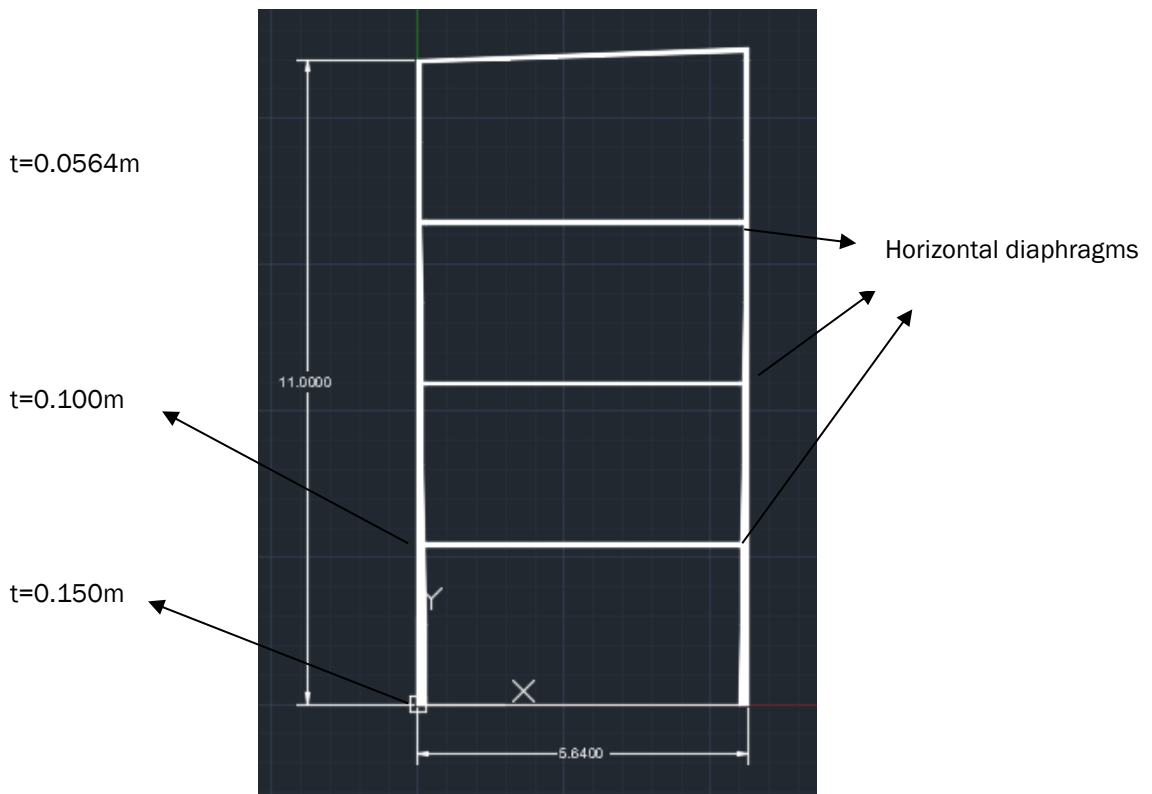


Figure 36: Cross section of the Vertical Leg, demonstrating the Horizontal diaphragms for increasing the straight against buckling.

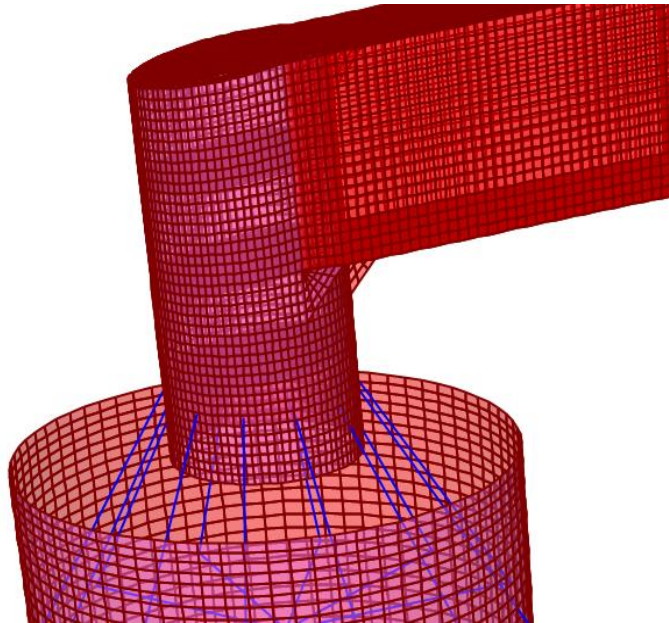


Figure 37: Connection between the Vertical Leg and the Inclined Rods.

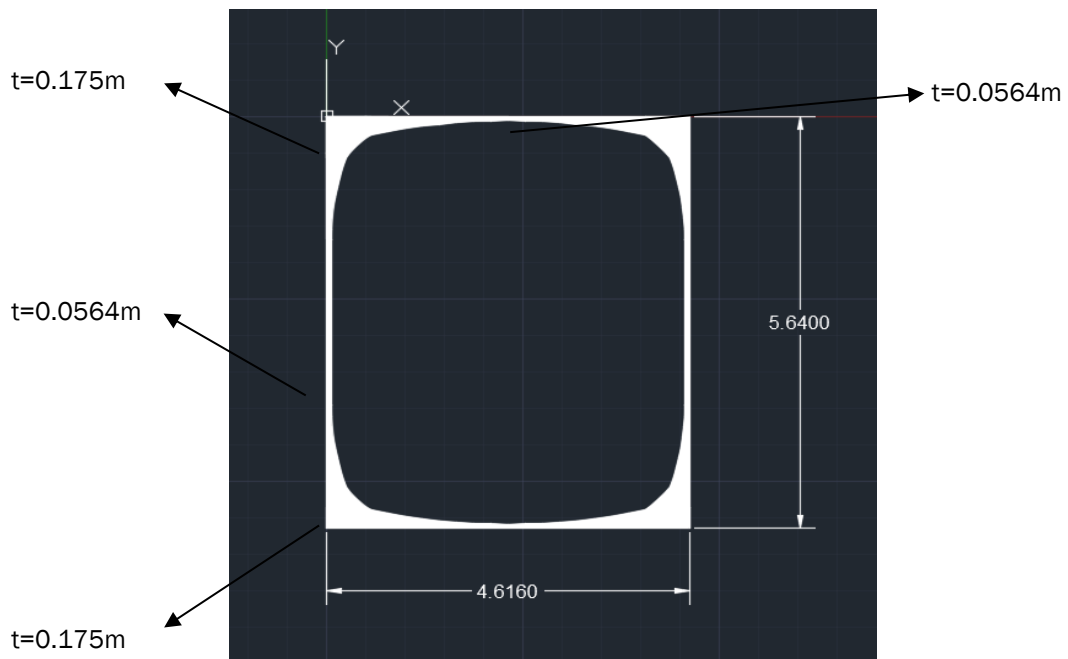


Figure 38: Cross section of the connection between the Central Cylinder and the Horizontal Leg.

### 7.3.6 Steel-concrete connection

The proposed solution, regarding the connection between the steel and the concrete column is formed by:

1. Twelve inclined steel radial rods [Figure 39], with hollow cylindrical cross-sections. Through the 12 rods the loading is transferred to 12 positions along the concrete wall. The inclination angle is  $60^\circ$  in order to minimize the horizontal force transferred to the wall, since the axial force of each member is reduced. The rods are considered hinged at both ends [Figure 40], reducing the lateral buckling phenomena.
2. Twelve horizontal steel ties with hollow cylindrical sections pinned to the concrete shell [Figure 39]. These ties will prevent the bulging failure of the concrete wall, caused by the communicated force through the inclined members.
3. A steel ring on which the ties are connected is shown in Figure 39.

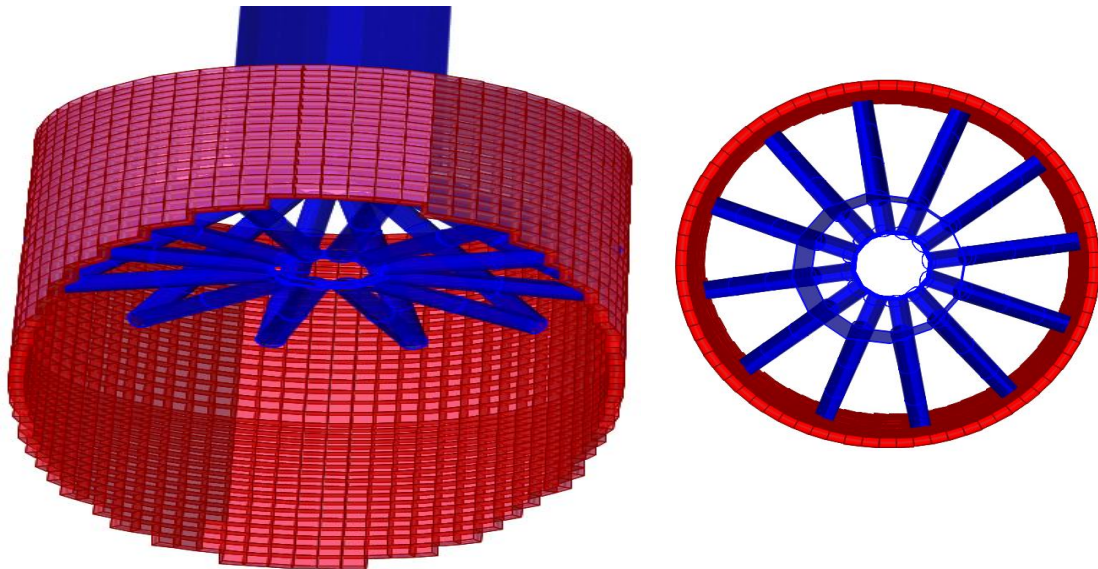


Figure 39: Connection between steel and concrete cylinders, 3D view (left) and top view (right).

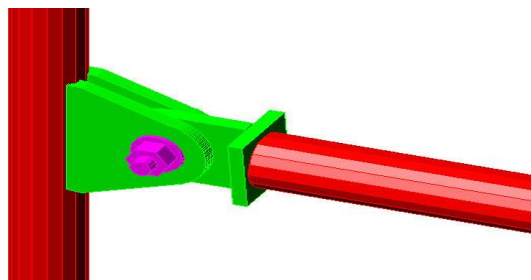


Figure 40: Typical pinned connection.

### 7.3.6.1 Design of the steel inclined rods

The steel rods are made of a hollow cylindrical section with the following properties [Figure 41, Figure 42].

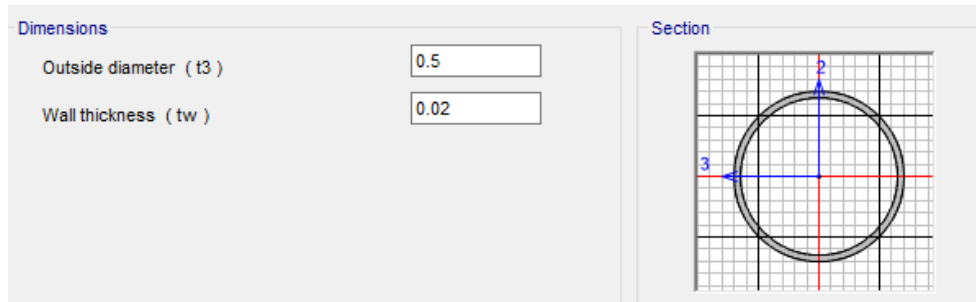


Figure 41: Geometry of the inclined steel rods [m].

Properties			
Cross-section (axial) area	0.0302	Section modulus about 3 axis	3.480E-03
Moment of Inertia about 3 axis	8.701E-04	Section modulus about 2 axis	3.480E-03
Moment of Inertia about 2 axis	8.701E-04	Plastic modulus about 3 axis	4.611E-03
Product of Inertia about 2-3	0.	Plastic modulus about 2 axis	4.611E-03
Shear area in 2 direction	0.0151	Radius of Gyration about 3 axis	0.1699
Shear area in 3 direction	0.0151	Radius of Gyration about 2 axis	0.1699
Torsional constant	1.740E-03	Shear Center Eccentricity (x3)	0.

Figure 42: Properties of the inclined steel rods [kN, m].

### 7.3.6.2 Design of the steel ties

The steel ties are made of a steel hollow cylindrical section with the following properties [Figure 43, Figure 44].

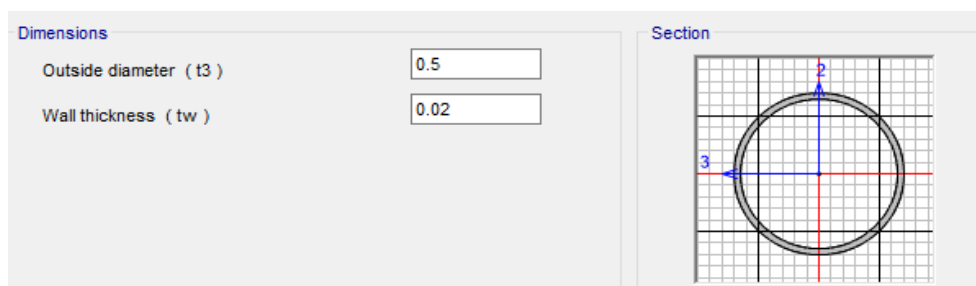


Figure 43: Geometry of the steel ties [m].

Properties			
Cross-section (axial) area	0.0302	Section modulus about 3 axis	3.480E-03
Moment of Inertia about 3 axis	8.701E-04	Section modulus about 2 axis	3.480E-03
Moment of Inertia about 2 axis	8.701E-04	Plastic modulus about 3 axis	4.611E-03
Product of Inertia about 2-3	0.	Plastic modulus about 2 axis	4.611E-03
Shear area in 2 direction	0.0151	Radius of Gyration about 3 axis	0.1699
Shear area in 3 direction	0.0151	Radius of Gyration about 2 axis	0.1699
Torsional constant	1.740E-03	Shear Center Eccentricity (x3)	0.

Figure 44: Properties of the ties [kN, m].

### 7.3.7 Reinforcement of the Concrete cylindrical columns

The steel reinforcement of the concrete cylindrical columns is defined according to EC2 (EN 1992-1-1 Design of concrete structures. General rules for buildings, 2004):

1. Vertical reinforcement:  $\Phi 20/140$
2. Horizontal reinforcement:  $\Phi 20/300$
3. Confinement Hoops:  $\Phi 10/200$

### 7.3.8 Heave Plates

The originally considered steel heave plates are replaced by concrete ones [Figure 45], in order to avoid the steel to concrete connection between the heave plates and the floater base. The geometry of the heave plates is unchanged, so the height is 0.5m and the diameter is 22.5m. The total mass of each plate is  $M_{hp} = 546$  tn.

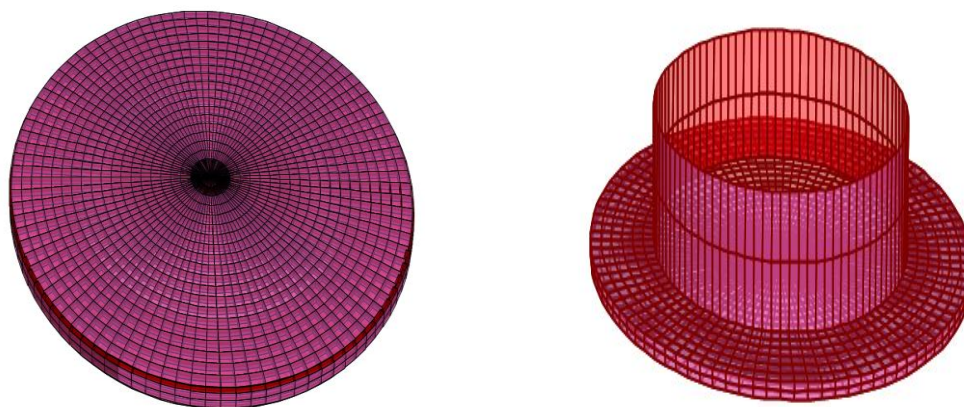


Figure 45 : Meshing of the heave plate (left) and of the connection between a cylindrical column and a heave plate (right).

### 7.3.9 Platform data

Table 22 details the updated total properties of the tri-spar floater, derived by the detailed design analysis.

		Initial design	Current design
<b>Platform</b>	Elevation of tower base above SWL (m)	25	25
	Center of mass below SWL (m)	36.0176	<b>35.9702</b>
	Platform mass (tn)	28268.22	28268.18
	Ballast Mass (tn)	17264	<b>15653.12</b>
<b>Columns</b>	Length (m)	65	65
	Distance to the centre (m)	26	26
	Diameter (m)	15	15
	Elevation above SWL (m)	10.5	10.5
	Mass (tn)	3279.5	3279.5
<b>Heave</b>	Thickness (m)	0.5	0.5
	Diameter (m)	22.5	22.5
<b>Plates</b>	Mass (tn)	678.7	<b>1639.3</b>
<b>Tripod</b>	Total Height (m)	15	15
	Height Outer Cylinder (m)	11	11
	Diameter Outer Cylinder (m)	5.64	5.64
	Bar Cross-Section height (m)	5.64	5.64
	Bar Cross-Section width (m)	5.64	<b>4.6164</b>
	Wall thickness (m)	0.0564	0.0564
	Mass (tn)	971.3	<b>948.36</b>
<b>Tripod-Cylinder</b>	Inclined rod diameter (m)	-	<b>0.5</b>
	Inclined rod thickness (m)	-	<b>0.02</b>
<b>Connection</b>	Horizontal tie diameter (m)	-	<b>0.5</b>
	Horizontal tie thickness (m)	-	<b>0.02</b>
	Total Mass (tn)	-	<b>217.5</b>
<b>Densities</b>	Concrete density (kg/m <sup>3</sup> )	2750	2750
	Steel density (kg/ m <sup>3</sup> )	7750	7750
	Ballast density (kg/ m <sup>3</sup> )	2500	2500
	Water density (kg/ m <sup>3</sup> )	1025	1025
<b>Mass</b>	Total Platform Mass (tn)	28268.22	28268.18
	Initial Total Platform Mass (tn)	28268.22	28268.22
<b>Moments of inertia about centre of mass</b>	Ixx (tn m <sup>2</sup> )	1.8674 E+07	<b>1.7451 E+07</b>
	Iyy (tn m <sup>2</sup> )	1.8674 E+07	<b>1.7451 E+07</b>
	Izz (tn m <sup>2</sup> )	2.0235 E+07	<b>2.0145 E+07</b>

**Table 22: Updated platform properties, derived by the detailed design analysis.**

### 7.3.10 Equivalent beam properties

In Table 16 the equivalent beam properties of all the cross sections are given in order to be used in hydro-servo-aero-elastic tools that consider the flexibility of the floater using beam theory. The axes orientation of the horizontal steel leg cross section is shown in Figure 46, while all the other sections are cylindrical.

Property	Concrete Columns	Heave Plates	Vertical Steel Cylinder	Horizontal Steel Beam
$\rho$ (kg/m <sup>3</sup> )	2750	2750	7750	7750
E (N/m <sup>2</sup> )	3.70E+10	3.70E+10	2.1E+11	2.1E+11
G (N/m <sup>2</sup> )	1.54E+10	1.54E+10	8.08E+10	8.08E+10
J (m <sup>4</sup> )	978.4402	25161.12	7.8787	7.1938
A (m <sup>2</sup> )	18.3376	397.6078	0.9964	1.1446
$k_x A$ (m <sup>2</sup> )	9.1688	357.847	0.4982	0.6407
$k_y A$ (m <sup>2</sup> )	9.1688	357.847	0.4982	0.5166
$I_{xx}$ (m <sup>4</sup> )	489.2201	12580.56	3.9394	5.7066
$I_{yy}$ (m <sup>4</sup> )	489.2201	12580.56	3.9394	4.1158
dens (kg/m)	50428.4	1093421.45	7722.1	8870.65
$\rho I_{xx}$ (kgm)	1345355.275	34596540	30530.35	44226.15
$\rho I_{yy}$ (kgm)	1345355.275	34596540	30530.35	31897.45
EA (N)	6.78491E+11	1.47115E+13	2.09244E+11	2.40366E+11
EI <sub>xx</sub> (Nm <sup>2</sup> )	1.81011E+13	4.65481E+14	8.27274E+11	1.19839E+12
EI <sub>yy</sub> (Nm <sup>2</sup> )	1.81011E+13	4.65481E+14	8.27274E+11	8.64318E+11
$G_x A$ (N)	1.41352E+11	5.51681E+12	4.02392E+10	5.17488E+10
$G_y A$ (N)	1.41352E+11	5.51681E+12	4.02392E+10	4.17254E+10
GJ (Nm <sup>2</sup> )	1.50843E+13	3.87901E+14	6.36357E+11	5.81038E+11

Table 23: Equivalent beam properties.

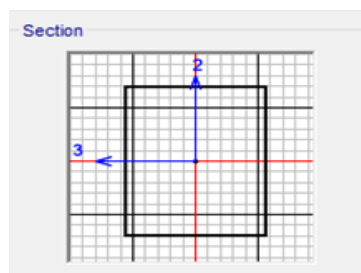


Figure 46: Cross section axes definition of the horizontal steel leg, where  $GA_2 \equiv GA_x$  and  $GA_3 \equiv GA_y$

## 7.4 FLS analysis of the tri-spar floater

In the present section, the procedure for the structural design/verification of the tri-spar floater against fatigue is presented. This requires a stochastic analysis, performed by considering the model presented in section 7.3 in the frequency domain using SAP2000 solver. For the stochastic analysis the excitation is given in terms of power spectral density (PSD) of the loads/pressures (instead of the maximum ones given for the ULS), while the solution provides the root mean square (RMS) stresses and the stress PSD at every element. For the estimation of the structure lifetime, the stress PSD at the critical points is used in conjunction with the appropriate material S-N curves, given in (DNV-RP-C203 Fatigue Design Of Offshore Steel Structures. (2011) ).

The external loading includes:

- The constant gravitational and hydrostatic terms,
- The PSD of the loads at the tower base (to be applied on the upper part of the floater). These PSD's were obtained by processing time domain hydro-servo-aero-elastic simulations for DLC1.2 [section 7.2.1] and
- The PSD of the hydrodynamic pressure applied along the wet surface of the floater, obtained from the solution of the hydrodynamic problem in the frequency domain [section 7.3.2].

### 7.4.1 Theory

The fatigue lifetime may be calculated based on the S-N fatigue approach under the assumption of linear cumulative damage (Palmgren-Miner rule). When the long-term stress range distribution is expressed by a stress histogram, consisting of a convenient number of constant stress range blocks  $\Delta\sigma_i$  each with a number of stress repetitions  $n_i$  the fatigue criterion yields:

$$D = \sum_{i=1}^k \frac{n_i}{N_i} = \frac{1}{\bar{a}} \sum_{i=1}^k n_i (\Delta\sigma_i)^m \leq \eta \quad (1)$$

Where:

$D$  = accumulated fatigue damage

$\bar{a}$  = intercept of the design S-N curve with the log N axis

$m$  = negative inverse slope of the S-N curve

$k$  = number of stress blocks

$n_i$  = number of stress cycles in stress block  $i$

$N_i$  = number of cycles to failure at constant stress range  $\Delta\sigma_i$

$\eta$  = usage factor = 1/Design Fatigue Factor (DFF) defined in (DNV-OS-C101 Design of Offshore Steel Structures, General (LRFD Method). (2011)).

For the present analysis, the design S-N curves (in air) given in DNV-RP-C203 are used [Figure 47]. For offshore structures subjected to typical wave and wind loading the main contribution to fatigue damage is in the region  $N > 10^6$  cycles and the bilinear S-N curves can be used. The necessary parameters ( $\bar{a}$ ,  $m$ ) are extracted from the S-N curves and provided in Table 24

The stress Range ( $\Delta\sigma_i$ ) and number of cycles ( $n_i$ ) are derived from the stress PSD provided by the SAP2000. (the  $i$ -th stress range can be calculated as the square root of the  $i$ -area under the stress PSD curve, while the number of stress cycles for 20 years in block  $i$  is  $n_i = 60 \cdot 60 \cdot 24 \cdot 365 \cdot 20 \cdot f_i$  [Hz]).

The Design fatigue factors (DFF) are applied in order to reduce the probability of fatigue failures. The DFFs depend on the significance of the structural components with respect to structural integrity and on the availability for inspection and repair. For the present analysis the DFF=2 is used for all the components. Table 25 provides the DFFs as defined in DNV-OS-C101.

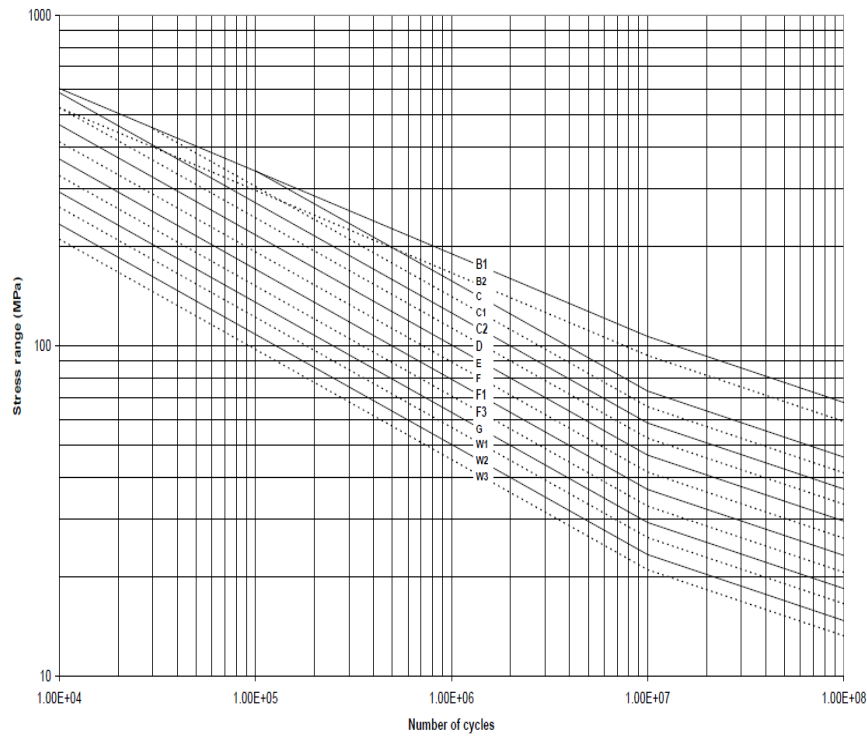


Figure 47: S-N curve in air from DNV-RP-C203.

Table 24: Parameters derived directly from the S-N curves in air, defined in DNV-RP-C203.

S-N curve	$N \leq 10^7$ cycles		$N > 10^7$ cycles	Fatigue limit at $10^7$ cycles *)	Thickness exponent $k$
	$m_1$	$\log \bar{a}_1$	$\log \bar{a}_2$ $m_2 = 5.0$		
B1	4.0	15.117	17.146	106.97	0
B2	4.0	14.885	16.856	93.59	0
C	3.0	12.592	16.320	73.10	0.15
C1	3.0	12.449	16.081	65.50	0.15
C2	3.0	12.301	15.835	58.48	0.15
D	3.0	12.164	15.606	52.63	0.20
E	3.0	12.010	15.350	46.78	0.20
F	3.0	11.855	15.091	41.52	0.25
F1	3.0	11.699	14.832	36.84	0.25
F3	3.0	11.546	14.576	32.75	0.25
G	3.0	11.398	14.330	29.24	0.25
W1	3.0	11.261	14.101	26.32	0.25
W2	3.0	11.107	13.845	23.39	0.25
W3	3.0	10.970	13.617	21.05	0.25
T	3.0	12.164	15.606	52.63	0.25 for SCF $\leq$ 10.0 0.30 for SCF $>$ 10.0

Table 25: Design Fatigue Factors from DNV-OS-C101.

<i>DFE</i>	<i>Structural element</i>
1	Internal structure, accessible and not welded directly to the submerged part.
1	External structure, accessible for regular inspection and repair in dry and clean conditions.
2	Internal structure, accessible and welded directly to the submerged part.
2	External structure not accessible for inspection and repair in dry and clean conditions.
3	Non-accessible areas, areas not planned to be accessible for inspection and repair during operation.

#### 7.4.2 Results: Critical sections and Damage ratios

The critical sections for the structural design against fatigue are the connecting points between the different members. Welds connections are considered for the steel members and bolt connections for the steel to concrete connections. Five different connecting points are checked as shown in Figure 48, Figure 49:

- Connection between the Central cylinder and the Horizontal legs
- Connection between the Horizontal Legs at the inclination point (near to center)
- Connection between the Horizontal and the Vertical Legs
- Connection between the Inclined Rods and Steel Vertical Leg
- Connection between the Inclined Rods and the Concrete Wall

In Figure 48 the 3 critical connecting points of the steel tripod (left) and the corresponding weld type as given in DNV-RP-C203 are defined. For the first and the third connecting points, automatic welds can be carried out on both sides and so the recommended S-N curve is C, while for the second connecting point transverse butt welds is considered, welded from both sides and so the S-N curve D is used.

In Figure 49 the connecting point between the inclined rods and the steel Leg or the concrete wall (left) and the diagram of the support for the pinned connection (right) are presented. The steel support is welded on the vertical steel leg and automatic weld can be carried out from both sides. If a specialist inspection demonstrates that longitudinal welds are free from significant flaws, the S-N curve category B2 can be used. On the other side, the support is attached to the concrete cylinder with bolts. Each bolt is subjected to shear stresses. The  $m$  and  $\log(a)$  coefficients are given in Table 26 together with the results obtained from the fatigue analysis.

The most critical part of the structure is the connection between the inclined rods and steel vertical leg where the damage ratio is  $\sim 0.7$ . On the other critical points the damage ratio is rather low (less than 0.1). It is noted that the damage ratio should be less than 1 since the DFF has been moved to the LHS of the equation.

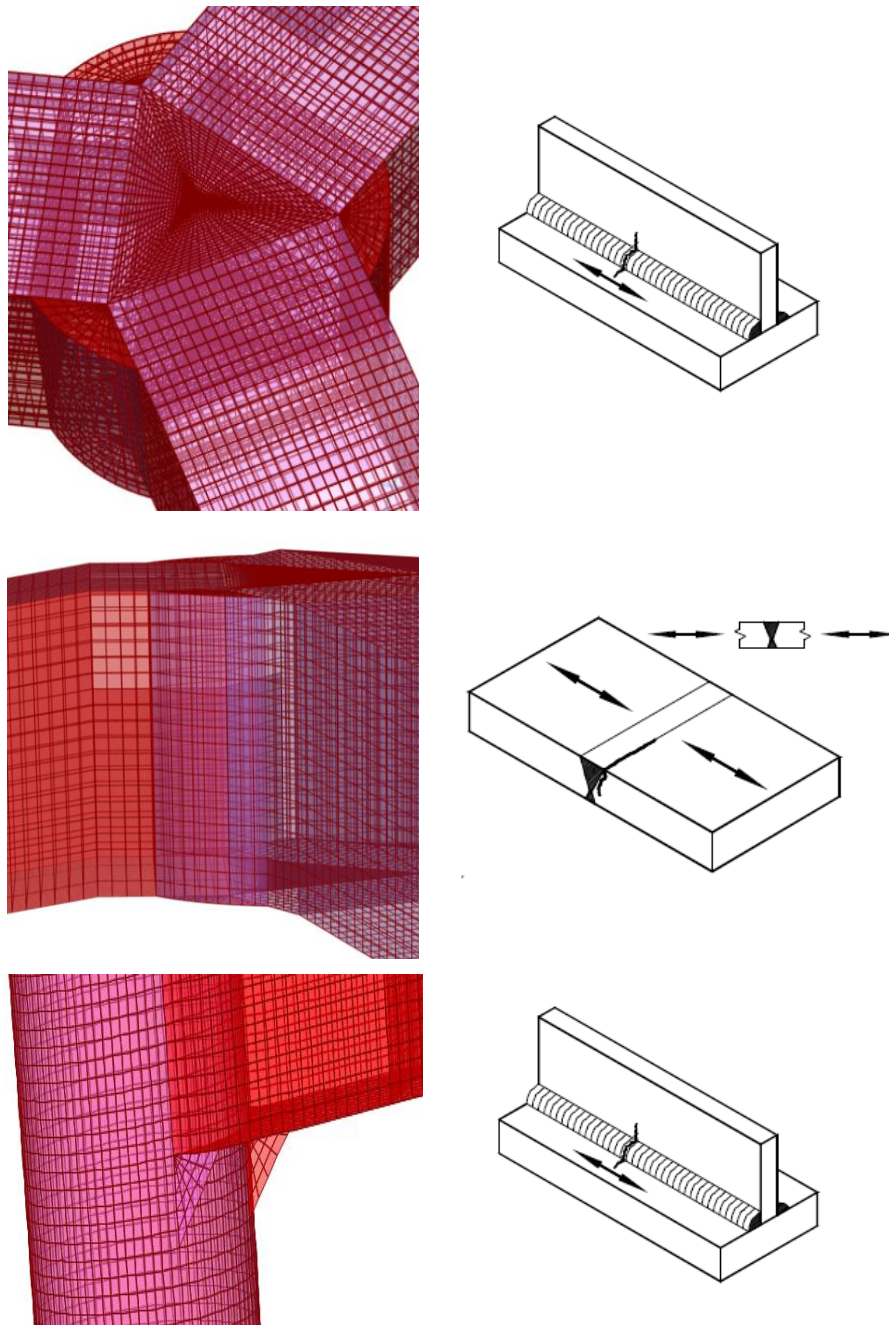


Figure 48: The 3 critical connecting points of the steel tripod, checked against fatigue (left) and their weld type based on DNV-RP-C203 (right).

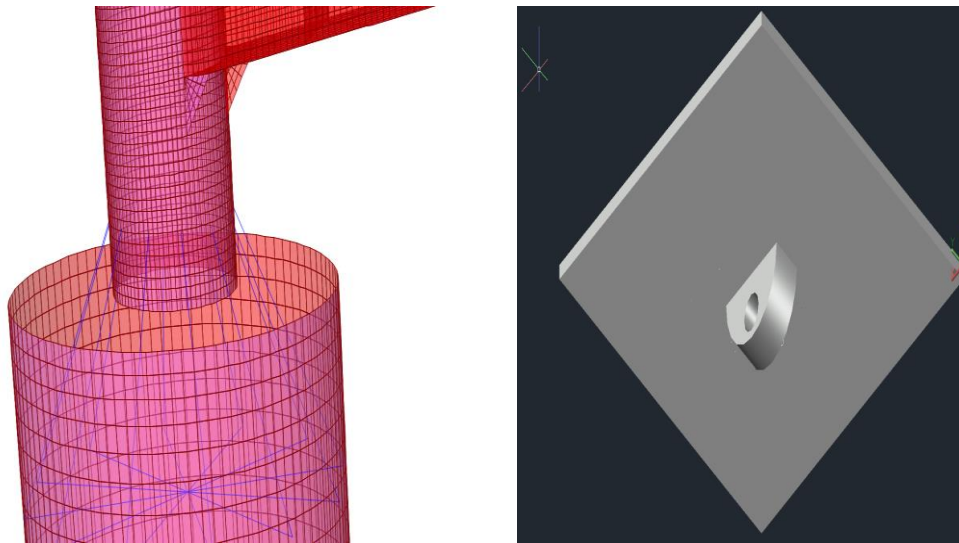


Figure 49: Connecting point between the inclined rods and the steel Leg or the concrete wall (left) and description of the support for the pinned connection (right).

Table 26: 20 years Damage Ratio from the fatigue analysis (should be <1).

Connection	S-N Curve Parameters			DFF	Damage Ratio
	Type	log(a)	m		
1. Central Cylinder – Horizontal Leg	C	12.592	3	2	0.032
2. Horizontal Leg at inclination point	D	12.164	3	2	0.120
3. Horizontal Leg – Vertical Leg	C	12.592	3	2	0.074
4. Inclined Rods – Steel Vertical Leg	B2	15.000	4	2	<b>0.706</b>
5. Inclined Rods - Concrete Wall	-	16.301	5	2	0.003

## 8 THE FLOATING VERTICAL AXIS WIND TURBINE CASE

### 8.1 Introduction

In this section, the case of a floating 10MW Vertical Axis Wind Turbine is considered and preliminary design and load analysis is reported. This work has been carried out in order to facilitate a first comparison of the two basic concepts and by that check the positive perspectives VAWTs may have as floating systems.

To this end it was decided to rely on the 5MW DeepWind concept (Figure 50) which for the purposes of the INNWIND.EU project should be upscaled to 10MW. Next first the design description is given and the upscaling procedure is outlined and then energy production and cost estimates are provided.



Figure 50 : SolidWorks rendering of the DeepWind concept

### 8.2 Design description and upscaling

The DeepWind 5MW concept combines a Darrius type 2 bladed rotor with a spar buoy floater in which the generator is accommodated (Figure 51). The concept consists of the following components:

Super structure	Includes the rotor and the tower clearance
Rotor:	Consists of 2 blades and a central, tapered column connecting blade rods with column
Tower shaft	A section connecting the rotor with the floater, called clearance
Floater	A spar buoy establishing the capacity for carrying the superstructure

Generator module	The part consists of a rotor connected to the floater, and a stator, connected to the torque absorber with torque arms connected to the mooring. The generator is enclosed in a casing
Mooring system	Catenary chain connecting the casing structure to the sea bed

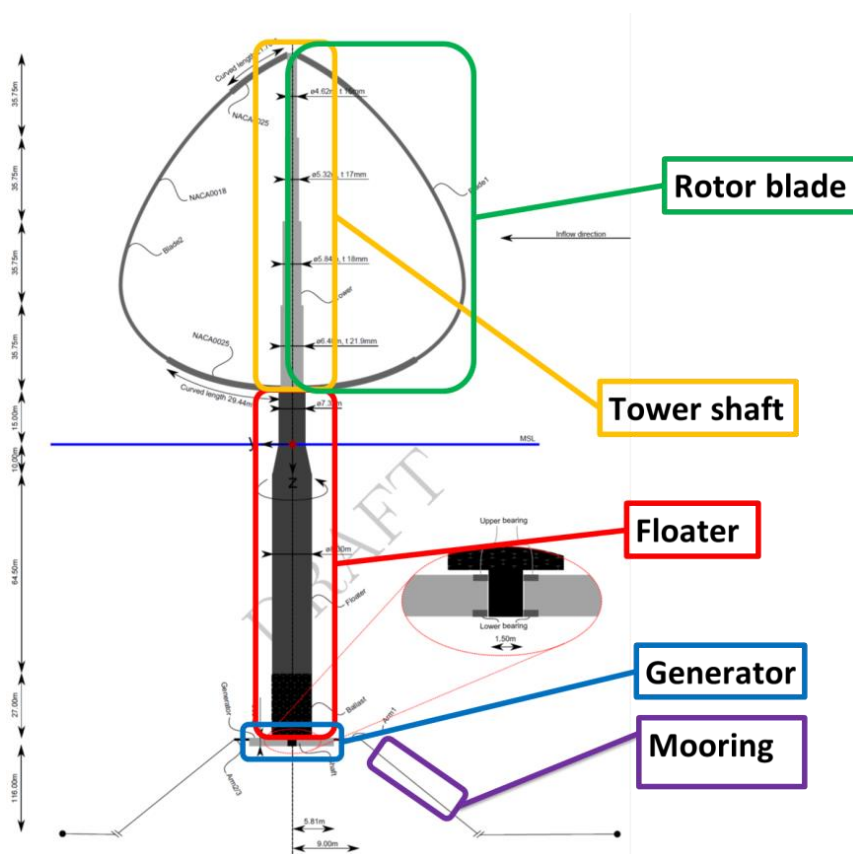


Figure 51 : The DeepWind Floating VAWT concept

In order to obtain the 10MW version, at first direct upscaling was carried out. Above sea level, upscaling consists of charging the dimensions with the scale factor defined from the power ratio assuming identical power performance and modifying structural properties so that normalized eigenmodes with respect to rotor speed remain the same. Below sea level (floater and moorings), Froude scaling is applied. This will result in scaling the different properties of the 5 MW design with a scaling factor. A difference adopted in this upscale might be that below water surface, Froude scaling is applied. This was believed to be a sound scheme, but provides a dilemma when considering the extension of the floater towards the blades position.

In parallel to the above upscaling process, a spreadsheet calculation tool was used, in order to find optimal solutions of a given design and to verify that a stable solution of an optimal floater exists for this configuration and at a thrust level of 3.7MN appearing at 26m/s wind speed. This exercise, reprinted in Table 28- resulted in a floater length of 152m with a ballast requirement of 40.45 m. However, the HAWC2 simulations following up on this design, did not show this configuration to be stable at high wind speeds. Time did not allow to go deeper and better understand the origin of the instabilities – which probably are due to the non-linear character of

the problem. During an onshore study of the 5MW VAWT, the tower diameter along height was increased by 20% to withstand fatigue, as pointed out in the study of (Christos Galinos (2): Vertical axis wind turbine design load cases investigation and comparison with horizontal axis wind turbine Paper presented at 13th Deepwind conference in Trondheim Norway, 2016), which after upscaling made the transition between the slender part of the floater and the tower look truncated. An additional attempt was made to actually upscale the generator section from the original concept (Krisztina Leban: Design Sheet Nessie Design WP3 Deep Wind FIXED, extract from PhD thesis , 2014); however, the adaptation into a HAWC2 model resulted in complicated deviations from the physical model [ (David Verelst et al: Detailed Load Analysis of the baseline 5MW DeepWind Concept , DTU Wind Energy E-0057, 2014), (Rachel Meyer: Stability Analysis of Multi-Megawatt Darrieus- Type Floating Vertical Axis Wind Turbines DTU Wind Energy-M-0099 2016), (Christos Galinos (1): Study of Design Load Cases for Multi-Megawatt Onshore Vertical Axis Wind Turbines)] and due to time limitations modifications along this line work were postponed until further.

In order to remedy the challenge with the floater draft of 152 m withstanding the thrust requirements at 26 m/s trial and error attempts were made by elongating the main hull of the floater and adjusting the ballast and mooring weights for balancing the thrust. Two local solutions were found, at 203m and 184m respectively of which the shortest was selected for further studies. The main dimensions of the floater are given in Table 27.

**Table 27: Dimensions of the 10MW VAWT Floater**

	Length [m]	Diameter [m]	Mass [tn]	Displacement [m <sup>3</sup> ]
Section 1	18.3	9.3896		
Section 2	12.2			871
Section 3	153.5	10.126		12362
L	184		11509.7	13233
Ballast	42.77		9501.4	
Generator	3.18	14.2	526.7	
Bearing	1.22		18.16	

The torque arms (#3) have a length of 18.3m and mass 155190kg, in total. They are mounted at the start of the generator section.

Table 28: Optimization process for the 10MW FVAWT

VAWT sheet			Designation		5MW	10MW		
Transmission, generator and gearbox			Nom power	kW	5000	10000		
			Generator mass	ton	50.00	141.42		
			bearing mass	ton	120.00	339.41		
			Other(enclosure) mass	ton	403.09	677.91		
<b>VAWT Rotor</b>								
			Swept area	m <sup>2</sup>	11996	23992		
			Specific power	W/m <sup>2</sup>	417	417		
		HAWT eqv	R (radius)	m	62	87		
		HAWT eqv	D (diameter)	m	124	175		
			H/D:		1.18	1.14		
		VAWT	D (rotor dia)	m	121	171		
		VAWT	H (rotor h)	m	143	195		
<b>Blades</b>	-1		S (laengde)	m	224	271		
			S/R		3.62	3.10		
			N		2	2		
			Solidity	$\sigma=NC/R$	0.1653	0.1653		
			C (korde)	m	5.00	7.07		
			t/C		0.198	0.198		
			t (tyk)		0.99	1.40		
			BI Cross/t°C		0.0232	0.0330		
			BI Cross	m <sup>2</sup> /blade	0.1159	0.3266		
			BI Volume CrossxLength/blade	m <sup>3</sup>	25.95	88.43		
			BI density	kg/m <sup>3</sup>	1850	1800		
			BI mass	ton/blade	48.00	159.17		
			Mass Rotor	Ton	96	318		
				CM rotorblade	m	-76.76	-112.50	
		<b>tower</b>	0		1 Tube Dia D <sub>top</sub>	m	5.58	7.903
	2 Tube thick t <sub>ce</sub>			m	0.02400	0.034		
	Area			m <sup>2</sup>	0.420	0.839		
	Tube material volume			m <sup>3</sup>	60	164		
	Buoyant force			kN	0.00	0.00		
	Tube mass			ton	467	1273		
	Mass blade+tower connecting blades			ton	563	1592		
	CM tuberot			m	-77.33	-109.36		
	CM combined_SWL			m	-77.23	-109.99		
	Tube length h <sub>0</sub>			m	15.00	15.00		
	Length tower top- sealevel			m	158.00	210.04		
	Tube Dia D <sub>top</sub>			m	5.588	7.903		
	Tube thick t <sub>ce</sub>			m	0.0240	0.034		
	Area			m <sup>2</sup>	0.420	0.839		
	Tube material volume(h <sub>0</sub> )			m <sup>3</sup>	6.29	12.59		
	Tube volume(h <sub>0</sub> +H)	m <sup>3</sup>	66.28	176.24				
	Above SWL volume(tubes,blades)	m <sup>3</sup>	118.2	353.1				
	CB	m						
	Buoyant force	kN	0.00	0.00				
	Tube mass h <sub>0</sub>	ton	48.96	97.92				
	Mass above ASWL	ton	611.70	1689.46				
		CM tube	m	-7.50	-7.50			
		CM rotorblade+tower+h <sub>0</sub>	m	-71.65	-104.05			
<b>Floater</b>	0.01587	1		Tube Dia D <sub>1</sub>	m	7.26	10.27	
				Tube thick t <sub>1</sub>	mm	0.0534	0.075	
				Tube length H <sub>1</sub>	m	5.00	7.070	
			Tube material volume Vol 1	m <sup>3</sup>	6.94	17.08		
			Tube volume	m <sup>3</sup>	206.88	585.16		
			Buoyant Force 1	kN	2080.27	5883.89		
			COM b SWL	m	2.50	3.54		
			Tube mass 1	ton	47.40	134.06		
			2 frustrum		Tube Dia D <sub>2</sub>	m	7.98	11.12
				Tube thick t <sub>2</sub>	m	0.05	0.075	
				Tube length H <sub>2</sub>	m	10.00	14.14	
			Tube material volum Vol 2	m <sup>3</sup>	13.03	36.86		
			Tube volume	m <sup>3</sup>	486.42	1375.81		
			Buoyant Force 2	kN	4891.09	13834.09		
			COM b SWL	m	6.18	8.75		
	Tube mass 2	ton	102.31	289.37				
	0.6402	3		Tube Dia D <sub>3</sub>	m	8.47	11.98	
			Tube thick t <sub>3</sub>	m	0.05	0.075		
			Tube length H <sub>3</sub>	m	57.20	80.89		
	Tube material volum Vol 3	m <sup>3</sup>	80.04	226.40				
	Tube volume	m <sup>3</sup>	3222	9113				
	Buoyant Force 3	kN	32397	91632				
	COM b SWL	m	43.59	61.65				
	Tube mass 3	ton	628.34	1777.22				
	5182	Ballast 4		Tube Dia D <sub>4</sub>	m	8.47	11.98	
			Tube thick t <sub>4</sub>	m	0.05	0.075		
			Tube length H <sub>4</sub>	m	28.60	40.45		
	Tube volum Vol 4	m <sup>3</sup>	1570.92	4443.23				
	Buoyant Force 4	kN	0.00	0.00				
	COM b SWL	m	57.89	81.88				
	Tube mass4	ton	4084	11552				
	5MW 5622	20MW 22,564		Diameter	m	7.40	10.47	
			Height	m	7.15	9.75		
			Tube material volum	m <sup>3</sup>	307.51	838.85		
	Tube volume	m <sup>3</sup>	307.51	838.85				
	Buoyant Force	kN	3092.09	8434.89				
	CM BSWL	m	75.77	106.98				
	Mass	ton	573	1159				
	Vol <sub>float</sub> (V)	m <sup>3</sup>	4223	11913				
	M <sub>float</sub> =M <sub>rot</sub> +M <sub>hull</sub> +rotor+ballast+generator module(float)	ton	6047	16601				
			CB(BSWL)	m	34.10	48.35		
			CM(BSWL)	m	43.69	60.63		
			$GM_L = KB + BM_L - KG$		9.63	12.33		
			$L_{float} = h_1+h_2+h_3+h_4+hf$		79.34	152.30		
			$C_{SS,hydro} = \rho g V GM_L$		4.09E+08	1.48E+09		
<b>total</b>			Buoyancy	B=B <sub>1</sub> +B <sub>2</sub> +B <sub>3</sub> +B <sub>4</sub> +B <sub>f</sub>	kN	42460	119785	
	<b>Mass</b>	i)	M <sub>O</sub> =M <sub>hull</sub> (ballast-generator module)	M <sub>O</sub> =M <sub>hull</sub> (ballast-generator module)	ton	778	2201	
		ii)	M <sub>O</sub> =M <sub>rotor</sub> +M <sub>hull</sub> (ballast-generator mo	M <sub>O</sub> =M <sub>rotor</sub> +M <sub>hull</sub> (ballast-generator module)	ton	1390	3890	
		iii)	W <sub>O</sub> =W <sub>rotor</sub> +W <sub>hull</sub> (ballast-generator module)		kN	13633	38162	
	<b>Ballast</b>	iv)	M <sub>O</sub> =M <sub>ballast</sub>	M <sub>O</sub> =M <sub>ballast</sub>	ton	4084	11552	
		M <sub>genmodule</sub>	M <sub>genmodule</sub>	ton	573	1159		
			Total mass	ton	6047	16601		
			Total mass	kN	59323	162858		
			L floater	m	79.3	152.3		

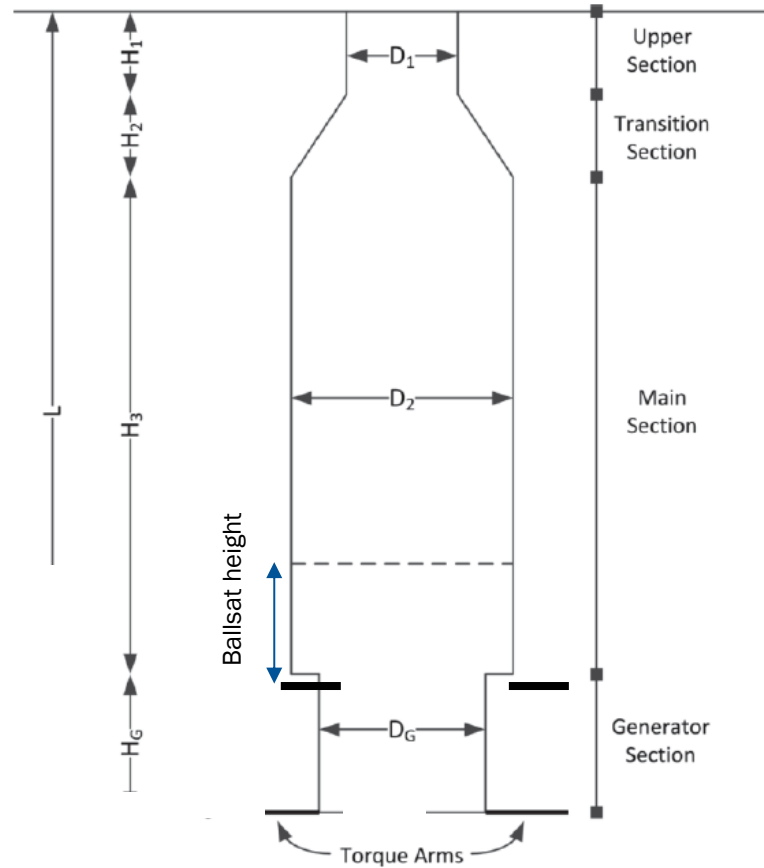


**Figure 52 Schematic overview of the spar buoy floater**

The rotor dimensions after upscaling are given in Table 29 along with some performance characteristics (see also Figure 53, Figure 54).

**Table 29 Rotor basic properties**

Geometry				Performance		
Radius	(R)	[m]	85.5	Rated Power	[MW]	10
Height	(H)	[m]	203.2	Rated speed	[rad/s]	0.42
Chord	(c)	[m]	7.07	Rated Wind Speed	[m/s]	14
Solidity	$\sigma=Nc/R$	[-]	0.165	Cut-in wind speed	[m/s]	5
Swept Area	(S)	[m <sup>2</sup> ]	24000	Cut-out Wind speed	[m/s]	26
Thickness		[-]	0.18			

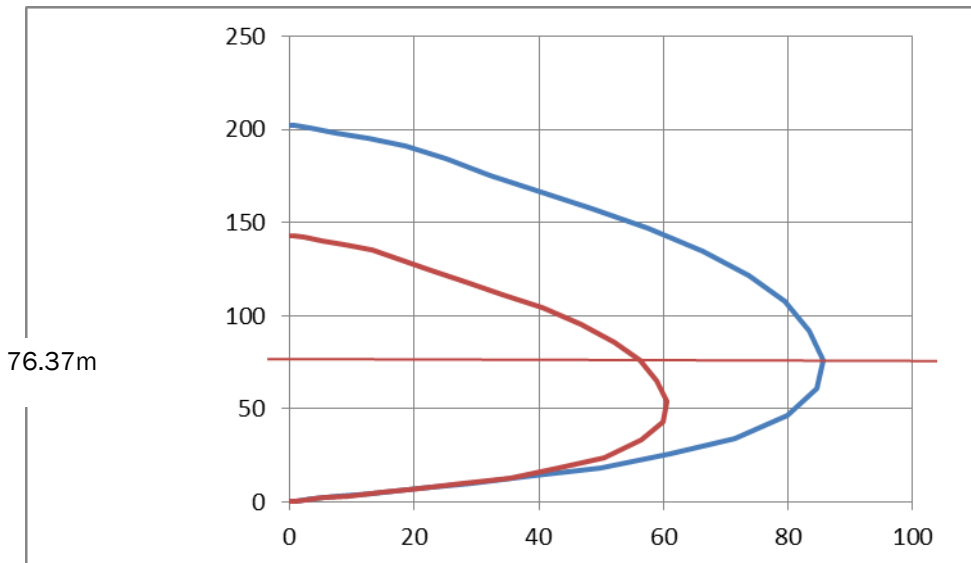


Figure 53: Rotor dimensions comparison between the reference 5MW and the upscaled 10MW DeepWind VAWT, with indication of height at maximum radius

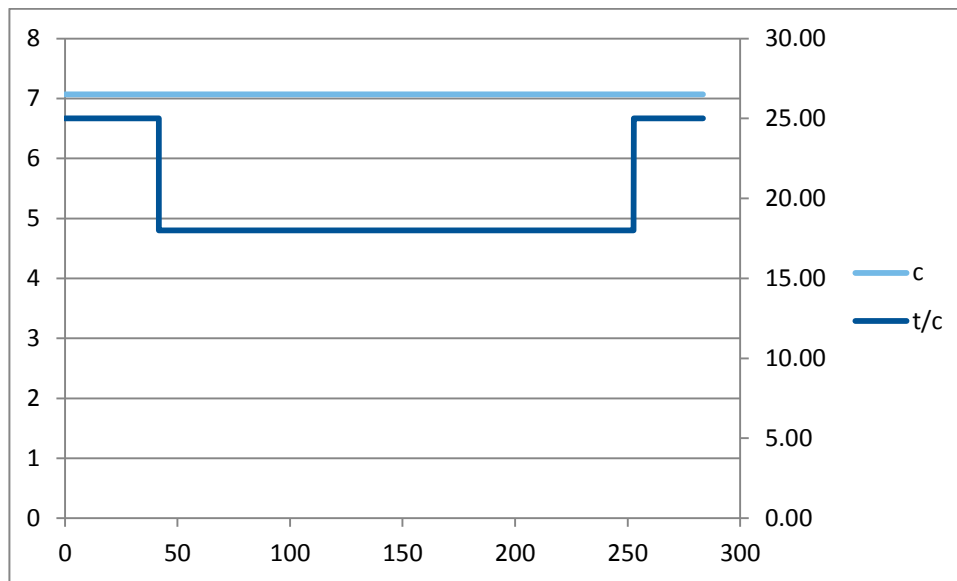


Figure 54: Blade properties of 10 MW design as a function of blade length

### 8.3 Mooring system

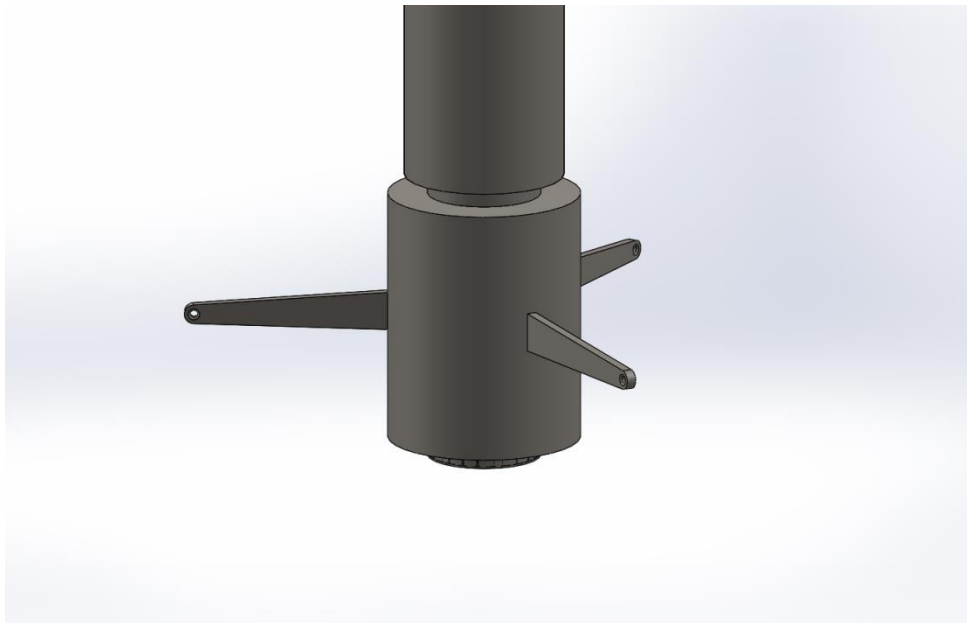
The properties of the mooring system are given in the next Table.

Table 30: Mooring properties

Number of active cables:	3	3
Water depth [m]:	290	268
Water below keel [m]:	110	88

Wet mass [kg/m]:	175.86	195
Total length [m]:	694.4 x 3	882.3 x 3
Mass [T]:	122.1 x 3	172.9 x 3
Elastic modulus Cable [kN/m <sup>2</sup> ]:	6.99e+7	6.99e+7
Cable stiffness EA [N/m]:	6.19E+8	1.65E+9
Cost [M€]:	1.05	1.46
Anchor [M€]	0.17 x 12	0.32 x 12

Three cables are attached to the torque absorption arms as shown in Figure 55. A system of 6 cables is intended to be used in order to provide additional redundancy.



**Figure 55 Generator module with three torque absorption arms, attached to mooring cables (not shown)**

The upscaling from 5MW to 10MW led to the following results regarding the (3) mooring cables: length 854m, cable weight of approximately 195 kg/m. The static equilibrium as per overview of the mooring system, gave an optimum layout at 694 m cable (122T) with stiffness EA= 1.65e9 Nm/m. This setup was tried, but as explained next it did not provide adequate yaw stiffness.

Trying out this setup in a simulated run at 26m/s with no controller, at a fixed angular speed of 0.24 rad/s, large mean values and variations in cable tension appeared as well as in the generator torque signal. Trying out several combinations of anchor position, depth below keel, EA, and torque arm lever resulted in data, for which a representative subset is shown in Figure 57. A review of yaw stiffness sensitivity for the 5MW turbine can be found in (Berthelsen, Fylling,Vita, Paulsen:Conceptual design of a floating support structure and mooring System for a vertical axis wind turbine OMAE2012-83335), and a result for pretension selection for 5 MW is reprinted in Figure 56, as well as illustrating restoring moments created by the cables.

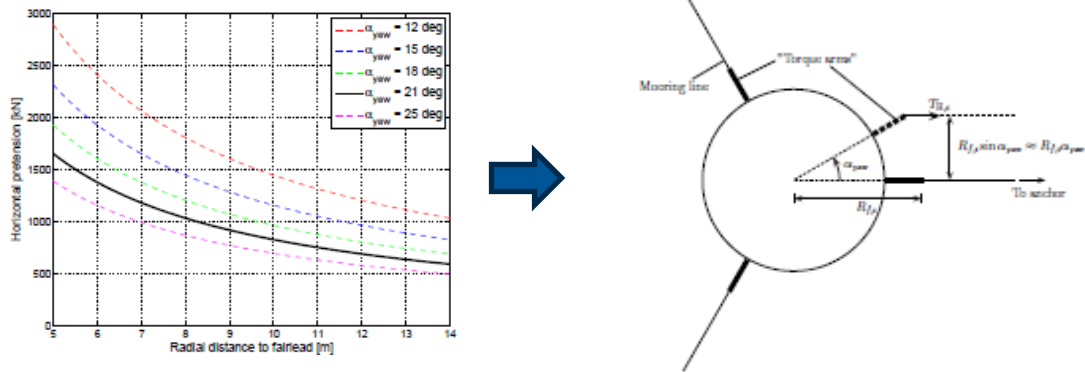


Figure 56: Left: Required horizontal pretension as function of radial distance, Right: Overview of buoy with concentric mooring system illustrating restoring moment from cables [Berthelsen et al]

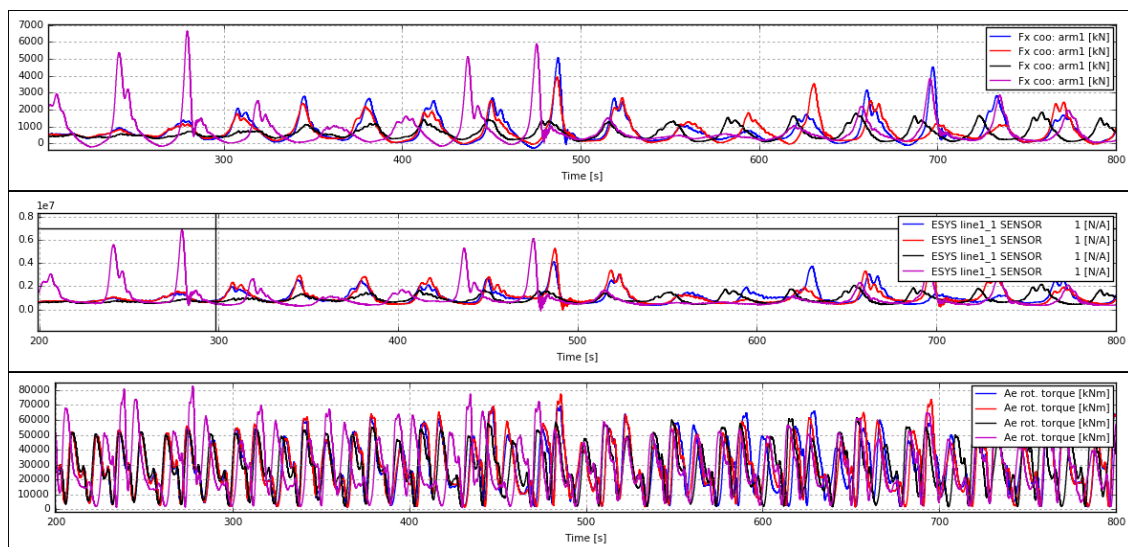


Figure 57 Top: tangential force at knucklehead position for fairlead arm 1. Middle: cable force in [N]. Bottom: aerodynamic torque Blue: torque arm Cd=1.3, Red: Cd=1 (distance to sea bed: 88m, distance from fairlead to anchor:854m, arm 18.3m) Black: arm 22.0m Purple: 712m distance between fairlead and anchor. Arm1 is co-parallel with the global co-ordinate system in the y-direction (parallel to wind direction)

The results show that there is a tradeoff between the cable weight suspended over the horizontal distance, a force triangle of the vertical force and the thrust force, and the cable stress. The worst case is a relatively short cable providing mooring cable forces exceeding the minimum break load of 6594 kN by 20%. In contrast to previous results, the plot reveals, that torque absorption with 20% longer arm reduces the cable forces considerably down to a level of 100T cable tension, resulting in a safety factor of more than 4 (recommendation is 1.75) and at 15% MBL. As shown in the bottom part of the figure, it will give a minor influence on the torque generation, which is balanced by torsional elasticity of the spar. In this context, with constant rpm at rated power of 10MW - the average rotor torque from the plot reads around 27-29000 kNm on average. This shows that control becomes very important in limiting the power. From the power variability and the discussion on the controls it is clear that the controller that was available is not capable of keeping the power constant.

Another possibility is to use clump weights, which is a very low-cost solution, that may reduce the cost of the mooring system with respect to the cable length. A configuration with cable length as before (=866m) and clump weights of 28.9T each has been applied. The weights were concrete cylinders of 1 m length and 3.67m diameter.

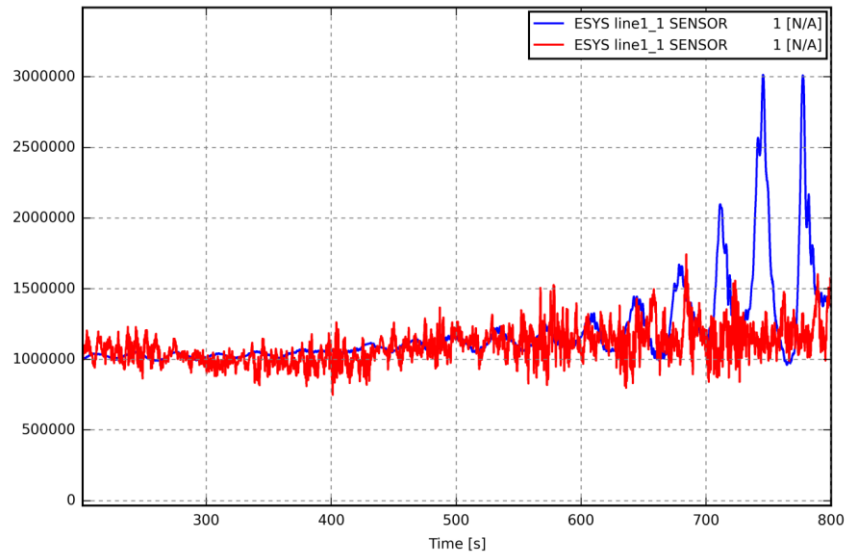


Figure 58 Effect of adding damping (red) to the clump weight body

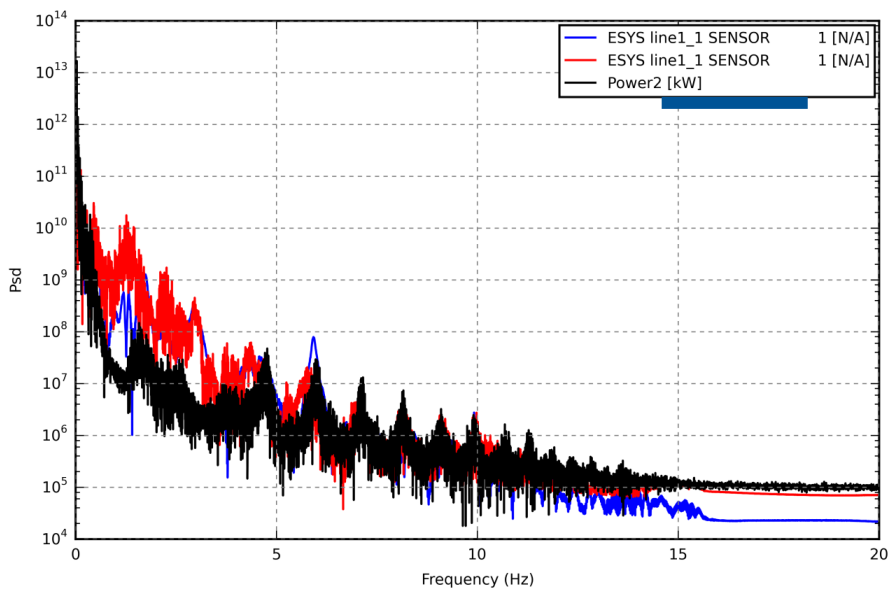


Figure 59 Power spectrum of cable1 axial forces with damping (red) and without (blue) and 22m arm1 configuration (black)

Adding appropriate damping will prevent energy being pumped into the complete system, as shown in Figure 58. Because the cable force is well below 200T tension, this is chosen as an ad hoc solution instead of using 22m torque arms. In the spectral space, the tension peaks seem to

appear more or less regularly as indicated in Figure 59. On the other hand, attention is needed at low frequencies that may clash with the accentuations of waves and currents.

### 8.3.1 Decay testing:

The Heave characteristic period is found by releasing the floater around 30 m below the normal position and releasing it; the period read from Figure 61 as 31.95 seconds, or 0.031Hz. Swaying the generator module -40m in the y-direction, then releasing it will provide the following pattern as shown in Figure 62 with a characteristic period of about 41s. In summary, the main characteristic of the floater with turbine on, is that it responds with periods of around 32-41 seconds. This result of the upscaling is a preliminary finding which may cause unfavorable interference with wave excitations experienced at the site.

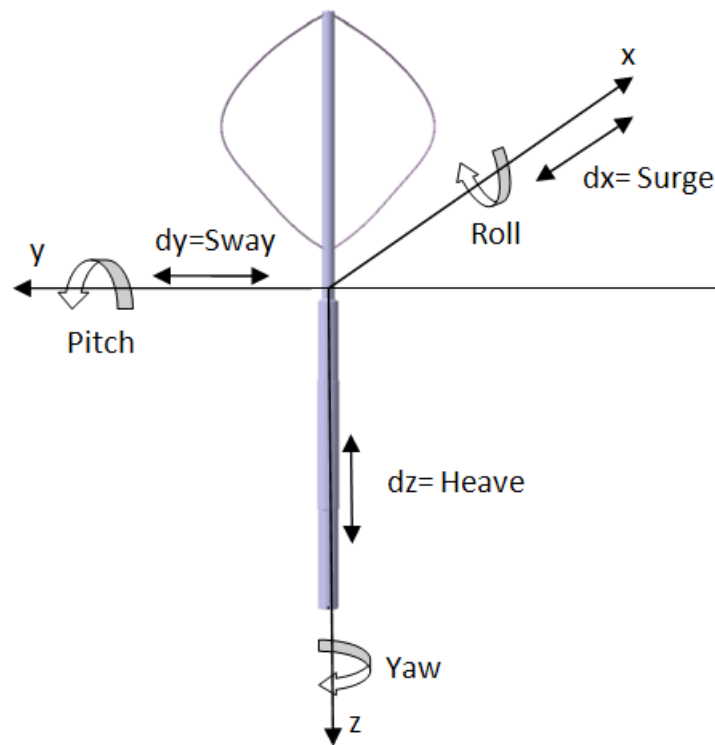


Figure 60 Overview of nomenclature for DOF

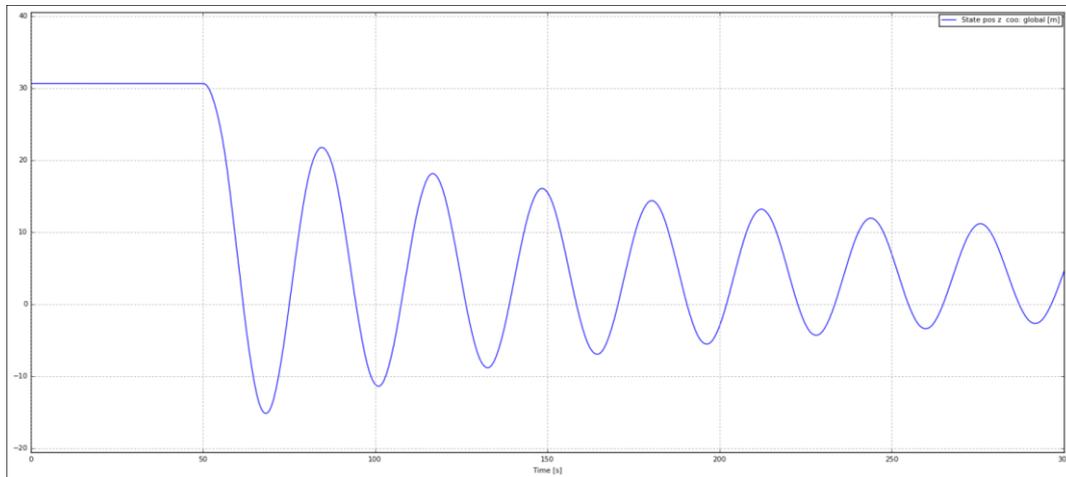


Figure 61 Floater decay-heave. Periodicity 31.96 seconds

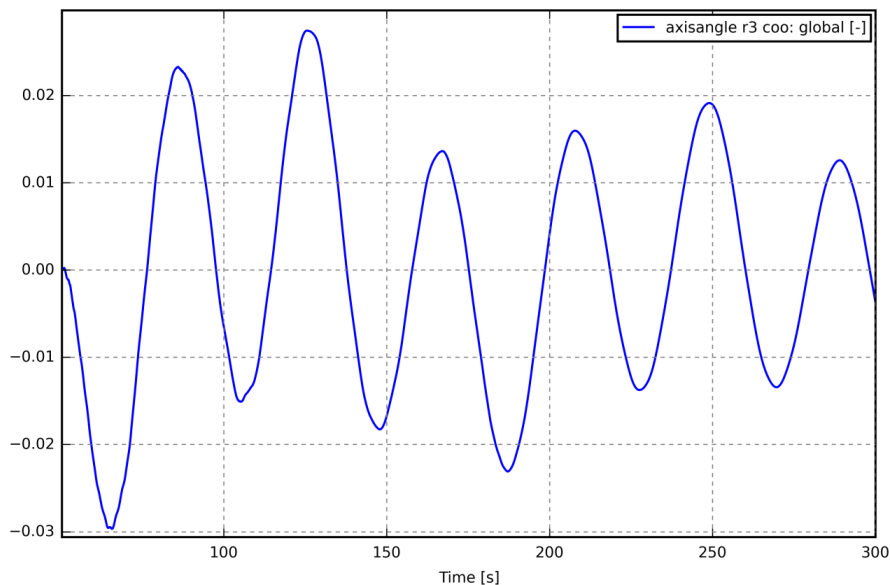


Figure 62 Pitch/roll response [radians] for concept, period is 40.98 seconds

## 8.4 Controller.

The controller originally developed by Sintef [ (Harald Svendsen: Description of simplified numerical model relevant for development of control concepts. TR A7179 2012)] for the 5 MW could not be implemented for the 10MW, since the controller was specifically hard coded for the 5MW with a HAWC2 DLL.

Instead a PI rotor speed controller has been adopted for the purpose, based on an induction generator model operated at variable frequency as seen on the controller scheme [ (Christos Galinos (3): Variable speed control for Vertical Axis Wind Turbine. DTU Wind Energy Report I 0627(EN) 2017), (Torben Larsen: Slip generator model implemented in HAWC2 as an external DLL Wind Energy Department 2005-12-05 J.nr. 200500523)]. The generator dynamics are

approximated by a first order differential equation with a prescribed slip. In order to allow variability in the rotor speed an inverter is assumed which changes the nominal generator speed. Below rated power the optimum tip speed ratio is tracked, while above the power is constrained to rated. The wind speed which is needed in the control it is considered as a known signal and used after a first order low pass filtering with a certain time-constant.

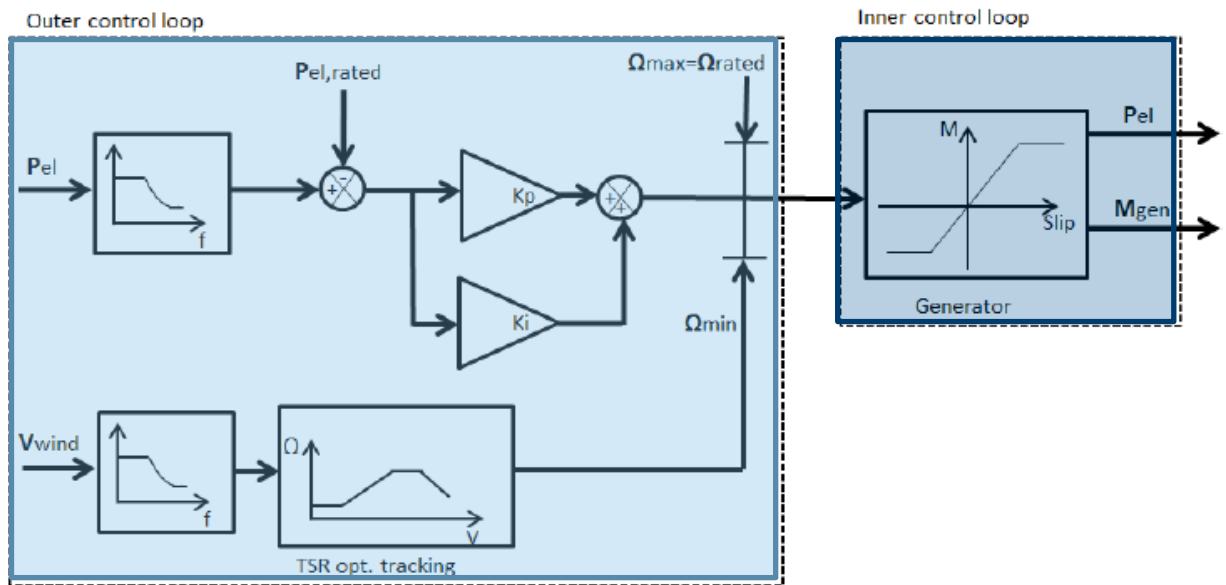


Figure 63: Controller scheme

The filtering of  $P_{el}$  turned out to be more complicated for this two-bladed configuration in comparison with the reference case used in the report (Christos Galinos (3): Variable speed control for Vertical Axis Wind Turbine. DTU Wind Energy Report I 0627(EN) 2017), and smoothening of the electrical power seems not that effective than with the 5 MW Sintef controller. The top figure3 represents two different filter constants of 30 and 60 seconds for two different low pass wind speed filter settings. The bottom figure reflects a more effective low pass filter on power. However, a complete rotor cycle lasts 15 seconds, and the applied low pass filter time seems to be very long, with time constant equivalent to 20 rotor cycles. It is obvious, that these observed strong variations will cause load specific parameters in the model to trend erroneous results, and that correction will need more studies.

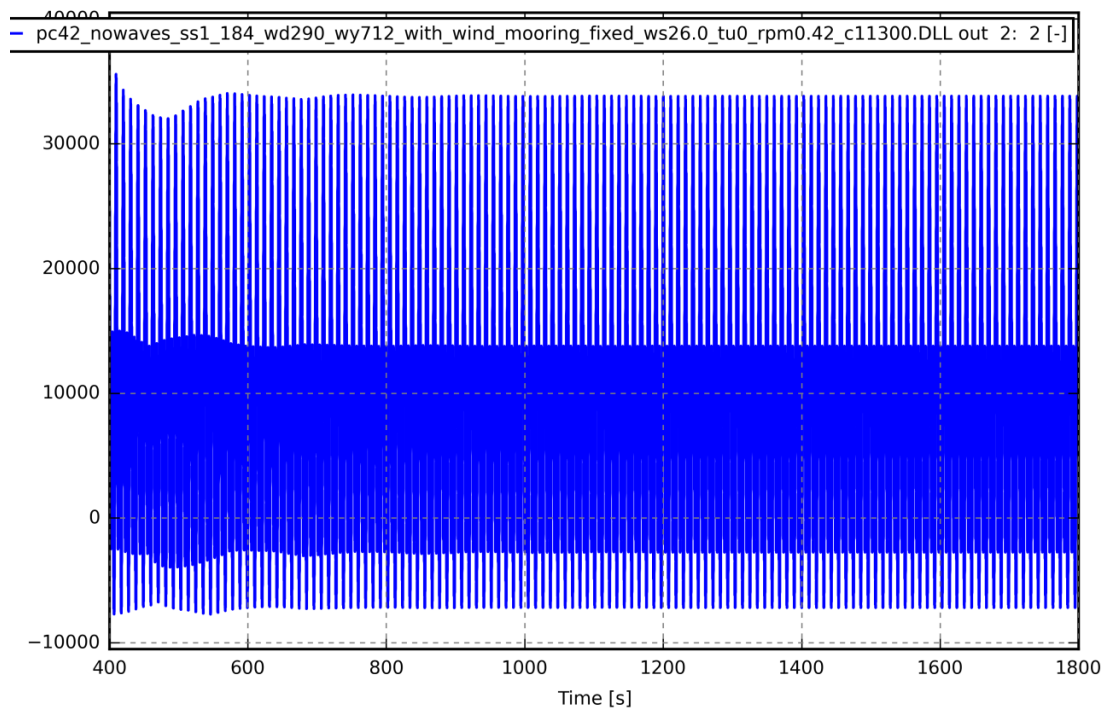
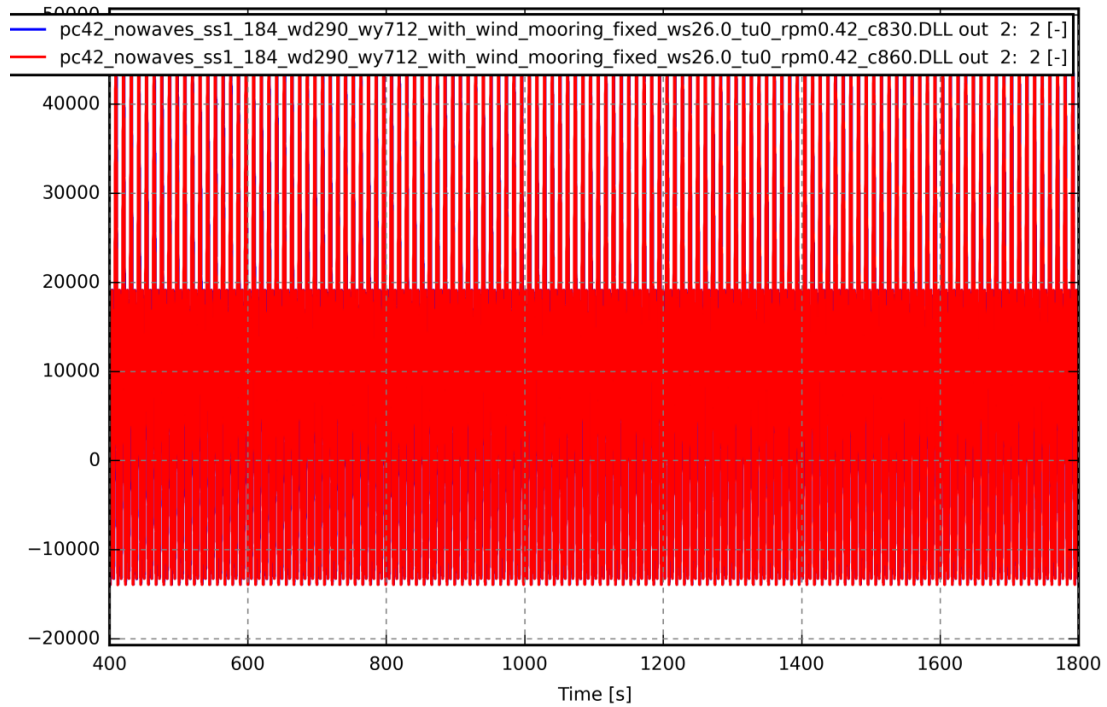


Figure 64: controller tuning attempts

## 8.5 Energy production and cost estimations

The power curve calculations have been carried out in uniform wind inflow conditions using the default controller constants as per top Figure 64). The power curve is shown in Figure 65 (and tabulated in Table 31) in comparison to the targeted one derived directly from the upscaling. The sdv values given in the Table are high compared to the averaged values which indicates that the control does not adequately average the fluctuations which will impact on the loads.<sup>1</sup>

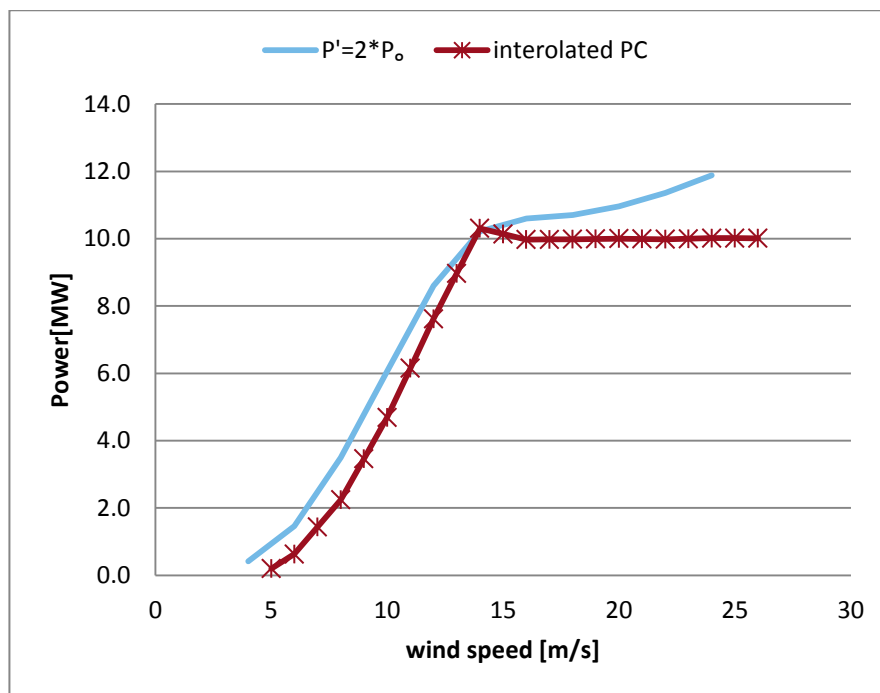


Figure 65 Power curve 10 MW FVAWT

Table 31 Power curve

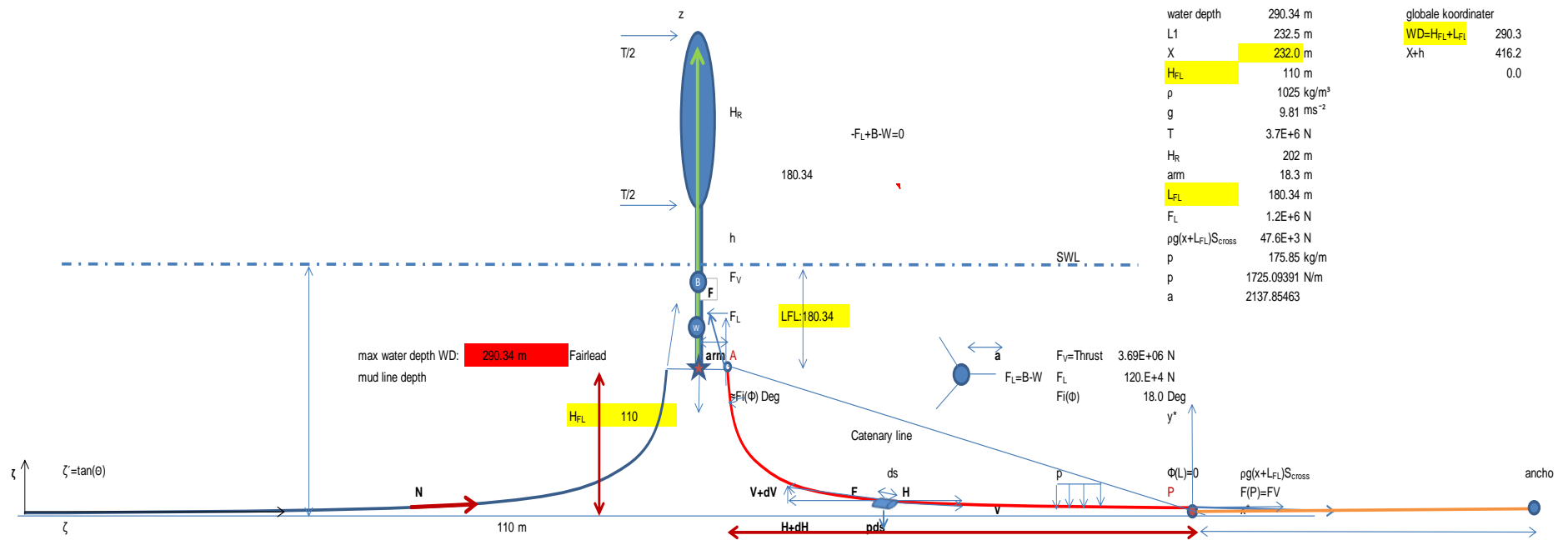
wind speed [m/s]	Mean(Pe) [kW]	Stdev(Pe) [kW]	Min(Pe) [kW]	Max(Pe) [kW]
4	-229.27	325.25	-659.31	303.65
6	633.81	862.38	-719.24	2200.36
8	2242.82	2045.98	-1114.40	5842.21
10	4690.47	3967.23	-1537.39	11633.12
12	7622.11	6353.13	-1337.02	19032.32
14	10308.38	8548.41	-604.31	25613.31
16	9971.75	12786.23	-6250.82	33298.88

<sup>1</sup> See (David Verelst et al: Detailed Load Analysis of the baseline 5MW DeepWind Concept , DTU Wind Energy E-0057, 2014), on the detailed loads analysis of the 5 MW concept

18	9982.99	13120.31	-5810.37	35578.24
20	10004.14	13324.06	-6363.93	37462.40
22	9980.64	13806.30	-8432.95	37890.24
24	10015.44	14995.25	-10802.86	38973.12
26	10013.57	15946.30	-11015.47	41232.32

Power energy production has been estimated for Site B of the Life50+ project. Site B has a yearly average wind speed of 10.46m/s, with Weibull constants  $A=6.214$  (121m aswl), and  $k=1.701$ .

The AEP for site B, from the 10MW WT and the power curve data given in Table 31 is 40.6GWh (See Figure 65, Figure 66). For a Rayleigh distribution ( $k=2$ ), the AEP=43GWh. Under the same conditions the 5MW design would result with 24.9MWh which upscaled gives AEP 49.8MWh. There is a difference of 23 % between what may be achieved and what is at present obtained. This is probably due to the inadequacy of the controller which does not achieve the highest aerodynamic performance.



v annual mean	ws			dv	F(V <sub>i-1</sub> )	F(V <sub>i</sub> )	f(v)	f(v)dv	Σf(v)dv	P0=2*P <sub>5MW</sub>	P0(v) f(v)dv	P1(10 MW)	P1(v) f(v)dv
	from	to	v										
10.46	1	3	2	2	0.007153	0.062563	0.055410	0.055410	0.055410	0	0	0	0
	3	5	4	2	0.062563	0.164278	0.101716	0.101716	0.157126	0.4	374232	0.000	0
	5	7	6	2	0.164278	0.296537	0.132259	0.132259	0.289385	1.5	1691543	0.634	734328
	7	9	8	2	0.296537	0.440912	0.144375	0.144375	0.433760	3.5	4426531	2.243	2836545
	9	11	10	2	0.440912	0.580455	0.139543	0.139543	0.573302	6.1	7407701	4.690	5733595
	11	13	12	2	0.580455	0.702739	0.122285	0.122285	0.695587	8.6	9212437	7.622	8164907
	13	15	14	2	0.702739	0.801136	0.098397	0.098397	0.793984	10.2	8809193	10.308	8885376
	15	17	16	2	0.801136	0.874387	0.073251	0.073251	0.867235	10.6	6801795	9.972	6398661
	17	19	18	2	0.874387	0.925085	0.050697	0.050697	0.917932	10.7	4751955	9.983	4433524
	19	21	20	2	0.925085	0.957814	0.032729	0.032729	0.950661	11.0	3142335	10.004	2868282
	21	23	22	2	0.957814	0.977757	0.019756	0.019756	0.970417	11.4	1966011	9.981	1727293
	23	25	24	2	0.977757	0.98874	0.011170	0.011170	0.981587	11.9	1162418	10.015	979978
	25	27	26	2	0.98874	0.994663	0.005923	0.005923	0.987510	0.0	0	10.014	979794
							Σ	0.987510					
												49746 MWh	43742 MWh

v annual mean ws	k= 1.701	A(121m) k		Weibull C factor		hours	P1(MW)	P1(v) f(v)dv	
		11.72371	1.701	11.72371					
10.46 from	to	dv	F(V <sub>i-1</sub> )	F(V <sub>i</sub> )	f(v)	f(v)dv	Σf(v)dv		
0	1	1	1.00000	0.984926	0.01507	0.01507	132.048		
1	3	2	0.984926	0.906264	0.07866	0.07866	689.079	0	
3	5	4	0.906264	0.790827	0.11544	0.11544	1011.226	0	
5	7	6	0.790827	0.659719	0.13111	0.13111	1148.508	0.634	
7	9	8	0.659719	0.528452	0.13127	0.13127	1149.899	2.243	
9	11	10	0.528452	0.407676	0.12078	0.12078	1057.998	4.690	
11	13	12	0.407676	0.303562	0.10411	0.10411	912.038	7.622	
13	15	14	0.303562	0.218553	0.08501	0.08501	744.682	10.308	
15	17	16	0.218553	0.152355	0.06620	0.06620	579.892	9.972	
17	19	18	0.152355	0.102959	0.04940	0.04940	432.707	9.983	
19	21	20	0.102959	0.067519	0.03544	0.03544	310.459	10.004	
21	23	22	0.067519	0.043005	0.02451	0.02451	214.740	9.981	
23	25	24	0.043005	0.026625	0.01638	0.01638	143.489	10.015	
25	27	26	0.026625	0.016034	0.01059	0.01059	92.778	10.014	
27	50 >27				0.01603		140		
					sum	0.99999 h(annual)	8760	MWh	40615 MWh

Figure 66 Upper: Mooring system overview Lower: AEP for site B (Rayleigh distribution, k=2, and actual k=1.701)

#### Cost estimation:

The cost basis is developed from the 5MW Deepwind study.

Component	Cost per unit	Unit	Cost
Blades			(2 blades)
They are pultruded	6€/kg	129200kg/blade	775.200,00
Generator	12€/kg	294000kg (generator) + 261020kg (enclosure) = 555000kg	6.660.000,00
Bearings			546.000,00
Tower			
The tower is made of construction steel	3.75€/kg	1079000kg	4.046.250,00
Floater			
The floater is made of structural steel	3€/kg	1866780kg (+	5.600.340,00
Ballast	0.05€/kg	7588000kg	379.400,00
Mooring system (*)			4.000.000,00
			22.006.940,00

(\*) The mooring system is dimensioned to keep it stationed at 26 m/s wind speed. The depth below keel was set to 110m (due to optimization), which brings the required water depth to 290.1m. The distance to the fairlead is 180.34m. For the case a unit cost of 2875€/ton, and the anchor cost is a rough estimate on the basis of anchors intended for a 20MW floater. The estimated cost of a mooring system is accordingly 3M€-5M€. The anchor type is drag embedded type. A remarkable difference with the 5MW mooring system is that the water depth was set at 220m, and the anchor radius was approximately 1000m - here it is quite less and on the expense of a bulkier cable type. The 220m water depth equivalent for the 10MW is 268.4m.

For a 20years period, the cost per KWh is 0.027€/kWh for the case of 41GWh per year estimation and accordingly for the other ones. This estimation does not include other costs.

## 8.6 Discussion

The above analysis and in particular the cost estimation are subjected to certain reservations. As mentioned the direct upscale of the existing design from 5 to 10MW was not successful in terms of going from a 5MW cost of 1200-1800€/kW to a cost of 2200€/kW for the 10MW. Time and allocated effort did not allow proper design of a 10MW VAWT. A dedicated controller was needed and the floater had to be fine-tuned for the 10MW case, in order to carry the design verification as done for the HAWT.

## 9 OUTLOOK FOR THE DESIGN SOLUTIONS OF FLOATING WIND TURBINES

### 9.1 Introduction

In the current stage, the structural design verification in Section 7 is based on frequency analysis of the loads. However, loads at the connection point between the tower and the floating platform are pre-calculated by simulation tools that assume a rigid floating platform, yet a flexible platform exhibits different excitation frequency and flexible modes can be significantly excited, increasing the predicted loads (Borg, Hansen, & Bredmose, 2016). Nonetheless, performing a coupled simulation of aerodynamic and hydrodynamic loads on floating wind turbines for fatigue analysis is complex subject due to the increase computational cost of calculating the hydrodynamic effects on the platform. Obtaining the time-domain pressures on the wetted surface to be used in a model solver is not a trivial task.

Simulation software, such as NREL's FAST (NWTC, NWTC Information Portal (FAST v8), 2016), can reproduce the motions and loads of the turbine, mooring system and tower with good accuracy and resolution (Allen C. K., Goupee, Dagher, & Viselli, 2015). The hydro-aero-servo-elastic simulation tools can use the results from a first order hydrodynamics solver in the frequency domain and transform them in a way to be used in the time domain simulation. However, the forces on the floating platform are simplified such that its deformation is not taken into account. Distributed wave loads on the platform are not calculated and thus show the possibility of the implementation of software for structural analysis. This is a topic of research which has also been dealt with by (Kvittem & Moan, 2015) and (Luan, Gao, & Moan, 2017).

In this section, a procedure is described for future investigation in order to be able to utilize results of first order wave loads on a finite element model for the structural design and verification of the floating platform. The main concept for this approach is to use the output data from a Boundary Element Methods (BEM) or numerical panel code methods dedicated to the computation of first order wave loads on offshore structures (added mass, radiation damping, diffraction forces) for dynamic analysis. The frequency dependent results calculated by the BEM software can then be processed and transferred to a finite element model which allows time domain simulations of the platform.

### 9.2 Pressure mapping for finite element analysis

To obtain a time domain simulation of a floating body there are several processes that need to be intertwined. These have been outlined schematically in Figure 67.

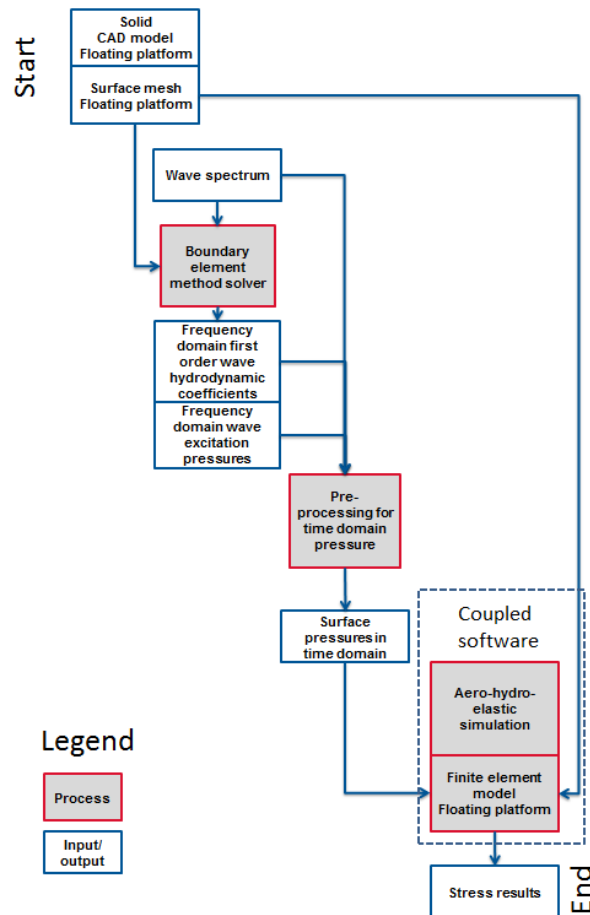


Figure 67: Process chain for expansion pass of loads on floating platform for pressure mapping in a time domain simulation

As can be seen in the Figure 67, the time domain simulation uses two separate softwares for calculating loads. One models the hydrodynamics of the floating platform (Boundary element method solver) and the other one the aero-elastic behaviour of the turbine (Aero-hydro-elastic simulation). These loads are transferred as inputs for the finite element model of the floating platform for the calculation of the dynamic response and stresses.

### 9.2.1 Boundary element method solver

A BEM software can be used for calculation of the frequency domain first order wave loads, for example NEMOH (Barbit & Delhommeau, 2015). The BEM software takes a solid structure and discretizes it into a surface model with panels and respective nodes. This is the mesh. For these panels, the radiation and diffraction fields of pressure for each desired frequency can be calculated. That is, for every frequency of the incident wave, the software solves one diffraction problem and one problem for the movement of the body for each of the six degrees of freedom of each panel. This is done assuming free surface potential flow theory. The theory describing the processed used by NEMOH for calculating these outputs is given in (Delhommeau, 1987).

### 9.2.2 Aero-hydro-elastic simulations

There have been several methods that could be implemented for the analysis of time domain simulation of offshore platforms. Similar to the process described in Section 7, (Allen C. , Goupee, Viselli, & Dagher, 2017) and (Walia , 2015) use a method in which the loads are pre-calculated, and then applied as section forces on the floating platform. In these pre-calculations, an aero-

hydro-elastic software (such as FAST) can be used to compute the cross-sectional forces on a rigid model of the platform.

As mentioned beforehand, including the flexibility of the floating platform changes the eigenfrequencies of the model and thus it is worth to integrate the simulation software. In this way, a coupled simulation, linking the two models of the aero-elastic simulation tool with that from the floating platform, could lead to a more accurate representation of the loads.

Coupling of such software specializing in the calculation of aerodynamics, elastic or hydrodynamic loads has already been implemented for fixed bottom onshore and offshore turbine such as describe in (Stache & Ehlers, 2009), (Kaufer, Cosack, Böker, Seidel, & Kühn, 2009), and its implementation is available between ANSYS and Flex5.

### 9.2.3 Pre-processing for time domain pressures

Before analysis of the finite element model can occur, the hydrodynamic coefficients and the wave excitation pressure on the floating platform have to be calculated. As mentioned beforehand, the frequency domain results can be obtained with the software NEMOH. This software takes a geometric mesh of the wetted surface of the underwater part of the platform and outputs among other things, the frequency dependent hydrodynamic coefficients and wave excitation pressures on each of those mesh elements.

In order to use results from each mesh element in a time domain simulation, processing of the frequency domain excitation and radiation forces needs to be done.

#### 9.2.3.1 Wave excitation pressures

The wave excitation pressures on each panel element of the platform are calculated by adding the Froude-Krylov pressure to the diffraction pressures. These are dependent on the wave frequency. The formulas for these in the time domain are as follows:

$$P_{exc} = P_{FK} + P_{diff} \quad (2)$$

$$P_{FK}(t) = \sum_{n=1}^{N_{\omega}} \rho g H_n f_o(z) \cos(k_{\omega} x - \omega_n t + \epsilon_{\omega}) \quad (3)$$

$$P_{diff}(t) = \sum_{n=1}^{N_{\omega}} \text{Re} \left( H_n |\tilde{P}_{diff}(\omega_n)| e^{-i(\omega_n t - \angle \tilde{P}_{diff}(\omega_n) + \epsilon_{\omega})} \right) \quad (4)$$

Where  $P$  is the Froude-Krylov or diffraction pressure,  $\rho$  is the density of the water,  $g$  is the acceleration due to gravity,  $H$  is the amplitude of the wave,  $\omega$  is the wave frequency,  $t$  is time,  $k$  is the wave number,  $x$  the coordinate of the panel location,  $N$  the number of wave frequencies and  $\epsilon$  is the random phase shift of the wave frequency as per the wave spectrum.  $\tilde{P}_{diff}$  is the complex number representing the pressure (normalized to the wave height) for each panel and  $\angle \tilde{P}_{diff}$  is the angle of the complex number. Both are an output of the BEM software.

$f_o$  is dependent on the water depth so that,

$$f_o(z) = e^{kz} \text{ for deep water} \quad (5)$$

$$f_o(z) = \frac{\cosh(k(z+h))}{\cosh(kh)} \text{ for intermediate water depth} \quad (6)$$

When not assuming deep water depths,  $K$  can be solved using a numerical approach.

Important to remember, for equation (3) and (4), a simulation will usually use a wave spectrum  $S$  (for example the JONSWAP spectrum) to take into account the distribution of the energy in the waves over the different frequencies. Therefore, in these equations, instead of taking the integration of the wave force over all the frequencies, an approximation is made through which constant successive frequencies are taken in increments of  $\Delta\omega$  such that:

$$\frac{H_n^2}{2} = S(\omega_n)\Delta\omega \quad (7)$$

As proposed by (Massel, 1996), it is recommended to choose a cut-off frequency when doing the analysis. This is proportional to the peak spectral frequency and 3 times its magnitude.

### 9.2.3.2 Radiation pressures

The calculation of the pressures due to radiation, meaning added mass and radiation damping, in the time domain require a more complicated procedure.

The time domain linear representation of the hydrodynamic forces acting on the platform is given by (Cummins, 1962) and also summarized in (Jonkman J. , Dynamics Modeling and Loads Analysis of an Offshore Floating Wind Turbine, 2007), are shown in equation (8)

$$F_i^{Hydro} = F_i^{waves} + \rho g V_0 \delta_{i3} - C_{ij}^{Hydrostatic} q_j - \int_0^t K_{ij}(t - \tau) \dot{q}(\tau) d\tau \quad (8)$$

Where  $F_i^{hydro}$  is the  $i^{th}$  component of the applied hydrodynamic load on the support platform associated with everything but the added mass  $A$ ,  $F^{waves}$  are the excitation forces,  $V_0$  is the displaced volume of fluid when the support platform is in its undisplaced position,  $\delta_{i3}$  is the  $(i,3)$  component of the Kronecker-Delta function (i.e., identity matrix) and  $C_{ij}^{Hydrostatic}$  is the  $(i,j)$  component of the linear hydrostatic-restoring matrix,  $q_j$  is the displacement in the direction of the  $j^{th}$  degree of freedom,  $K(t)$  is the impulse response function according to (Cummins, 1962).

The convolution integral represents the load contribution from wave-radiation damping and also represents an additional contribution from added mass. The convolution thus takes into account transient effects which would not be the case in a frequency domain analysis. These transients are due to the pressure forces from the radiated waves by a motion impulse of the hull of the platform.

The calculation of the convolution and the impulse response function in the scale of every panel of the mesh of the floating platform is left out of the scope of this section.

### 9.2.3.3 Added Mass

From the results from Nemoh, a wave frequency dependent complex number is output for each panel, from which the impulsive hydrodynamic added mass can be calculated. This is done by adding the forces and moments resulting on each panel with respect to a reference point. For the situation at hand, the calculation of the pressure on each panel is more interesting. The output from Nemoh is thus used in the following formulas to calculate the pressure cause by the added mass.

$$A_{panel_{idof}}(\omega) = Re(P_{Rad}) : \text{Nemoh convention} \quad (9)$$

$$B_{panel_{idof}}(\omega) = -Imaginary(P_{Rad})/\omega : \text{Nemoh convention} \quad (10)$$

$$P_{added\_mass\_panel} = \sum_{i_{DOF}=1}^6 A_{panel_{idof}}(\infty) * \ddot{q}_{idof}(t) \quad (11)$$

Where  $P_{radiation}$  is a complex number that is an output of Nemoh representing the contributions of added mass and radiation damping of each panel,  $P_{added\_mass\_panel}$  is the pressure due to the added mass on each panel,  $A_{panel}$  is the added mass contribution of each panel for each degree of freedom, and its value at infinite frequency is approximated as the output of Nemoh for a frequency equal to the cut-off frequency of the wave spectrum,  $B_{panel}$  is the radiation damping contribution of each panel for each degree of freedom and which is an output of Nemoh, and  $\ddot{q}$  is the acceleration/rotational acceleration of the panel for each of its degrees of freedom.

#### 9.2.3.4 Hydrostatic

Additionally the hydrostatic pressure is added to each panel's pressure. This pressure is due to the head of water, and is taken as proportional to the instantaneous z coordinates of the panels below the mean sea level.

For additional information on time domain calculations of forces on floating platforms see Chapter 2 of (Jonkman J. , Dynamics Modeling and Loads Analysis of an Offshore Floating Wind Turbine, 2007).

#### 9.2.4 Finite element model of floating platform

Based on the solid model of the floating platform (Figure 68) a finite element model can be developed. From the solid model, a finite element model of the floating platform is created to take the inputs of the pre-processed time domain pressures for each panel of its mesh. These pressures represent the excitation and diffraction pressures, and are only calculated for the wet surface under the mean water level. An example of a mesh and pressure map for the excitation pressure on the underwater surface meshed TripleSpar is shown in Figure 69.



Figure 68: : model of the floating platform in ANSYS

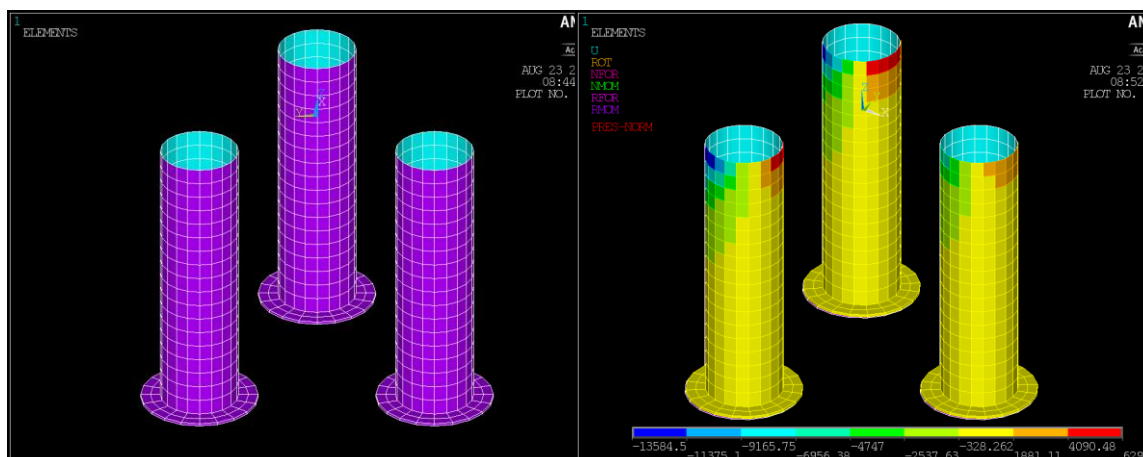


Figure 69: Left- mesh of underwater part of TripleSpar. Right- pressure map of excitation pressures of one load step from a regular wave coming from the x direction applied on the mesh

### 9.2.5 Example time domain simulation of excitation pressures

Exemplary results from the stresses of a 60 second simulations of the Froude-Krylov loads and the diffraction loads on the TripleSpar are shown in Figure 70. For demonstration purposes the hydrostatics, added mass and radiation damping have been left out. Here, a regular wave with a period of 5 seconds and amplitude of 1 meter has been used. Additionally, the steel connection of the column to the tower is assumed to be rigid, unlike the model already used in in Section 7.

Also, for this particular example, because the calculation of excitation forces assumes the platform to be fixed, the simulation in the time domain of the stresses for excitation pressures fixes the connection point of the platform to the turbine tower while allowing the TripleSpar columns to deform.

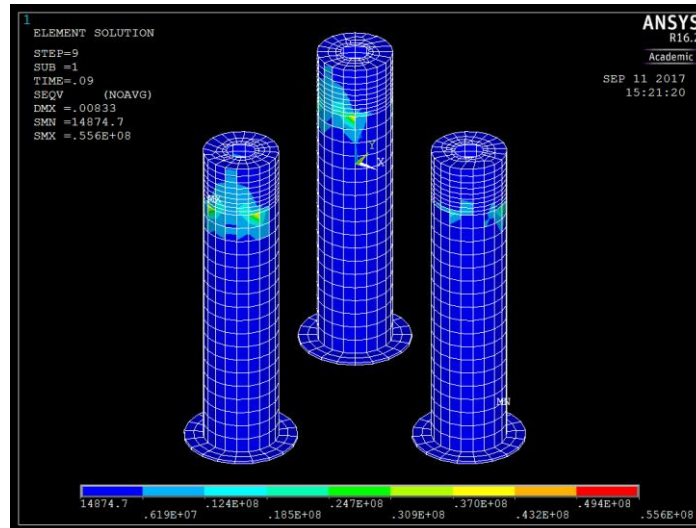


Figure 70: von Mises stress on the floating platform for the simulation of wave excitation forces

The example shows the flexibility of the pressure mapping procedure shown in Figure 67, since it allows the superposition of different effects in the form of added pressures to each of the mesh panels under the water line. This comes from the assumption of linearization of the hydrodynamics problem.

However, the increase of the model complexity of the platform also means simulation time for such a procedure is much larger than that of a simulation that assumes a rigid platform. For the 60 second simulation with 6000 time steps of the TripleSpar with 2322 four-sided finite elements on an Intel core-i5 with 2.7GHz, the time to complete was about 2 days. The actual simulation of the platform under a normal sea state would therefore take a disproportionately long time considering most floating offshore simulation require one simulation to be of 3 hours of operation.

### 9.3 Summary and considerations

The procedure outlined in Figure 67 serves the purpose to help analyse a time domain simulation and the stresses on the floating platform through pressure mapping for the design ultimate and fatigue loads specified in the IEC 61400-3 (International-Electrotechnical-Commission, 2009). This attempts to advance current design practices already shown in previous sections since they assume the floating platform is rigid when performing time domain simulations. An example of its application is shown by pressure mapping the excitation loads of a regular wave on a finite element model of the TripleSpar platform. The procedure can then help designers with calculation of maximum stresses for the design load cases with normal sea states, as well as determination of time varying stresses needed for fatigue calculations.

In the current state of research, the BEM software has to be checked for convergence of parts with relative thin thicknesses such as the heave plates. Finally, results need to be expanded to include the diffraction, turbine, and mooring lines loads, while verifying them with the solution from high fidelity computational fluid dynamic models (which are more computationally time consuming).

Furthermore, it is found that the BEM software can limit the amount of panels that can be analysed and therefore might not lead to a converged solution for the mesh of the FEA model. Also, as with current state of the art time domain simulations, an initial run up period will be needed for the simulation to overcome initial transients. This will significantly increase processing time. This simulation time was already very large for the example given where the 6000 step

simulation took over 2 days. When considering the complexity that it would take to model the whole platform with enough panel for convergence and with a several simulation seeds to take into account turbulence seeds, wave direction, wind wave misalignment, the process could be too time consuming for the design engineers to model the fatigue.

## 10 CONCLUSIONS

A floating platform for the INNWIND 10MW wind turbine has been successfully designed, including the structural analysis, the control strategy and the mooring system. The platform is a hybrid design between the typologies spar and semisubmersible to combine the advantages of both concepts. The platform is composed of three cylinders that provide stability and allow the draft of the platform to be moderate, which is an important advantage for the installation and facilitates the adaptation of the design to locations with different water depths. In addition, the use of concrete cylinders makes easier the manufacturing and has smaller material costs. Heave plates at the bottom of the columns are added to increase the heave damping. A transition piece has been designed in steel to connect the wind turbine to the supporting cylinders. This floater concept has been called TripleSpar.

The design of the platform followed a methodology of increasing analysis complexity. The first dimensions were drafted by means of a parametric study that combined a cost model and a stability analysis with the dimensions of the platform. The design space of the platform was characterized and the main dimensions were defined considering the cost of the platform and the resulting natural periods to avoid the interaction with the wave spectrum.

Once the platform concept was dimensioned, the mooring system was designed for the specific location. Semi taut mooring lines combining steel chain and polyester were designed to obtain a cost efficient system. Again, low complexity tools, based on static calculations were used for the conceptual design of the mooring system. Afterwards, more complex integrated simulations of the complete system including the wind turbine, the platform and the mooring system were performed based on a selected set of critical loadcases taken from the guidelines. The analysis showed that semi-taut mooring system was successfully designed for seakeeping the 10MW turbine on the TripleSpar floating platform: the maximum tensions were always below the MBL of the materials, the motions of the platform were moderate, the line did not hit the heave plates, the polyester did not contact the seabed and the anchors did not present vertical loads.

A specific control strategy was designed to ensure the stability of the TripleSpar platform supporting the INNWIND 10MW wind turbine. The control also aimed to maximize the power production and reduce the loads at the different mechanical components of the floating wind turbine.

The next step was to perform a detailed analysis to verify the mechanical integrity of the system. The most critical components of the platform were checked: the steel tripod, its connection with the concrete cylinders, the concrete reinforcement and the heave plates. This analysis was based on the ultimate loads obtained from the coupled simulation of a selected set of design load cases defined in the guidelines. The structural verification of the components under these loads was based on Finite Element. The elements were reinforced when needed, based on the results.

The proposed TripleSpar floater presents a good dynamic behavior and great potential to reduce the cost of the energy thanks to the use of concrete as construction material. The computations for the floater design included integrated simulations, hydrodynamic analysis, mooring line dynamics, control design and structural analysis. Based on these computations, the integrity of the system has been successfully verified. Nevertheless there are still aspects to be defined, mainly related to the manufacturing, transport or installation of the platform. In addition, some of the analysis performed would require an expansion, for instance, a more detailed computation of the design load cases is required for the concept certification, including fatigue analysis.

For the design of the VAWTs, a 10MW vertical rotor was defined as an upscale of the DeepWind 5MW design. This procedure faced certain difficulties as regards the controller which did not allow to go through a proper design verification of the 10MW version. By assuming that simple upscaling provides a valid result and taking into account that the 5MW version was verified, the dimensioning of the various components was made and then used to produce power production

and cost estimations. This gives 27€/MWh based on material costs exclusively. This cost level is promising and indicates the need for further investigation.

The development of these designs was based on simulation tools with different complexity levels for each stage of the design and with diverse capabilities. The design tools and methods have been developed during the INNWIND project, showing how the project has contributed to the development of the partner's design capabilities and numerical models. In addition, the design required a joint effort of all the participants on the task that promoted a fruitful exchange of knowledge.

## 11 REFERENCES

- EN 1992-1-1 *Design of concrete structures. General rules for buildings*. (2004).
- EN 1993-1-1: *Design of Steel Structures: Genral rules and rules for buildings* . (2004).
- Allen, C. K., Goupee, A. J., Dagher, H. J., & Viselli, A. M. (2015). Validation Of Global Performance Numerical Design Tools Used For Design Of Floating Offshore Wind Turbines. *Proceedings of the ASME 2015 34th International Conference on Ocean, Offshore and Arctic Engineering*. Saint John's/Canada.
- Allen, C., Goupee, A., Viselli, A., & Dagher, H. (2017). Experimental Validation of a Spectral-Based Structural Analysis Model Implemented in the Design of the VoltturnUS 6MW Floating Offshore Wind Turbine. San Francisco, California, USA: International Society of Offshore and Polar Engineers.
- Ansys. (2009). *Aqwa™-line manual*. Tech. rep.
- Bak, C. Z. (2013). *Description of the DTU 10 MW Reference Wind Turbine*. Report-I-0092.
- Bak, C., Zahle, F., Bitsche, R., Kim, T., Yde, A., Henriksen, L. C., et al. (2013). Reference Wind Turbine Report. *Deliverable 1.21*. INNWIND.EU.
- Bak, C., Zahle, F., Bitsche, R., Kim, T., Yde, A., Henriksen, L., et al. (n.d.). *Description of the DTU 10 MW Reference Wind Turbine*. Tech. rep., DTU.
- Barbit, A., & Delhommeau, G. (2015). Theoretical and numerical aspects of the open source BEM solver NEMOH. Nantes,France: Proc. of 11th European Wave and Tidal Energy Conference.
- Bard Offshore. (2009). Retrieved 06 2015, from [http://www.bard-offshore.de/uploads/tx\\_barddocuments/FactSheetBARD5.pdf](http://www.bard-offshore.de/uploads/tx_barddocuments/FactSheetBARD5.pdf)
- Bartrop, N. (1998). *Floating Structures: A Guide for Design and Analysis*. Oilfield Publications.
- (n.d.). *Berthelsen, Fylling,Vita, Paulsen:Conceptual design of a floating support structure and mooring System for a vertical axis wind turbine OMAE2012-83335*.
- Borg, M., Hansen, A., & Bredmose, H. (2016). Floating substructure flexibility of large-volume 10MW offshore wind turbine platforms in dynamic calculations. *Vol. 753, No. 8, 082024*.
- Chakrabarti, S. K. (2005). *Handbook of Offshore Engineering* (Vol. I). Elsevier.
- Chaviaropoulos, P. K., Karga, I., Harkness, C., & Hendriks, B. (2014, April). PI-based assessment of innovative concepts (methodology). *Deliverable 1.2.3*. INNWIND.EU.
- (n.d.). *Christos Galinos (1): Study of Design Load Cases for Multi-Megawatt Onshore Vertical Axis Wind Turbines*.
- (n.d.). *Christos Galinos (2): Vertical axis wind turbine design load cases investigation and comparison with horizontal axis wind turbine Paper presented at 13th Deepwind conference in Trondheim Norway, 2016*.
- (n.d.). *Christos Galinos (3): Variable speed control for Vertical Axis Wind Turbine. DTU Wind Energy Report I 0627(EN) 2017*.
- CSI. (2016). *Analysis Reference Manual*. Berkeley, California, USA .
- Cummins, W. (1962, October). The Impulse Response Function and Ship Motions. *Schiffstechnik*, pp. pp.101-109.
- (n.d.). *David Verelst et al: Detailed Load Analysis of the baseline 5MW DeepWind Concept , DTU Wind Energy E-0057, 2014*.

- Delhommeau, G. (1987). Les Problemes de diffraction-radiation et de resistance de vagues: etude theorique et resolution numerique par la methode des singularites. Thesis. Nantes: Ecole Nationale Superieure de Mecanique.
- DNV-GL. (2015, July). Position mooring DNVGL-OS-E301. *Offshore Standard* . DNV GL AS.
- DNV-OS-C101 *Design of Offshore Steel Structures, General (LRFD Method)*. (2011). (n.d.).
- DNV-RP-C203 *Fatigue Design Of Offshore Steel Structures*. (2011) . (n.d.).
- Dwyer, M. G., Viselli, A., Dagher, H., & Goupee, A. (2017). Experimental Verification Of Abs Concrete Design Methodology Applied To The Design Of The First Commercial Scale Floating Offshore Wind Turbine In The United States. *Proceedings of the ASME 2017 36th International Conference on Ocean, Offshore and Arctic Engineering*. Trondheim.
- Engels, W., Kanev, S., Savenije, F., & Wouters, D. (2013). ACT: Advanced Control Tool by ECN. In *proceedings of the EWEC*. Vienna: ECN-L--13-051.
- Faltinsen, O. M. (1990). *Sea Loads on Ship and Offshore Structures*. Cambridge: Cambridge University Press.
- Fischer, B. (2012). Reducing rotor speed variations of floating wind turbines by compensation of non-minimum phase zeros. EWEA 2012.
- Florian Amann, Frank Lemmer. (n.d.). *Deliverable D4.37-Design Solutions for 10MW Floating Offshore Wind Turbines*.
- Gómez, P., Sánchez, G., Llana, A., & Gonzalez, G. (2015). D1.1 Oceanographic and meteorological conditions for the design. *LIFES50+ Qualification of innovative floating substructures for 10MW wind turbines and water depths greater than 50m*.
- (n.d.). *Harald Svendsen: Description of simplified numerical model relevant for development of control concepts*. TR A7179 2012.
- I.E.C. (2005). *Wind Turbines-Part 1: Design Requirements, IEC 61400-1 Ed. 3*.
- I.E.C. (2008). *Wind Turbines-Part 3: Design Requirements for Offshore Wind Turbines, IEC 61400-3*.
- International-Electrotechnical-Commission. (2009). *IEC TS 61400-3 Wind Turbines – Part 3: Design requirements for offshore wind turbines, First Edition 2009-02*. ISBN 978-2-88910-514-4.
- Jonkman, J. (2007, nov). *Dynamics Modeling and Loads Analysis of an Offshore Floating Wind Turbine*. National Renewable Energy Laboratory. National Renewable Energy laboratory.
- Jonkman, J. (2008). Influence of control on the pitch damping of a floating wind turbine. In *Proceedings of the ASME Wind Energy Symposium*. Reno.
- Jonkman, J., Butterfield, S., Musial, W., & Scott, G. (2009). *Definition of a 5-MW Reference Wind Turbine for Offshore System Development*. NREL, Boulder/USA.
- Journée, J., & Massie, W. (2001). *OFFSHORE HYDROMECHANICS*. Delft: Delft University of Technology.
- Kaufer, D., Cosack, N., Böker, C., Seidel, M., & Kühn, M. (2009). Integrated analysis of the dynamics of offshore wind turbines with arbitrary support structures. *European Wind Energy Conference*. Marseille.
- Krisztina Leban: Design Sheet Nessie Design WP3 Deep Wind FIXED, extract from PhD thesis , 2014. (n.d.).
- Kvittem, M., & Moan, T. (2015). *Time domain analysis procedures for fatigue assessment of a semi-submersible wind turbine*. Marine Structures.

- Larsen, T. J., & Hanson, T. D. (n.d.). *A method to avoid negative damped low frequent tower vibrations for a floating, pitch controlled wind turbine*. Journal of Physics: Conference Series, 75, 012073. doi:10.1088/1742-6596/75/1/012073.
- Laugesen, R., & Hansen, A. M. (2015). *Experimental Study of the Dynamic Response of the DTU 10 MW Wind turbine on a Tension Leg Platform*. Ph.D. dissertation, DTU.
- Lee, C. (1998). *WAMIT—a radiation–diffraction panel program for wave-body interactions, user manual*. Dept. of Ocean Engineering, Massachusetts Institute of Technology, USA.
- Lemmer, F., Amann, F., Raach, S., & Schlipf, D. (2016). *Definition of the SWE-TripleSpar platform for the DTU10MW reference turbine*. Retrieved August 08, 2017, from Website of University of Stuttgart/SWE: <http://www.ifb.uni-stuttgart.de/windenergie/downloads>
- Lemmer, F., Müller, K., Pegalajar-Jurado, A., Borg, M., & Bredmose, H. (2016). *LIFES50+ D4.1: Simple Numerical Models for Upscaled Design*. Tech. rep., University of Stuttgart.
- Lemmer, F., Raach, S., Schlipf, D., & Cheng, P. W. (2015). Prospects of Linear Model Predictive Control on a 10MW Floating Wind Turbine. *Proceedings of the ASME 34th International Conference on Ocean, Offshore and Arctic Engineering*. St. John's/Canada.
- Lemmer, F., Schlipf, D., & Cheng, P. W. (2016). Control design methods for floating wind turbines for optimal disturbance rejection. *Journal of Physics: Conference Series*, 753.
- (n.d.). *Life50+: Qualification of innovative floating substructures for 10MW wind turbines and water depths greater than 50m*.
- Lopez, J. M. (n.d.). D1.1 - Oceanographic and meteorological conditions for the design. *Lifes50+*.
- Luan, C., Gao, Z., & Moan, T. (2017). Development and verification of a time-domain approach for determining forces and moments in structural components of floaters with an application to floating wind turbines. pp. 87-109.
- Manjock, A., D. Manolas, F. Sandner and S. Voutsinas. (2014). *INNWIND.EU D4.2.3: Integrated Design Methods and Controls for Floating Wind Turbines*. Tech rep. (n.d.).
- Manolas D.I., R. V. (2014). Assessing the importance of geometric non-linear effects in the prediction of wind turbine blade loads. *Computational and Nonlinear Dynamics Journal*, Vol. 10, 041008.
- Manolas, D. (2015). *Hydro-aero-elastic analysis of offshore wind turbines, PhD Thesis*. Athens: NTUA.
- Massel, S. (1996). *Ocean Surface Waves: Their Physics and Prediction* (Advanced Series on Ocean Engineering, Vol. 11 ed.). Singapore – New Jersey – London – Hong Kong: World Scientific Publishing Co. Pte. Ltd.
- Molins, C., Campos, A., Sandner, F., & Matha, D. (2014). Monolithic Concrete Off-Shore Floating Structure For Wind Turbines. *Proceedings of the EWEA*.
- Namik, H., & Stol, K. (2010). Individual blade pitch control of floating offshore wind turbines. *Wind energy*, 13, 74-85.
- National Renewable Energy Laboratory. (2016, July 27). *NWTC Information Portal (FAST v8)*. Retrieved from <https://nwtc.nrel.gov/FAST8>
- NWTC. (2016). *NWTC Information Portal (FAST v8)*.
- NWTC. (2016). *NWTC Information Portal (FAST v8)*. Retrieved from <https://nwtc.nrel.gov/FAST8>
- (n.d.). *Rachel Meyer: Stability Analysis of Multi-Megawatt Darrieus- Type Floating Vertical Axis Wind Turbines DTU Wind Energy-M-0099 2016*.

- Riziotis, V., & Voustinas, S. (1997). Gast: A General Aerodynamic and Structural Prediction Tool for Wind Turbines. *Proceedings of the EWEC`97*. Dublin, Ireland.
- Sandner, F., Yu, W., Matha, D., Azcona, J., Munduate, X., Grela, E., et al. (2014). *INNWIND.EU D4.33: Innovative Concepts for Floating Structures*. Tech. rep.
- Savenije, F., & Peeringa, J. (2014). Control development for floating wind. *Journal of Physics: Conference Series*, 524.
- Schlipf, D., Simley, E., Lemmer, F., Pao, L., & Cheng, P. W. (2015). Collective Pitch Feedforward Control of Floating Wind Turbines Using Lidar. *Journal of Ocean and Wind Energy*, 2(4), 223-230.
- Skaare, B. (2017). Development of the Hywind Concept. *Proceedings of the ASME 2017 36th International Conference on Ocean, Offshore and Arctic Engineering*. Trondheim.
- Stache, F., & Ehlers, B. (2009). Wind turbine aeroelastic simulation by embedding Flex5 into SIMPACK. *SIMPACK Newsletter*, 6-7.
- (n.d.). *Torben Larsen: Slip generator model implemented in HAWC2 as an external DLL Wind Energy Department 2005-12-05 J.nr. 200500523*.
- Van der Hooft, E., & Van Engelen, T. (2004). Estimated wind speed feed forward control for wind turbine operation optimisation. *Presented at the EWEC*. London: ECN-RX-04-126.
- Veen, G. V., Couchman, Y., & Bowyer, R. (2012). Control of floating wind turbines. *Proceedings of the American Control Conference ACC*, (pp. 3148-3153).
- Walia , D. (2015). *Coupled simulation of structural loads of floating wind energy converters*. Master Thesis.